

Are Learned Molecular Representations Ready For Prime Time?

Kevin Yang,^{*,†} Kyle Swanson,^{*,†} Wengong Jin,[†] Connor Coley,[‡] Philipp Eiden,[¶]
Hua Gao,[§] Angel Guzman-Perez,[§] Timothy Hopper,[§] Brian Kelley,^{||} Miriam
Mathea,[¶] Andrew Palmer,[¶] Volker Settels,[¶] Tommi Jaakkola,[†] Klavs Jensen,[‡]
and Regina Barzilay[†]

[†]*Computer Science and Artificial Intelligence Laboratory, MIT, Cambridge, MA*

[‡]*Department of Chemical Engineering, MIT, Cambridge, MA*

[¶]*BASF SE, Ludwigshafen, Germany*

[§]*Amgen Inc., Cambridge, MA*

^{||}*Novartis Institutes for BioMedical Research, Cambridge, MA*

E-mail: yangk@mit.edu; swansonk@mit.edu

Advancements in neural machinery have led to a wide range of algorithmic solutions for molecular property prediction. Two classes of models in particular have yielded promising results: neural networks applied to computed molecular fingerprints or expert-crafted descriptors, and graph convolutional neural networks that construct a learned molecular representation by operating on the graph structure of the molecule. However, recent literature has yet to clearly determine which of these two methods is superior when generalizing to new chemical space. Furthermore, prior research has rarely examined these new models in industry research settings in comparison to existing employed models. In this paper, we benchmark models extensively on 19 public and 15 proprietary industrial datasets spanning

a wide variety of chemical endpoints. In addition, we introduce a graph convolutional model that consistently outperforms models using fixed molecular descriptors as well as previous graph neural architectures on both public and proprietary datasets. Our empirical findings indicate that while approaches based on these representations have yet to reach the level of experimental reproducibility, our proposed model nevertheless offers significant improvements over models currently used in industrial workflows.

Introduction

Molecular property prediction, one of the oldest cheminformatics tasks, has received new attention in light of recent advancements in deep neural networks. These architectures either operate over fixed molecular fingerprints common in traditional QSAR models, or they learn their own task-specific representations using graph convolutions.¹⁻¹¹ Both approaches are reported to yield substantial performance gains, raising state-of-the-art accuracy in property prediction.

Despite these successes, many questions remain unanswered. The first question concerns the comparison between learned molecular representations and fingerprints or descriptors. Unfortunately, current published results on this topic do not provide a clear answer. Wu et al.² demonstrate that convolution-based models typically outperform fingerprint-based models, while experiments reported in Mayr et al.¹² report the opposite. Part of these discrepancies can be attributed to differences in evaluation setup, including the way datasets are constructed. This leads us to a broader question concerning current evaluation protocols and their capacity to measure the generalization power of a method when applied to a new chemical space, as is common in drug discovery. Unless special care is taken to replicate this distributional shift in evaluation, neural models may overfit the training data but still score highly on the test data. This is particularly true for convolutional models that can learn a poor molecular representation by memorizing the molecular scaffolds in the training data

and thereby fail to generalize to new ones. Therefore, a meaningful evaluation of property prediction models needs to account explicitly for scaffold overlap between train and test data in light of generalization requirements.

In this paper, we aim to answer both of these questions by designing a comprehensive evaluation setup for assessing neural architectures. We also introduce an algorithm for property prediction that outperforms existing strong baselines across a range of datasets. The model has two distinctive features: (1) It operates over a hybrid representation that combines convolutions and descriptors. This design gives it flexibility in learning a task specific encoding, while providing a strong prior with fixed descriptors. (2) It learns to construct molecular encodings by using convolutions centered on bonds instead of atoms, thereby avoiding unnecessary loops during the message passing phase of the algorithm.

We evaluate our model and other recently published neural architectures on both publicly available benchmarks, such as those from Wu et al.² and Mayr et al.,¹² as well as proprietary datasets from Amgen, Novartis, and BASF (Badische Anilin und Soda Fabrik). Our goal is to assess whether the models' performance on the public datasets and their relative ranking are representative of their ranking on the proprietary datasets. We demonstrate that under a scaffold split of training and testing data, the relative ranking of the models is consistent across the two classes of datasets. We also show that a scaffold-based split of the training and testing data is a good approximation of the temporal split commonly used in industry in terms of the relevant metrics. By contrast, a purely random split is a poor approximation to a temporal split, confirming the findings of Sheridan.¹³ To put the performance of current models in perspective, we report bounds on experimental error and show that there is still room for improving deep learning models to match the accuracy and reproducibility of screening results.

Building on the diversity of our benchmark datasets, we explore the impact of molecular representation with respect to the dataset characteristics. We find that a hybrid representation yields higher performance and generalizes better than either convolution-based or

fingerprint-based models. We also note that on small datasets (up to 1000 training molecules) fingerprint models can outperform learned representations, which are negatively impacted by data sparsity. Beyond molecular representation issues, we observe that hyperparameter selection plays a crucial role in model performance, consistent with prior work.¹⁴ We show that Bayesian optimization yields a robust, automatic solution to this issue. The addition of ensembling further improves accuracy, again consistent with the literature.¹⁵

In aggregate, we conclude that our model achieves consistently strong out-of-the-box performance and even stronger optimized performance across a wide range of public and proprietary datasets, indicating its applicability as a useful tool for chemists actively working on drug discovery.

Background

Since the core element of our model is a graph encoder architecture, our work is closely related to previous work on graph encoders, such as those for social networks^{6,16} or for chemistry applications.^{1,7–9,17–24}

Common approaches to molecular property prediction today involve the application of well-known models like support vector machines²⁵ or random forests²⁶ to expert-engineered descriptors or molecular fingerprints, such as the Dragon descriptors²⁷ or Morgan (ECFP) fingerprints.²⁸ One direction of advancement is the use of domain expertise to improve the base feature representation of molecular descriptors^{27,29–32} to drive better performance.¹² Additionally, many studies have leveraged explicit 3D atomic coordinates to improve performance further.^{2,33–36}

The other main line of research is the optimization of the model architecture, whether the model is applied to descriptors or fingerprints^{12,37} or is directly applied to SMILES³⁸ strings¹² or the underlying graph of the molecule.^{1–11} Our model belongs to the last category of models, known as graph convolutional neural networks. In essence, such models learn their

own expert feature representations directly from the data, and they have been shown to be very flexible and capable of capturing complex relationships given sufficient data.^{2,4}

In a direction orthogonal to our own improvements, Ishiguro et al.³⁹ also make a strong improvement to graph neural networks. Liu et al.⁴⁰ also evaluate their model against private industry datasets, but we cannot compare against their method directly owing to dataset differences.⁴⁰

The property prediction models most similar to our own are encapsulated in the Message Passing Neural Network (MPNN) framework presented in Gilmer et al.⁴ We build upon this basic framework by adopting a message-passing paradigm based on updating representations of directed bonds rather than atoms. Additionally, we further improve the model by combining computed molecule-level features with the molecular representation learned by the MPNN.

Methods

We first summarize MPNNs in general using the terminology of Gilmer et al.,⁴ and then we expand on the characteristics of Directed MPNN (D-MPNN)¹⁹ used in this paper.¹

Message Passing Neural Networks

An MPNN is a model which operates on an undirected graph G with node (atom) features x_v and edge (bond) features e_{vw} . MPNNs operate in two phases: a *message passing phase*, which transmits information across the molecule to build a neural representation of the molecule, and a *readout phase*, which uses the final representation of the molecule to make predictions about the properties of interest.

More specifically, the message passing phase consists of T steps. On each step t , hidden states h_v^t and messages m_v^t associated with each vertex v are updated using message function

¹D-MPNN is originally called *structure2vec* in Dai et al.¹⁹ In this paper, we refer to it as Directed MPNN to show it is a variant of the generic MPNN architecture.

M_t and vertex update function U_t according to:

$$m_v^{t+1} = \sum_{w \in N(v)} M_t(h_v^t, h_w^t, e_{vw})$$

$$h_v^{t+1} = U_t(h_v^t, m_v^{t+1})$$

where $N(v)$ is the set of neighbors of v in graph G , and h_v^0 is some function of the initial atom features x_v . The readout phase then uses a readout function R to make a property prediction based on the final hidden states according to

$$\hat{y} = R(\{h_v^T | v \in G\}).$$

The output \hat{y} may be either a scalar or a vector, depending on whether the MPNN is designed to predict a single property or multiple properties (in a multitask setting).

During training, the network takes molecular graphs as input and makes an output prediction for each molecule. A loss function is computed based on the predicted outputs and the ground truth values, and the gradient of the loss is backpropagated through the readout phase and the message passing phase. The entire model is trained end-to-end.

Directed MPNN

The main difference between the Directed MPNN (D-MPNN)¹⁹ and the generic MPNN described above is the nature of the messages sent during the message passing phase. Rather than using messages associated with vertices (atoms), D-MPNN uses messages associated with directed edges (bonds). The motivation of this design is to prevent totters⁴¹, that is, to avoid messages being passed along any path of the form $v_1 v_2 \cdots v_n$ where $v_i = v_{i+2}$ for some i . Such excursions are likely to introduce noise into the graph representation. Using Figure 1 as an illustration, in D-MPNN, the message $1 \rightarrow 2$ will only be propagated to nodes 3 and 4 in the next iteration, whereas in the original MPNN it will be sent to node 1 as

well, creating an unnecessary loop in the message passing trajectory. Compared to the atom based message passing approach, this message passing procedure is more similar to belief propagation in probabilistic graphical models.⁴² We refer to Dai et al.¹⁹ for futher discussion about the connection between D-MPNN and belief propagation.

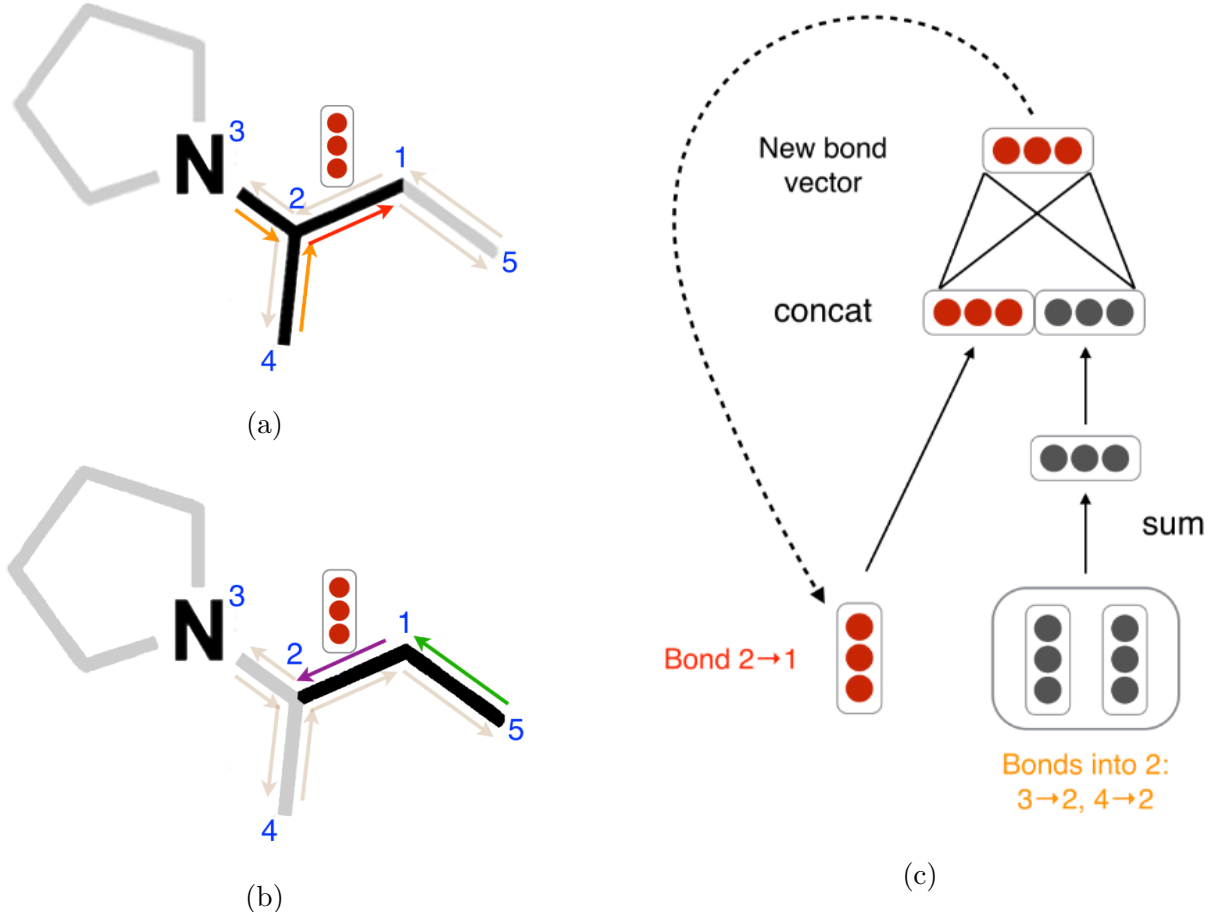


Figure 1: Illustration of bond-level message passing in our proposed D-MPNN. (a): Messages from the orange directed bonds are used to inform the update to the hidden state of the red directed bond. By contrast, in a traditional MPNN, messages are passed from atoms to atoms (for example atoms 1, 3, and 4 to atom 2) rather than from bonds to bonds. (b): Similarly, a message from the green bond informs the update to the hidden state of the purple directed bond. (c): Illustration of the update function to the hidden representation of the red directed bond from diagram (a).

The D-MPNN works as follows. The D-MPNN operates on hidden states h_{vw}^t and messages m_{vw}^t instead of on node based hidden states h_v^t and messages m_v^t . Note that the direction of messages matters (i.e., h_{vw}^t and m_{vw}^t are distinct from h_{wv}^t and m_{wv}^t). The

corresponding message passing update equations are thus

$$m_{vw}^{t+1} = \sum_{k \in \{N(v) \setminus w\}} M_t(x_v, x_k, h_{kv}^t)$$

$$h_{vw}^{t+1} = U_t(h_{vw}^t, m_{vw}^{t+1}).$$

Observe that message m_{vw}^{t+1} does not depend on its reverse message m_{wv}^t from the previous iteration. Prior to the first step of message passing, we initialize edge hidden states with

$$h_{vw}^0 = \tau(W_i \text{ cat}(x_v, e_{vw}))$$

where $W_i \in \mathbb{R}^{h \times h_i}$ is a learned matrix, $\text{cat}(x_v, e_{vw}) \in \mathbb{R}^{h_i}$ is the concatenation of the atom features x_v for atom v and the bond features e_{vw} for bond vw , and τ is the ReLU activation function.⁴³

We choose to use relatively simple message passing functions M_t and edge update functions U_t . Specifically, we define $M_t(x_v, x_w, h_{vw}^t) = h_{vw}^t$ and we implement U_t with the same neural network on every step,

$$U_t(h_{vw}^t, m_{vw}^{t+1}) = U(h_{vw}^t, m_{vw}^{t+1}) = \tau(h_{vw}^0 + W_m m_{vw}^{t+1})$$

where $W_m \in \mathbb{R}^{h \times h}$ is a learned matrix with hidden size h . Note that the addition of h_{vw}^0 on every step provides a skip connection to the original feature vector for that edge.

Finally, we return to an atom representation of the molecule by summing the incoming bond features according to

$$m_v = \sum_{k \in N(v)} h_{kv}^T$$

$$h_v = \tau(W_a \text{cat}(x_v, m_v))$$

where $W_a \in \mathbb{R}^{h \times h}$ is a learned matrix.

Altogether, the D-MPNN message passing phase operates according to

$$h_{vw}^0 = \tau(W_i \text{ cat}(x_v, e_{vw}))$$

followed by

$$\begin{aligned} m_{vw}^{t+1} &= \sum_{k \in \{N(v) \setminus w\}} h_{kv}^t \\ h_{vw}^{t+1} &= \tau(h_{vw}^0 + W_m m_{vw}^{t+1}) \end{aligned}$$

for $t \in \{1, \dots, T\}$, followed by

$$\begin{aligned} m_v &= \sum_{w \in N(v)} h_{vw}^T \\ h_v &= \tau(W_a \text{cat}(x_v, m_v)). \end{aligned}$$

The readout phase of the D-MPNN is the same as the readout phase of a generic MPNN.

In our implementation of the readout function R , we first sum the atom hidden states to obtain a feature vector for the molecule

$$h = \sum_{v \in G} h_v.$$

Finally, we generate property predictions $\hat{y} = f(h)$ where $f(\cdot)$ is a feed-forward neural network.

Initial Featurization

Our model's initial atom and bond features are listed in Tables 1 and 2, respectively. The D-MPNN's initial node features x_v are simply the atom features for that node, while the

D-MPNN’s initial edge features e_{vw} are the bond features for bond vw . All features are computed using the open-source package RDKit.⁴⁴

Table 1: Atom Features. All features are one-hot encodings except for atomic mass, which is a real number scaled to be on the same order of magnitude.

Feature	Description	Size
Atom type	Type of atom (ex. C, N, O), by atomic number.	100
# Bonds	Number of bonds the atom is involved in.	6
Formal charge	Integer electronic charge assigned to atom.	5
Chirality	Unspecified, tetrahedral CW/CCW, or other.	4
# Hs	Number of bonded Hydrogen atom.	5
Hybridization	sp, sp ² , sp ³ , sp ³ d, or sp ³ d ² .	5
Aromaticity	Whether this atom is part of an aromatic system.	1
Atomic mass	Mass of the atom, divided by 100.	1

Table 2: Bond Features. All features are one-hot encodings.

Feature	Description	Size
Bond type	Single, double, triple, or aromatic.	4
Conjugated	Whether the bond is conjugated.	1
In ring	Whether the bond is part of a ring.	1
Stereo	None, any, E/Z or cis/trans.	6

D-MPNN with Features

Next, we discuss further extensions and optimizations to improve performance. Although an MPNN should ideally be able to extract *any* information about a molecule that might be relevant to predicting a given property, two limitations may prevent this in practice. First, many property prediction datasets are very small, i.e., on the order of only hundreds or thousands of molecules. With so little data, MPNNs are unable to learn to identify and extract all features of a molecule that might be relevant to property prediction, and they are susceptible to overfitting to artifacts in the data. Second, most MPNNs use fewer message passing steps than the diameter of the molecular graph, i.e. $T < \text{diam}(G)$, meaning atoms that are a distance of greater than T bonds apart will never receive messages about each other. This results in a molecular representation that is fundamentally local rather than

global in nature, meaning the MPNN may struggle to predict properties that depend heavily on global features.

In order to counter these limitations, we introduce a variant of the D-MPNN that incorporates 200 global molecular features that can be computed rapidly *in silico* using RDKit. The neural network architecture requires that the features are appropriately scaled to prevent features with large ranges dominating smaller ranged features, as well as preventing issues where features in the training set are not drawn from the same sample distribution as features in the testing set. To prevent these issues, a large sample of molecules was used to fit cumulative density functions (CDFs) to all features. CDFs were used as opposed to simpler scaling algorithms mainly because CDFs have the useful property that each value has the same meaning: the percentage of the population observed below the raw feature value. Min-max scaling can be easily biased with outliers and Z-score scaling assumes a normal distribution which is most often not the case for chemical features, especially if they are based on counts.

The CDFs were fit to a sample of 100k compounds from the Novartis internal catalog using the distributions available in the scikit-learn package,⁴⁵ a sample of which can be seen in Figure 2. One could do a similar normalization using publicly available databases such as ZINC⁴⁶ and PubChem.⁴⁷ scikit-learn was used primarily due to the simplicity of fitting and the final application. However, more complicated techniques could be used in the future to fit to empirical CDFs, such as finding the best fit general logistic function, which has been shown to be successful for other biological datasets.⁴⁸ No review was taken to remove odd distributions. For example, azides are hazardous and rarely used outside of a few specific reactions, as reflected in the fr_azide distribution in Figure 2. As such, since the sample data was primarily used for chemical screening against biological targets, the distribution used here may not accurately reflect the distribution of reagents used for chemical synthesis. For the full list of calculated features, please refer to the Supporting Information.

To incorporate these features, we modify the readout phase of the D-MPNN to apply the

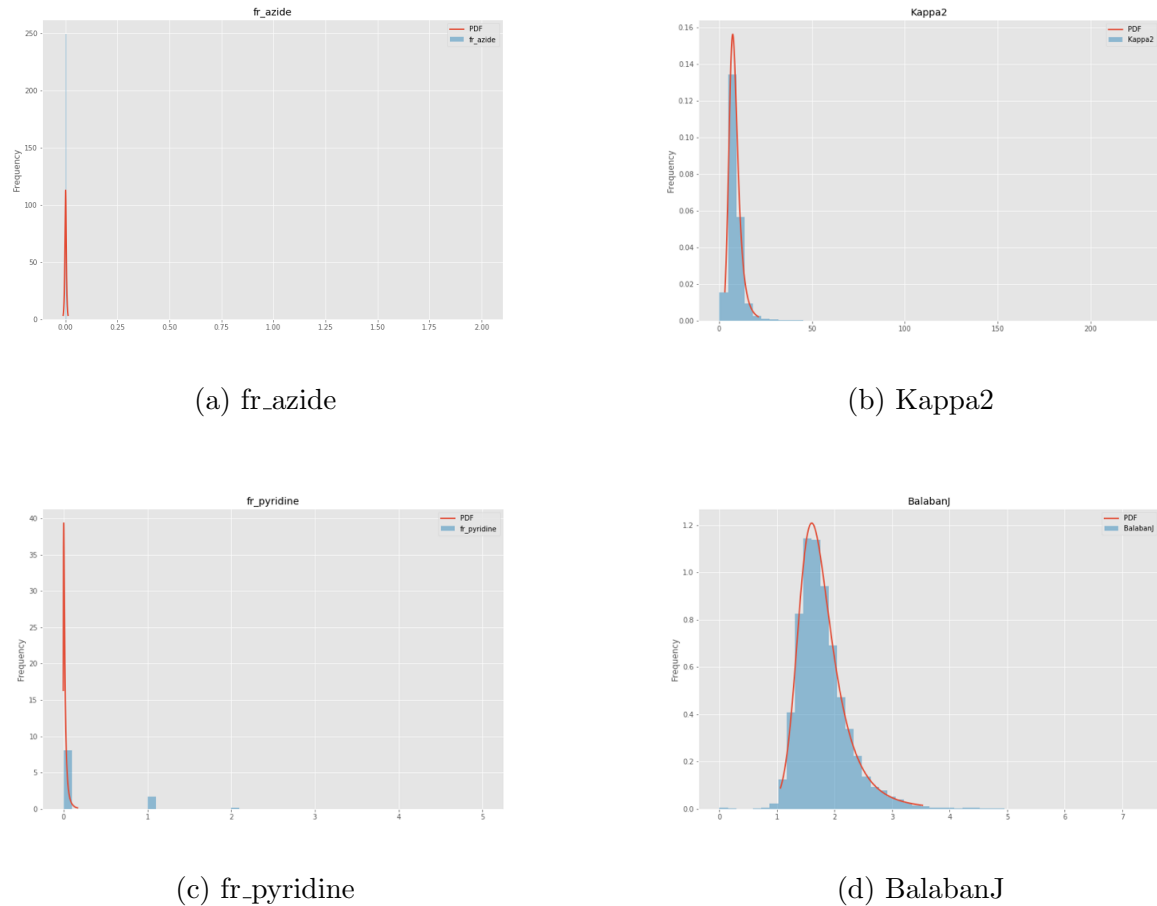


Figure 2: Four example distributions fit to a random sample of 100,000 compounds used for biological screening in Novartis. Note that some distributions for discrete calculations, such as fr_pyridine, are not fit especially well. This is an active area for improvement.

feed-forward neural network f to the concatenation of the learned molecule feature vector h and the computed global features h_f ,

$$\hat{y} = f(\text{cat}(h, h_f)).$$

This is a very general method of incorporating external information and can be used with any MPNN and any computed features or descriptors.

Hyperparameter Optimization

The performance of MPNNs, like most neural networks, can depend greatly on the settings of the various model hyperparameters, such as the hidden size of the neural network layers. Thus to maximize performance, we perform hyperparameter optimization via Bayesian Optimization¹⁴ using the `Hyperopt`⁴⁹ Python package. We specifically optimize our model's depth (number of message-passing steps), hidden size (size of bond message vectors), number of feed-forward network layers, and dropout probability.

Ensembling

A common technique in machine learning for improving model performance is ensembling, where the predictions of multiple independently trained models are combined to produce a more accurate prediction.¹⁵ We apply this technique by training several copies of our model, each initialized with different random weights, and then averaging the predictions of these models (each with equal weight) to generate an ensemble prediction.

Since prior work did not report performance using ensembling, all direct comparisons we make to prior work use a single D-MPNN model for a fair comparison. However, we also report results using an ensemble to illustrate the maximum possible performance of our model architecture.

Implementation

We implement our model using the PyTorch⁵⁰ deep learning framework. All code for the D-MPNN and its variants is available in our GitHub repository.⁵¹ Code for computing and using the RDKit feature CDFs is available in the `Descriptastorus` package.⁵² Additionally, a web demonstration of our model’s predictive capability on public datasets is available online.⁵³

Experiments

Data

We test our model on 19 publicly available datasets from Wu et al.² and Mayr et al..¹² These datasets range in size from less than 200 molecules to over 450,000 molecules. They include a wide range of regression and classification targets spanning quantum mechanics, physical chemistry, biophysics, and physiology. In particular, they measure the following properties:

- QM7, QM8, and QM9 consist of computer-generated quantum mechanical properties, such as atomization energy
- ESOL measures water solubility
- FreeSolv measures hydration free energy in water
- Lipophilicity measures octanol/water distribution coefficients
- The three PDBbind datasets measure protein binding affinity
- PCBA and MUV measure assorted biological assays
- HIV measures inhibition of HIV replication
- BACE measures inhibition of human β -secretase 1

- BBBP measures the ability to penetrate the blood-brain-barrier
- Tox21, ToxCast, and ClinTox measure toxicity
- SIDER labels drugs with side effects
- ChEMBL is a large collection of biological assays, such as binding affinities for different targets

Summary statistics for all the datasets are provided in Table 3², and further details on the datasets are available in Wu et al.,² with the exception of the ChEMBL dataset which is described in Mayr et al.¹² Additional information on the class balance of the classification datasets is provided in the Supporting Information³.

Experimental Procedure

Cross-Validation and Hyperparameter Optimization. Since many of the datasets are very small (two thousand molecules or fewer), we use a cross-validation approach to decrease noise in the results both while optimizing the hyperparameters and while determining final performance numbers. For consistency, we maintain the same approach for all of our datasets. Specifically, for each dataset, we use 20 iterations of Bayesian optimization on 10 randomly-seeded 80:10:10 data splits to determine the best hyperparameters, selecting hyperparameters based on validation set performance. We then evaluate the model by re-training using the optimal hyperparameters and checking performance on the test set. Due to computational cost, we only use 3 splits for HIV, QM9, MUV, PCBA, and ChEMBL. When we run the best model from Mayr et al.¹² for comparative purposes, we optimize

²For some datasets, the number of compounds in Table 3 does not precisely match the numbers from Wu et al.² because we removed a small number of molecules which could not be processed by RDKit.⁴⁴ Furthermore, we have fewer molecules in QM7 because we used SMILES strings generated by Wu et al.² from the original 3D coordinates in the dataset, but the SMILES conversion process failed for ~ 300 molecules. (Note that QM7 and some of the other MoleculeNet datasets are more commonly used for benchmarking models that leverage 3D information, rather than purely SMILES-based methods like our own.)

³The MUV dataset is particularly unbalanced, with only 0.2% of molecules classified as positive. This makes our model unstable, leading to the wide variation in performance in the subsequent sections.

Table 3: Summary statistics of the public datasets used in this paper. Note: PDBbind-F, PDBbind-C, and PDBbind-R refer to the full, core, and refined PDBbind datasets from Wu et al..²

Category	Dataset	# Tasks	Task Type	# Compounds	Metric
Quantum Mechanics	QM7	1	Regression	6,830	MAE
Quantum Mechanics	QM8	12	Regression	21,786	MAE
Quantum Mechanics	QM9	12	Regression	133,884	MAE
Physical Chemistry	ESOL	1	Regression	1,128	RMSE
Physical Chemistry	FreeSolv	1	Regression	642	RMSE
Physical Chemistry	Lipophilicity	1	Regression	4,200	RMSE
Biophysics	PDBbind-F	1	Regression	9,880	RMSE
Biophysics	PDBbind-C	1	Regression	168	RMSE
Biophysics	PDBbind-R	1	Regression	3,040	RMSE
Biophysics	PCBA	128	Classification	437,928	PRC-AUC
Biophysics	MUV	17	Classification	93,087	PRC-AUC
Biophysics	HIV	1	Classification	41,127	ROC-AUC
Biophysics	BACE	1	Classification	1,513	ROC-AUC
Physiology	BBBP	1	Classification	2,039	ROC-AUC
Physiology	Tox21	12	Classification	7,831	ROC-AUC
Physiology	ToxCast	617	Classification	8,576	ROC-AUC
Physiology	SIDER	27	Classification	1,427	ROC-AUC
Physiology	ClinTox	2	Classification	1,478	ROC-AUC
Physiology	ChEMBL	1,310	Classification	456,331	ROC-AUC

their model’s hyperparameters with the same splits, using their original hyperparameter optimization script.

Split Type. We evaluate all models on random and scaffold-based splits⁴, as well as on the original splits from Wu et al.² and Mayr et al..¹²

Our scaffold split is similar to that of Wu et al..² Molecules are partitioned into bins based on their Murcko scaffold calculated by RDKit.⁴⁴ Any bins larger than half of the desired test set size are placed into the training set, in order to guarantee the scaffold diversity of the validation and test sets. All remaining bins are placed randomly into the training, validation, and test sets until each set has reached its desired size. As this latter process involves randomly placing scaffolds into bins, we are able to generate several different scaffold

⁴With the exception of the model of Mayr et al.¹² which was only run on scaffold-based splits, due to the large computational cost of optimizing their model. Results on random splits are presented in the Supporting Information.

splits for evaluation.

None of our splits on classification datasets are stratified; we do not enforce class balance. Compared to random splits, the scaffold splits have more class imbalance on average, but are not excessively imbalanced; we analyze this class balance quantitatively in the Supporting Information.

Compared to a random split, a scaffold split is a more challenging and realistic evaluation setting as shown in Figures 11 and 13. This allows us to use a scaffold split as a proxy for the chronological split present in real-world property prediction data, where one trains a model on past data to make predictions on future data, although chronological splits are still preferred when available. However, as chronological information is not available for most public datasets, we use a scaffold-based split for all evaluations except for our direct comparison with the MoleculeNet models from Wu et al.,² for which we use their original data splits.

Baselines. We compare our model to the following baselines:

- The best model for each dataset from MoleculeNet by Wu et al.²
- The best model from Mayr et al.,¹² a feed-forward neural network on a concatenation of assorted expert-designed molecular fingerprints.
- Random forest on binary Morgan fingerprints.
- Feed-forward network (FFN) on binary Morgan fingerprints using the same FFN architecture that our D-MPNN uses during its readout phase.
- FFN on count-based Morgan fingerprints.
- FFN on RDKit-calculated descriptors.

The models in MoleculeNet by Wu et al.² include MPNN,⁴ Weave,³ GraphConv, kernel ridge regression, gradient boosting,⁵⁴ random forest,²⁶ logistic regression,⁵⁵ directed acyclic

graph models,⁵⁶ support vector machines,⁵⁷ Deep Tensor Neural Networks,¹⁰ multitask networks,⁵⁸ bypass networks,⁵⁹ influence relevance voting,⁶⁰ and/or ANI-1,⁶¹ depending on the dataset. Full details can be found in Wu et al..² For the feed-forward network model from Mayr et al.,¹² we modified the authors' original code with their guidance in order to run their code on all of the datasets, not just on the ChEMBL dataset they experimented with. We tuned learning rates and hidden dimensions in addition to the extensive hyperparameter search already present in their code.

Results and Discussion

In the following sections, we analyze the performance of our model on both public and proprietary datasets. Specifically, we aim to answer the following questions:

1. How does our model perform on both public and proprietary datasets compared to public benchmarks, and how close are we to the upper bound on performance represented by experimental reproducibility?
2. How should we be splitting our data, and how does the method of splitting affect our evaluation of the model's generalization performance?
3. What are the key elements of our model, and how can we maximize its performance?

In the following sections, all results using root-mean-square error (RMSE) or mean absolute error (MAE) are displayed as plots showing change relative to a baseline model rather than showing absolute performance numbers. This is because the scale of the errors can differ drastically between datasets. All results using R^2 , area under the receiver operating characteristic curve (ROC-AUC), or area under the precision recall curve (PRC-AUC) are displayed as plots showing the actual values. For RMSE and MAE, lower is better, while for R^2 , ROC-AUC, and PRC-AUC, higher is better. Table 3 indicates the metric used for each dataset. Tables showing the exact performance numbers for all experiments can be found in

the Supporting Information. Note that the error bars on all plots show the standard error of the mean across multiple runs, where standard error is defined as the standard deviation divided by the square root of the number of runs. We evaluate statistical significance in all experiments using an independent samples t-test and checking the p-value, comparing our best single (non-ensembled) model to the baselines. We define statistical significance as p-value less than 0.05.

Additionally, note that in all figures and tables, “D-MPNN” refers to the base D-MPNN model, “D-MPNN Features” refers to the D-MPNN with RDKit features, “D-MPNN Optimized” refers to the D-MPNN with RDKit features and optimized hyperparameters, and “D-MPNN Ensemble” refers to an ensemble of five D-MPNNs with RDKit features and optimized hyperparameters.

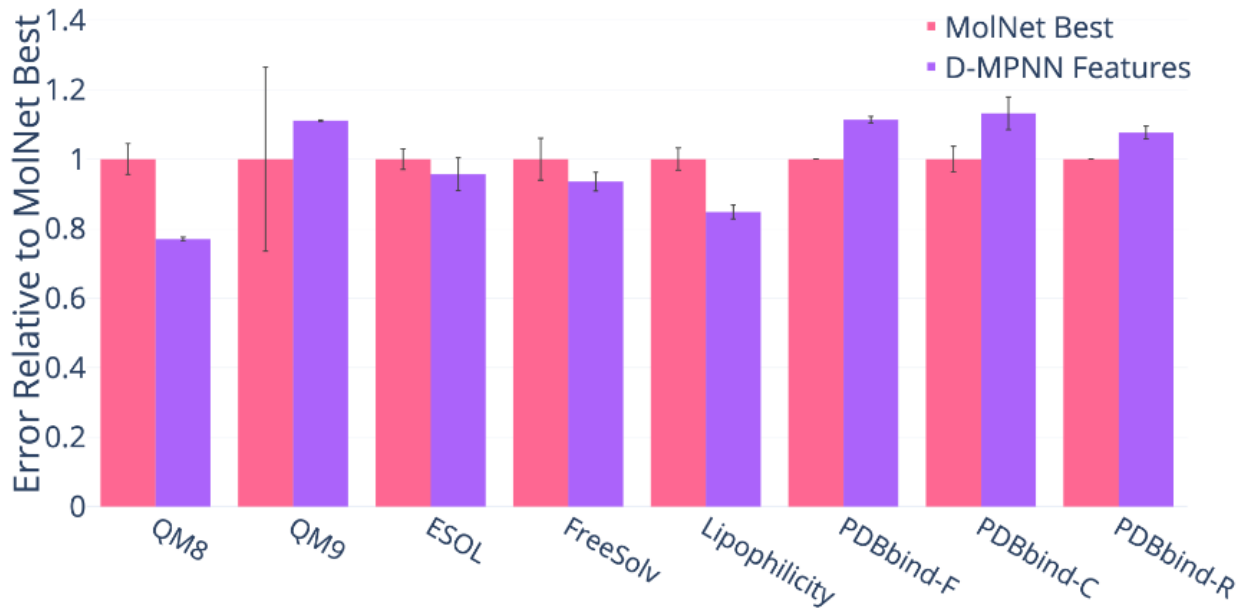
Comparison to Baselines

After optimizing our model, we compare our best single (non-ensembled) model on each dataset against models from prior work.

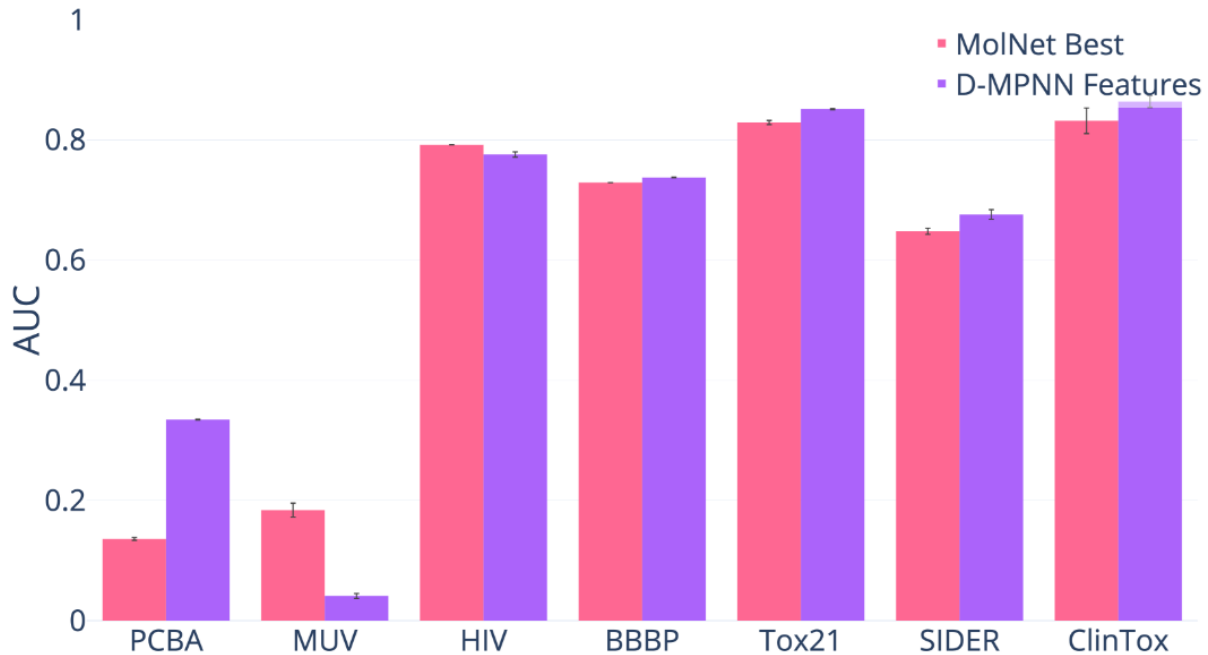
Comparison to MoleculeNet

We first compare our D-MPNN to the best model from MoleculeNet^{2,62} on the same datasets and splits on which Wu et al.² evaluate their models. We were unable to reproduce their original data splits on BACE, Toxcast, and QM7, but we have evaluated our model against their original splits on all of the other datasets. The splits are a mix of random, scaffold, and time splits, as indicated in Figure 3.

We note that there are two cases in which our D-MPNN may underperform. The first is the MUV dataset, which is large but extremely imbalanced; only 0.2% of samples are labeled as positives. Wu et al.² also encountered great difficulty with this extreme class imbalance when experimenting with the MUV dataset; all other datasets we experiment on contain at least 1% positives (see the Supporting Information for full class balance information). The



(a) Regression Datasets (lower = better).



(b) Classification Datasets (higher = better).

Figure 3: Comparison of our D-MPNN with features to the best models from Wu et al.² The differences on QM8, PCBA, MUV, BBBP, and Tox21 are statistically significant.

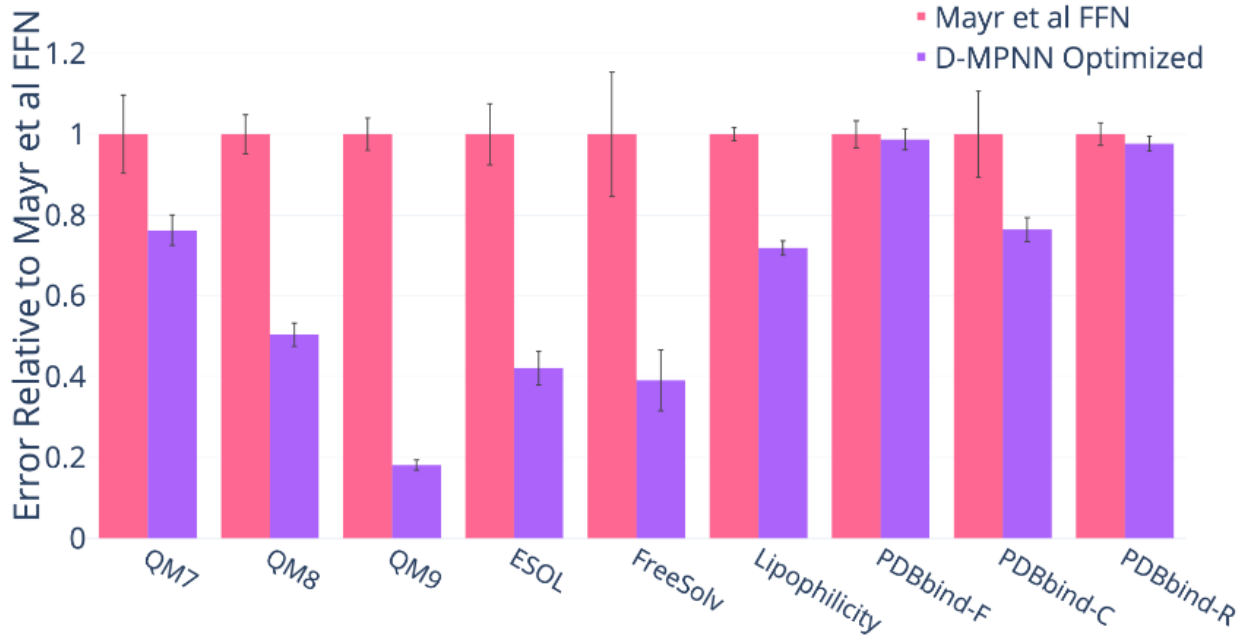
second exception is when there is auxiliary 3D information available, as in the three variants of the PDBbind dataset and in QM9. The current iteration of our D-MPNN does not use 3D coordinate information, and we leave this extension to future work. Thus it is unsurprising that our D-MPNN model underperforms models using 3D information on a protein binding affinity prediction task such as PDBbind, where 3D structure is key. Nevertheless, our D-MPNN model outperforms the best graph-based method in MoleculeNet on PDBbind and QM9. Moreover, we note that on another dataset that provides 3D coordinate information, QM8, our model outperforms the best model in MoleculeNet with or without 3D coordinates.

Comparison to Mayr et al.¹²

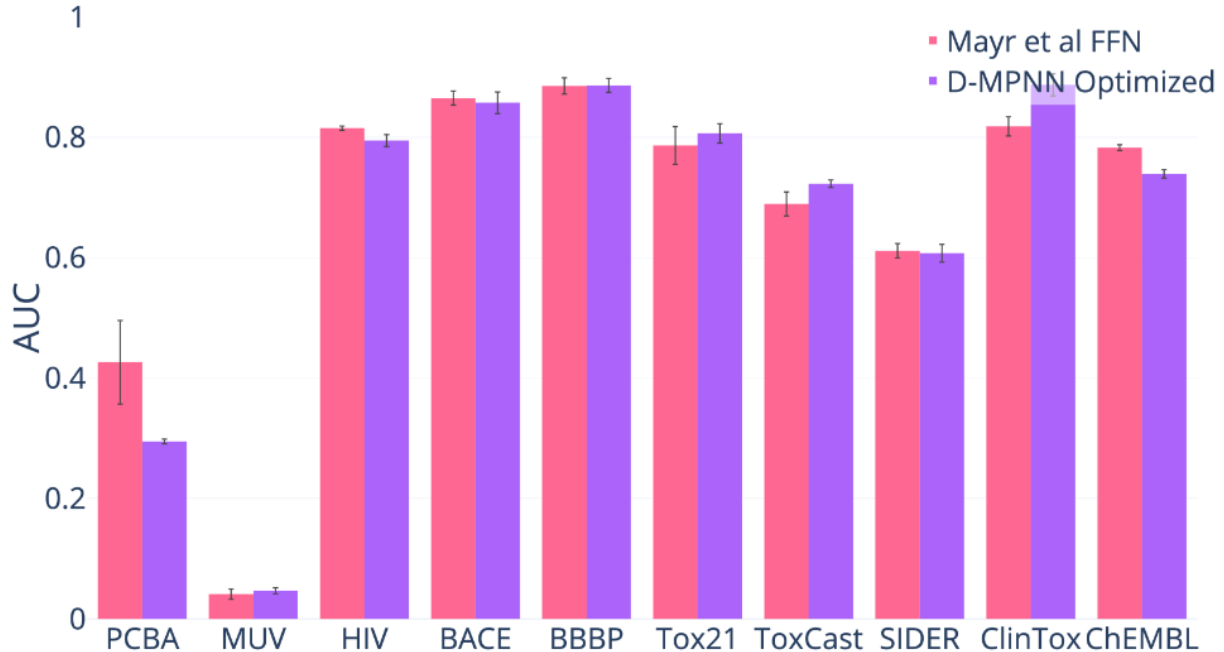
In addition, we compare D-MPNN to the baseline from Mayr et al.¹² in Figure 4. We reproduced the features from their best model on each dataset using their scripts or equivalent packages.⁶³ We then ran their code and hyperparameter optimization directly on the classification datasets, and we modified their code to run on regression datasets with the authors’ guidance.⁶³ On most classification datasets, we obtain similar performance to Mayr et al.¹² On regression datasets, the baseline from Mayr et al.¹² performs poorly in comparison, despite extensive tuning. We hypothesize that this poor performance on regression in comparison to classification is the result of a large number of binary input features to the output feed-forward network; this hypothesis is supported by the similarly poor performance of our Morgan fingerprint FFN baseline. In addition, their method does not employ early stopping based on validation set performance and therefore may overfit to the training data in some cases; this may be the source of some numerical instability.

Out-of-the-Box Comparison of D-MPNN to Other Baselines

For our final baseline comparison, we evaluate our model’s performance “out-of-the-box,” i.e. using all the default settings (hidden size = 300, depth = 3, number of feed-forward layers = 2, dropout = 0) without any hyperparameter optimization and without any additional



(a) Regression Datasets (lower = better).



(b) Classification Datasets (higher = better).

Figure 4: Comparison of our best single model (i.e. optimized hyperparameters and RDKit features) to the model from Mayr et al.. For regression, all but the PDBbind results are statistically significant with $p\text{-value} < 0.05$. For classification, only the result on ClinTox is statistically significant with $p\text{-value} < 0.05$. Although the model from Mayr et al. achieves higher AUC than our model on some classification endpoints, the p -values do not indicate statistical significance.

features. For this comparison, we compare to a number of simple baseline models that use computed fingerprints or descriptors:

1. Random forest (RF) with 500 trees run on Morgan (ECFP) fingerprints using radius 2 and hashing to a bit vector of size 2048.
2. Feed-forward network (FFN) on Morgan fingerprints.
3. FFN on Morgan fingerprints which use substructure counts instead of bits.
4. FFN on RDKit descriptors.

The parameters of the simple baseline models are also out-of-the-box defaults. We make this comparison in order to demonstrate the strong out-of-the-box performance of our model across a wide variety of datasets. Finally, we include the performance of the automatically optimized version of our model as a reference.

Figure 5 shows that even without optimization, our D-MPNN provides an excellent starting point on a wide variety of datasets and targets, though it can be improved further with proper optimization.

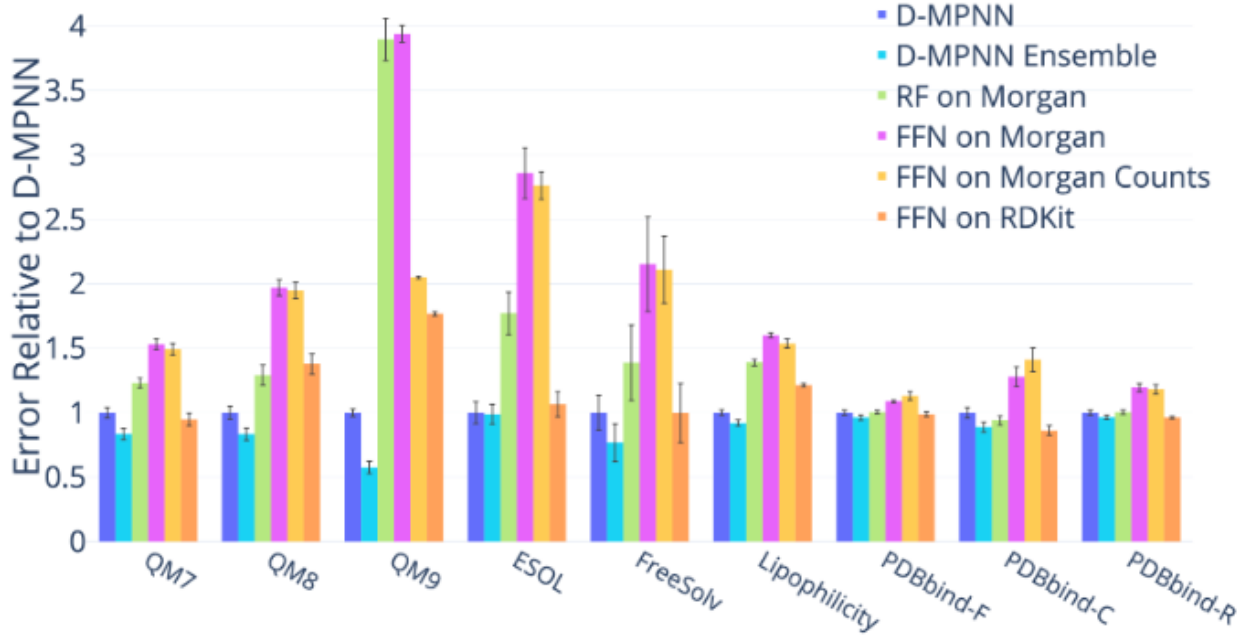
Proprietary Datasets

We also ran our model on several private industry datasets, verifying that our model’s strong performance on public datasets translates to real-world industrial datasets.

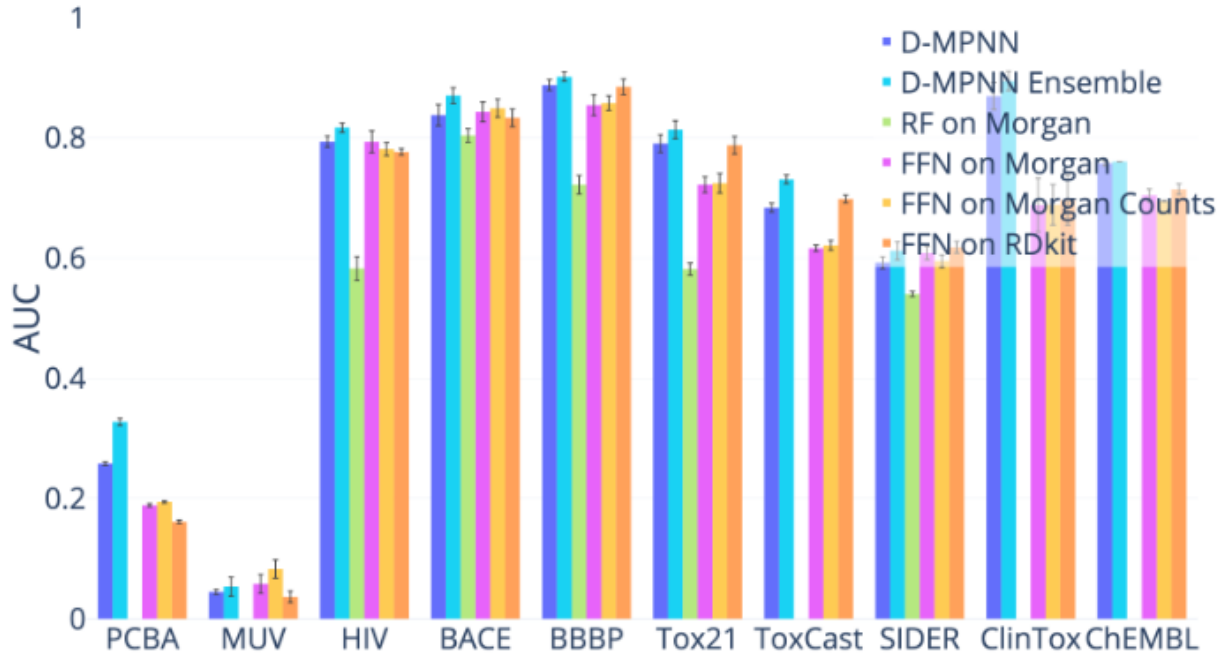
Amgen

We ran our model along with Mayr et al.’s¹² model and our simple baselines on four internal Amgen regression datasets. The datasets are as follows.

1. Rat plasma protein binding free fraction (rPPB).
2. Solubility in 0.01 M hydrochloric acid solution, pH 7.4 phosphate buffer solution, and simulated intestinal fluid (Sol HCL, Sol PBS, and Sol SIF respectively).



(a) Regression Datasets (lower = better).



(b) Classification Datasets (higher = better).

Figure 5: Comparison of our unoptimized D-MPNN against several baseline models. We omitted the random forest baseline on PCBA, MUV, Toxcast, and ChEMBL due to large computational cost. The D-MPNN outperforms all baselines by a statistically significant margin on QM8, QM9, Lipophilicity, PDBbind-Core, PCBA, and ClinTox.

3. Rat liver microsomes intrinsic clearance (RLM).
4. Human pregnane X receptor % activation at 2uM and 10uM (hPXR).

In addition, we binarized the hPXR dataset according to Amgen’s recommendations in order to evaluate on a classification dataset. Details of the datasets are shown in Table 4. Throughout the following, note that rPPB is in logit while Sol and RLM are in \log_{10} .

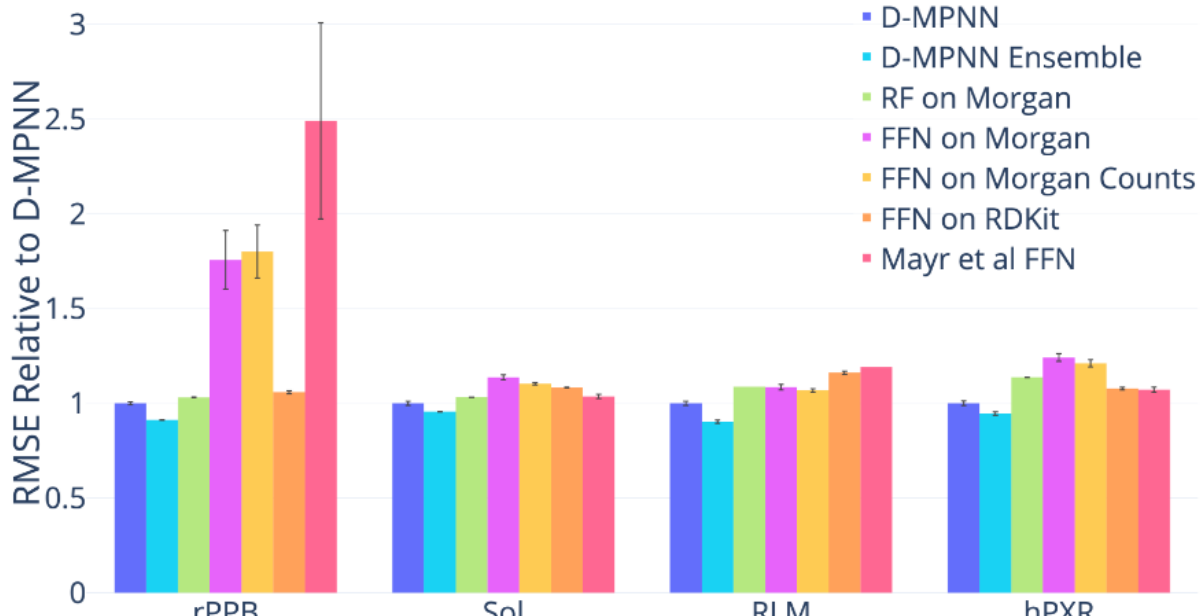
Table 4: Details on internal Amgen datasets. Note: ADME stands for absorption, distribution, metabolism, and excretion.

Category	Dataset	# Tasks	Task Type	# Compounds	Metric
ADME	rPPB	1	Regression	1,441	RMSE
Physical Chemistry	Solubility	3	Regression	18,007	RMSE
ADME	RLM	1	Regression	64,862	RMSE
ADME	hPXR	2	Regression	22,188	RMSE
ADME	hPXR (class)	2	Classification	22,188	ROC-AUC

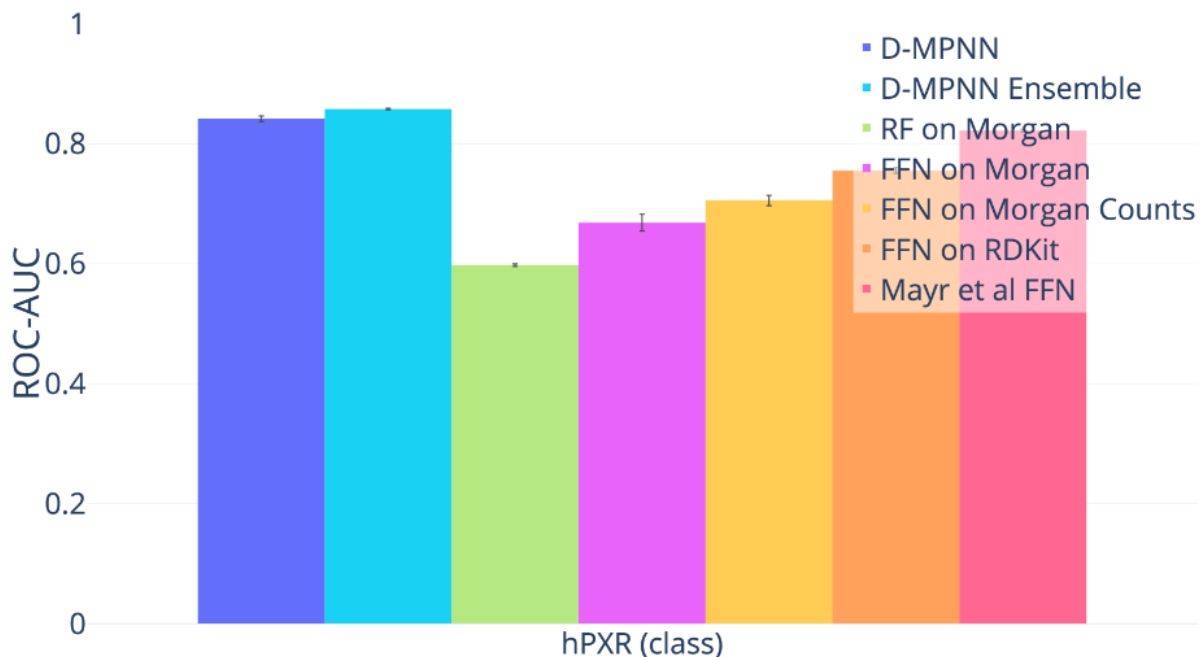
For each dataset, we evaluate on a chronological split. Our model significantly outperforms each individual baseline in at least one case, and does not underperform any baseline on any of the datasets, as shown in Figure 6. Thus our D-MPNN’s strong performance on scaffold splits of public datasets can translate well to chronological splits of private industry datasets.

BASF

We ran our model on 10 highly related quantum mechanical datasets from BASF. Each dataset contains 13 properties calculated on the same 30,733 molecules, varying the solvent in each dataset. Dataset details are in Table 5.



(a) Regression Datasets (lower = better).



(b) Classification Datasets (higher = better).

Figure 6: Comparison of our D-MPNN against baseline models on Amgen internal datasets on a chronological data split. D-MPNN outperforms each individual baseline by a statistically significant margin on at least one of the datasets, and is never worse. Note that the ensembles were ensembles of 3 models rather than 5 for the Amgen datasets only. Also note that RF on Morgan and Mayr et al FFN were only run once on RLM.

Table 5: Details on internal BASF datasets. Note: R^2 is the square of Pearson’s correlation coefficient.

Category	Dataset	Tasks	Task Type	# Compounds	Metric
Quantum Mechanics	Benzene	13	regression	30,733	R^2
Quantum Mechanics	Cyclohexane	13	regression	30,733	R^2
Quantum Mechanics	Dichloromethane	13	regression	30,733	R^2
Quantum Mechanics	DMSO	13	regression	30,733	R^2
Quantum Mechanics	Ethanol	13	regression	30,733	R^2
Quantum Mechanics	Ethyl acetate	13	regression	30,733	R^2
Quantum Mechanics	H ₂ O	13	regression	30,733	R^2
Quantum Mechanics	Octanol	13	regression	30,733	R^2
Quantum Mechanics	Tetrahydrofuran	13	regression	30,733	R^2
Quantum Mechanics	Toluene	13	regression	30,733	R^2

For these datasets, we used a scaffold-based split because a chronological split was unavailable. We found that the model of Mayr et al.¹² is numerically unstable on these datasets, and we therefore omit it from the comparison below. Once again we find that our model, originally designed to succeed on a wide range of public datasets, is robust enough to transfer to proprietary datasets: D-MPNN models significantly outperform our other baselines, as shown in Figure 7.

Novartis

Finally, we ran our model on one proprietary dataset from Novartis as described in Table 6. As with other proprietary datasets, our D-MPNN outperforms the other baselines as shown in Figure 8.

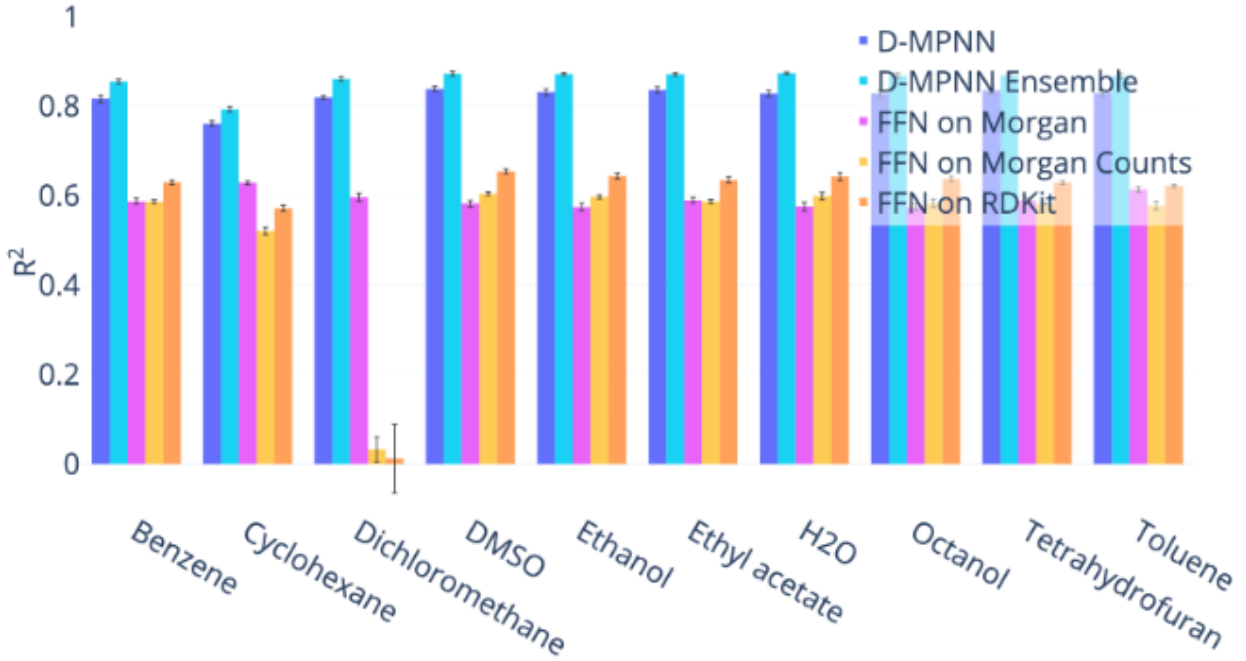


Figure 7: Comparison of our D-MPNN against baseline models on BASF internal regression datasets on a scaffold data split (higher = better). Our D-MPNN significantly outperforms all baselines, with p-value less than 0.02 for each pairwise comparison.

Table 6: Details on the internal Novartis dataset.

Category	Dataset	Tasks	Task Type	# Compounds	Metric
Physical Chemistry	logP	1	regression	20,294	RMSE

Experimental Error

As a final “oracle” baseline, we compare our model’s performance with to an experimental upper upper bound: the agreement between multiple runs of the same assay, which we refer to as the *experimental error*. Figure 9 shows the R^2 of our model on the private Amgen regression datasets together with the experimental error; in addition, this graph shows the performance of Amgen’s internal model using expert-crafted descriptors. Both models remain far less accurate than the corresponding ground truth assays. Thus there remains significant space for further performance improvement in the future.

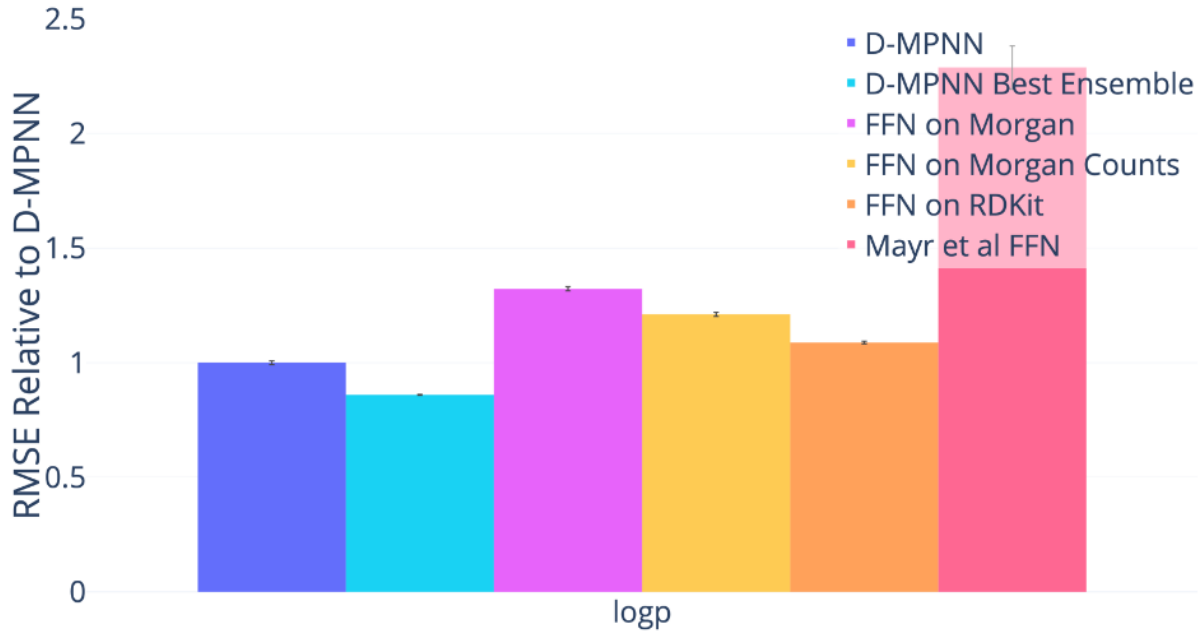


Figure 8: Comparison of our D-MPNN against baseline models on the Novartis internal regression dataset on a chronological data split (lower = better). Our D-MPNN outperforms all baseline models with p-value less than 0.001.

Analysis of Split Type

We now justify our use of scaffold splits for performance evaluation. The ultimate goal of building a property prediction model is to predict properties on new chemistry in order to aid the search for drugs from new classes of molecules. On proprietary company datasets, performance on new chemistry is evaluated using a chronological split of the data, i.e., everything before a certain date serves as the training set while everything after that date serves as the test set. This approximates model performance on molecules that chemists are likely to investigate in the future. Since chronological data is typically unavailable for public datasets, we investigate whether we can use our scaffold split as a reasonable proxy for a chronological split, following the work of Sheridan.¹³

Figure 10 provides motivation for a scaffold split approach. As illustrated in the figure, train and test sets according to a chronological split share significantly fewer molecular scaffolds than train and test sets split randomly. Since our scaffold split enforces zero molecular

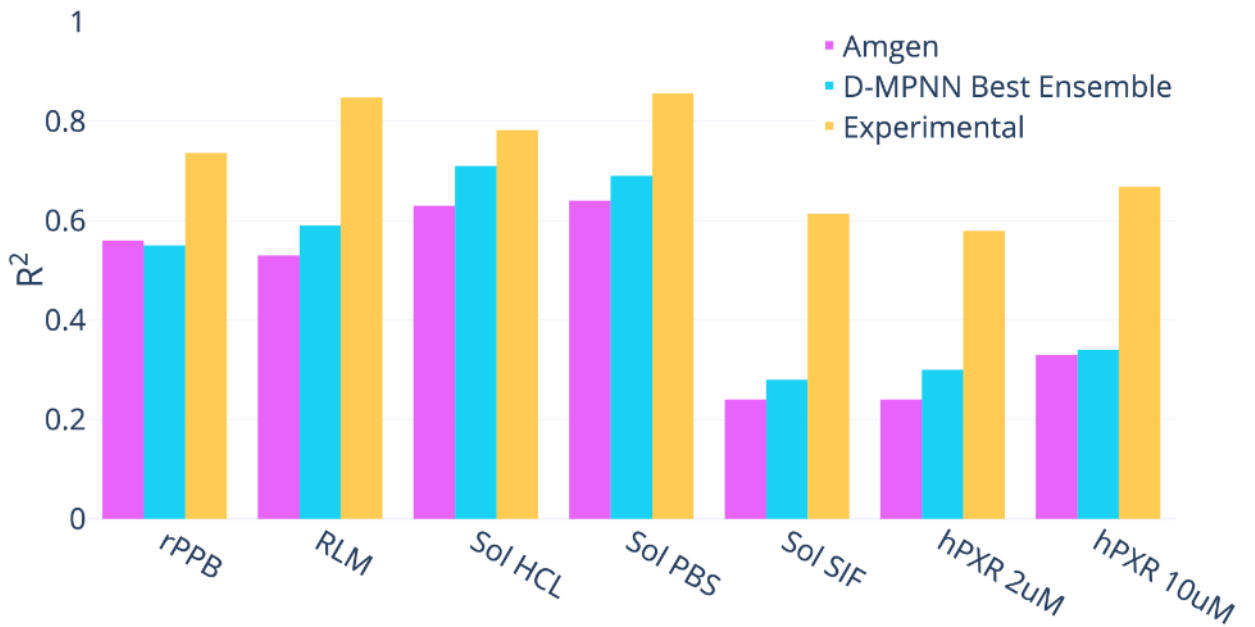


Figure 9: Comparison of Amgen’s internal model and our D-MPNN (evaluated using a single run on a chronological split) to experimental error (higher = better). Note that the experimental error is not evaluated on the exact same time split as the two models since it can only be measured on molecules which were tested more than once, but even so the difference in performance is striking.

scaffold overlap between the train and test set, it should ideally provide a split that is at least as difficult as a chronological split.

As illustrated in Figures 11, 12, and 13, performance on our scaffold split is on average closer to performance on a chronological split on proprietary datasets from Amgen and Novartis and on the public PDBBind datasets. However, results are noisy due to the nature of chronological splitting, where we only have a single data split (as opposed to random and scaffold splitting, which both have a random component and can generate different splits depending on the random seed)⁵. Figure 14 shows the difference between a random split and a scaffold split on the publicly available datasets, further demonstrating that a scaffold split generally results in a more difficult, and ideally more useful, measure of performance. Therefore, all of our results are reported on a scaffold split rather than a random split in order to better reflect the generalization ability of our model on new chemistry. Nevertheless, it should be emphasized that the chronological split is still the ideal split on which to evaluate when it is available. Thus we additionally report the results on chronological splits on all datasets where they are available.

Overall, our results confirm the findings of Sheridan¹³ that scaffold and chronological splits are more difficult than random splits, and hence scaffold splits should be preferred over random splits during evaluation. While we provide some evidence that chronological splits may actually be harder than scaffold splits, in contrast with the findings of Sheridan,¹³ we show statistical significance in only a few datasets, owing to the small number of datasets where chronological splits are available. Hence further investigation is necessary on this point, ideally on a larger range of datasets.

Ablations

Finally, we analyze and justify our modeling choices and optimizations.

⁵We can alleviate the problem with noise in chronological datasets by using a sliding time window to get different equally-sized splits, at the cost of significantly decreasing the dataset size. We report results on such sliding window splits in the Supporting Information, as the conclusions from these splits are qualitatively similar to those in the main paper.

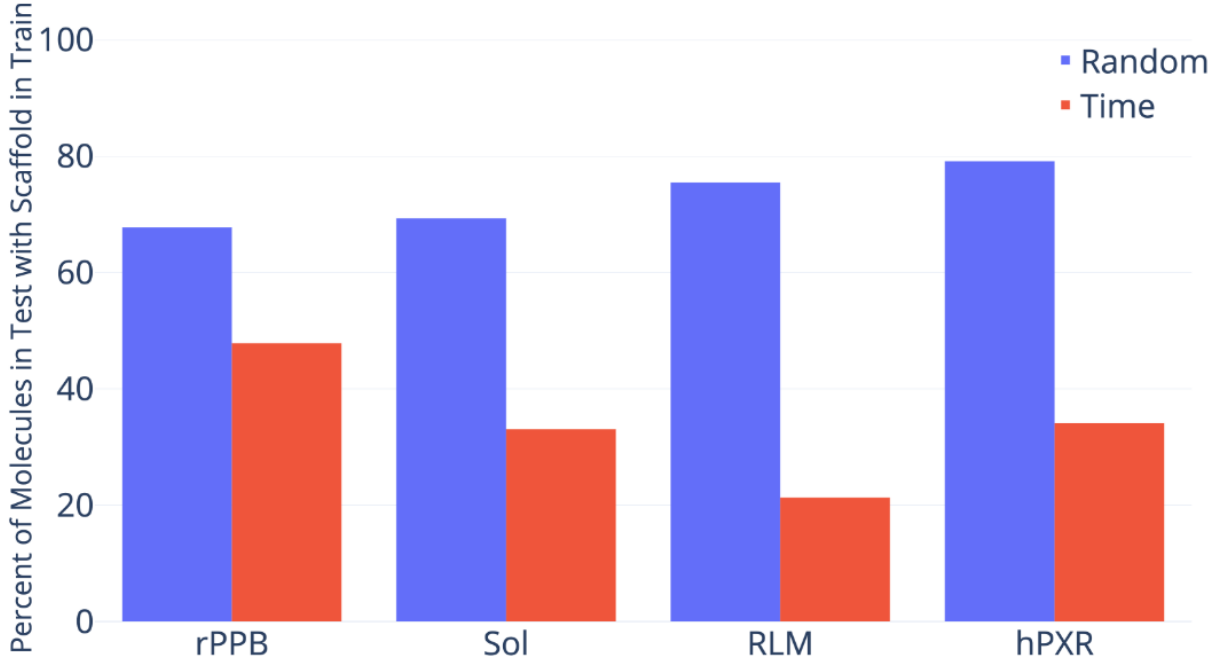


Figure 10: Overlap of molecular scaffolds between the train and test sets for a random or chronological split of four Amgen regression datasets. Overlap is defined as the percent of molecules in the test set which share a scaffold with a molecule in the train set.

Message Type

The most important distinction between our D-MPNN and related work is the nature of the messages being passed across the molecule. Most prior work uses messages centered on atoms whereas our D-MPNN uses messages centered on directed bonds. To isolate the effect of the message passing paradigm on property prediction performance, we implemented message passing on undirected bonds and on atoms as well, as detailed in the Supporting Information and in our code. Figure 15 illustrates the differences in performance between these three types of message passing. While on average the method using directed bonds outperforms the alternatives, the results are largely not statistically significant, so more investigation is warranted on this point.

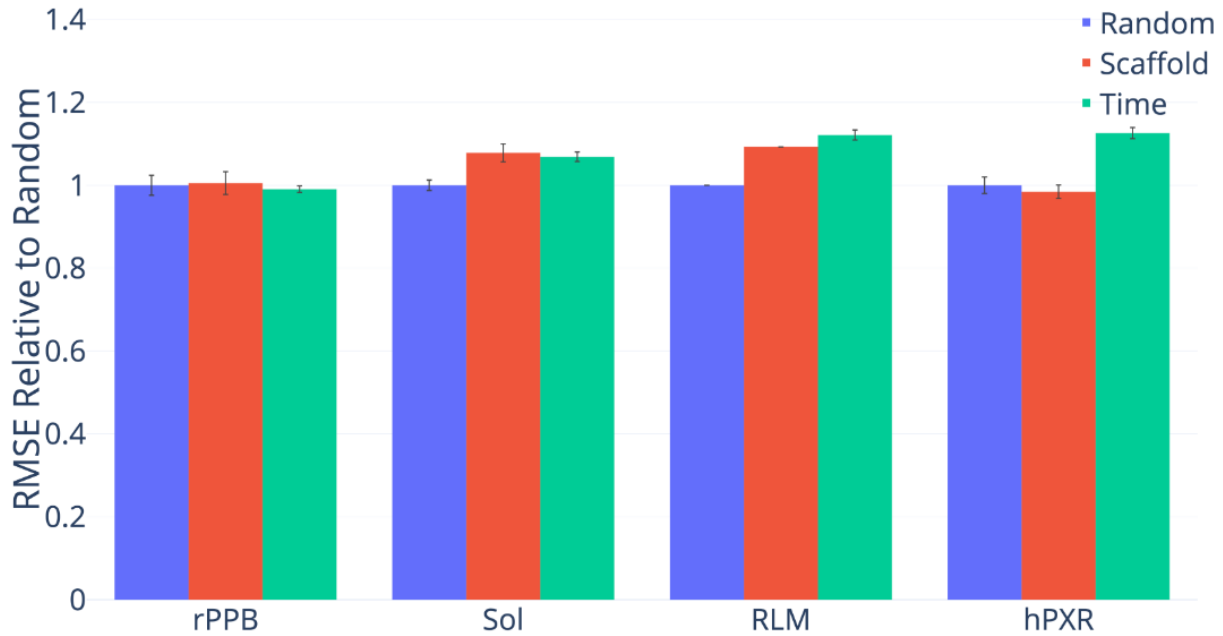


Figure 11: Performance of D-MPNN on four Amgen regression datasets according to three methods of splitting the data (lower = better). The chronological split is significantly harder than both random and scaffold on Sol and hPXR, while the scaffold split is significantly harder than the random split on Sol only.

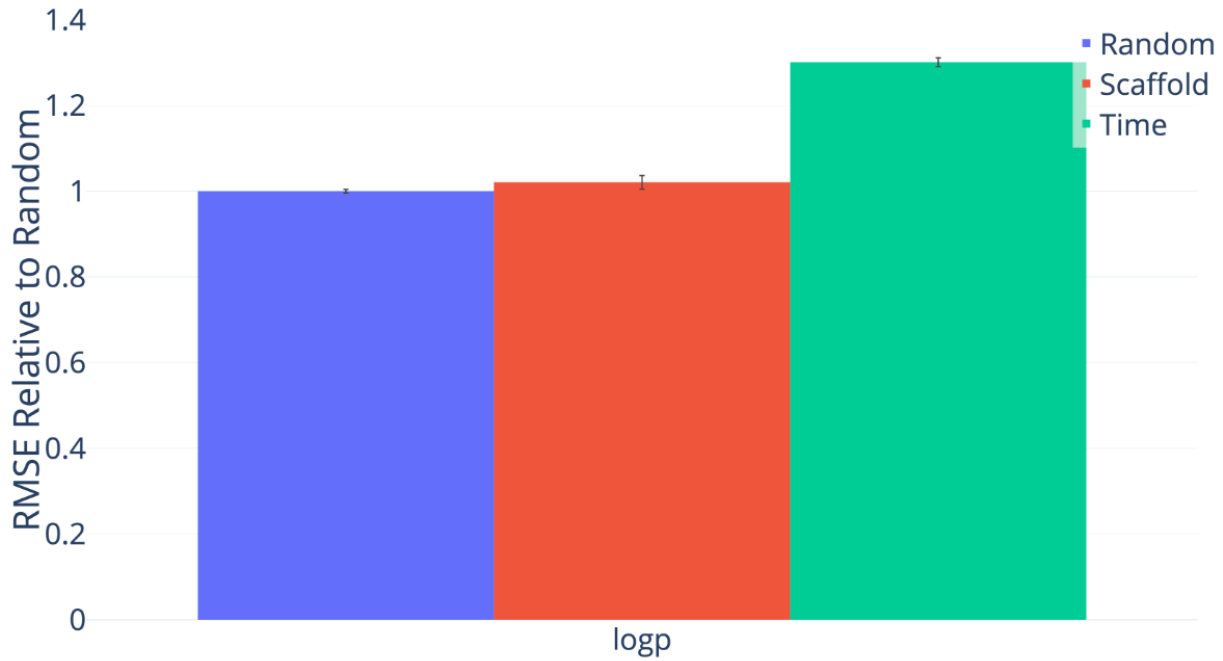


Figure 12: Performance of D-MPNN on the Novartis regression dataset according to three methods of splitting the data (lower = better). All pairwise comparisons are statistically significant.

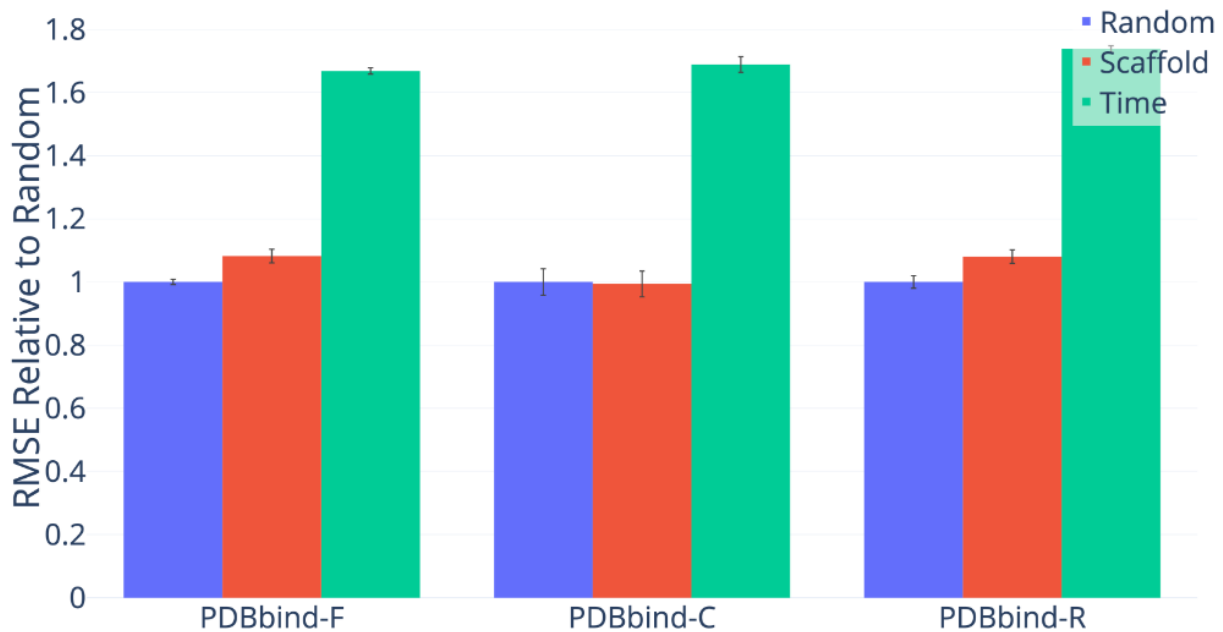
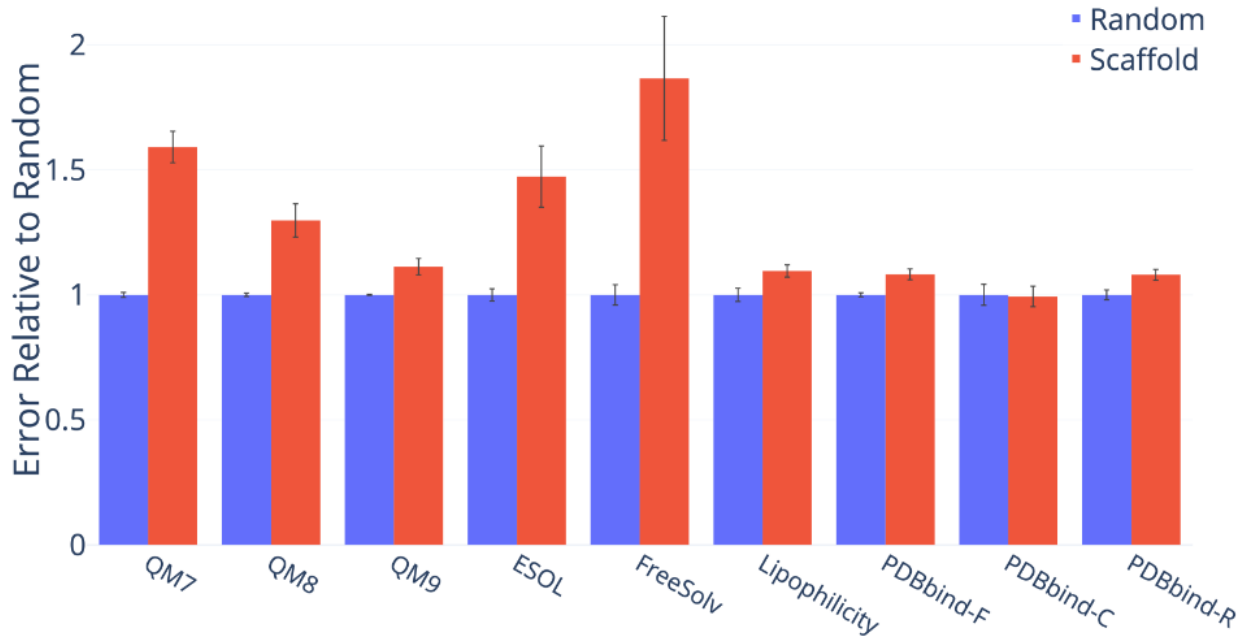
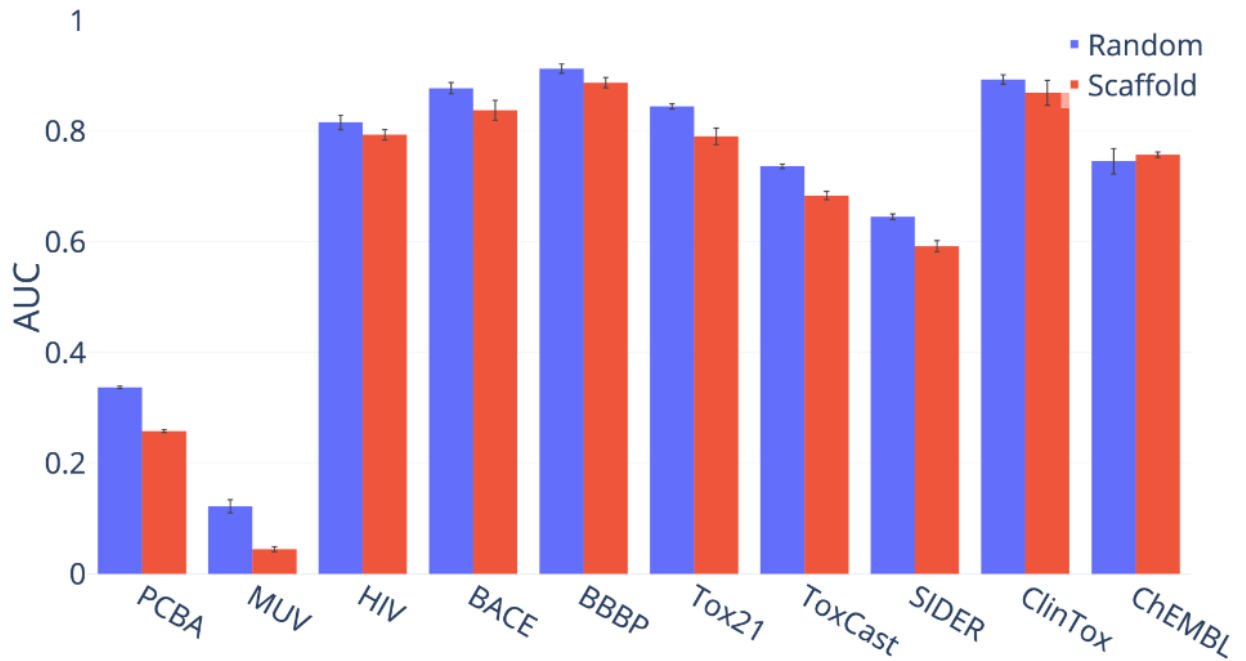


Figure 13: Performance of D-MPNN on the full (F), core (C), and refined (R) subsets of the PDBBind dataset according to three methods of splitting the data (lower = better). All pairwise differences are statistically significant with the exception of scaffold and random splits on PDBbind-C.



(a) Regression Datasets (lower = better).

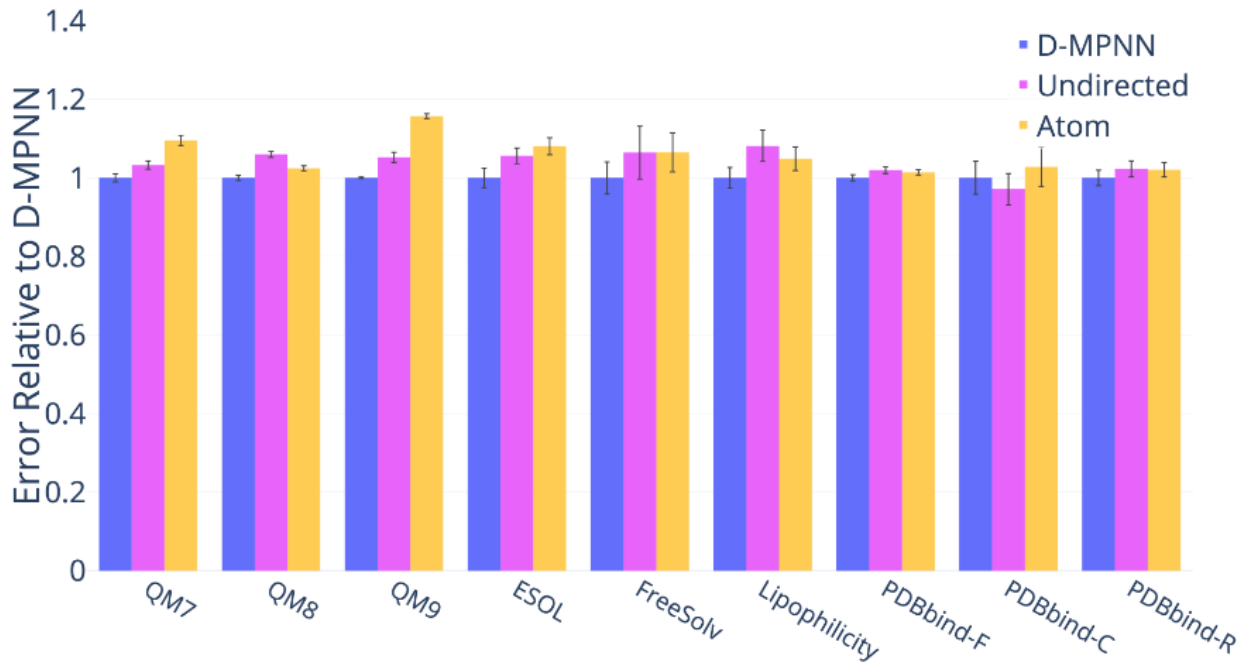


(b) Classification Datasets (higher = better).

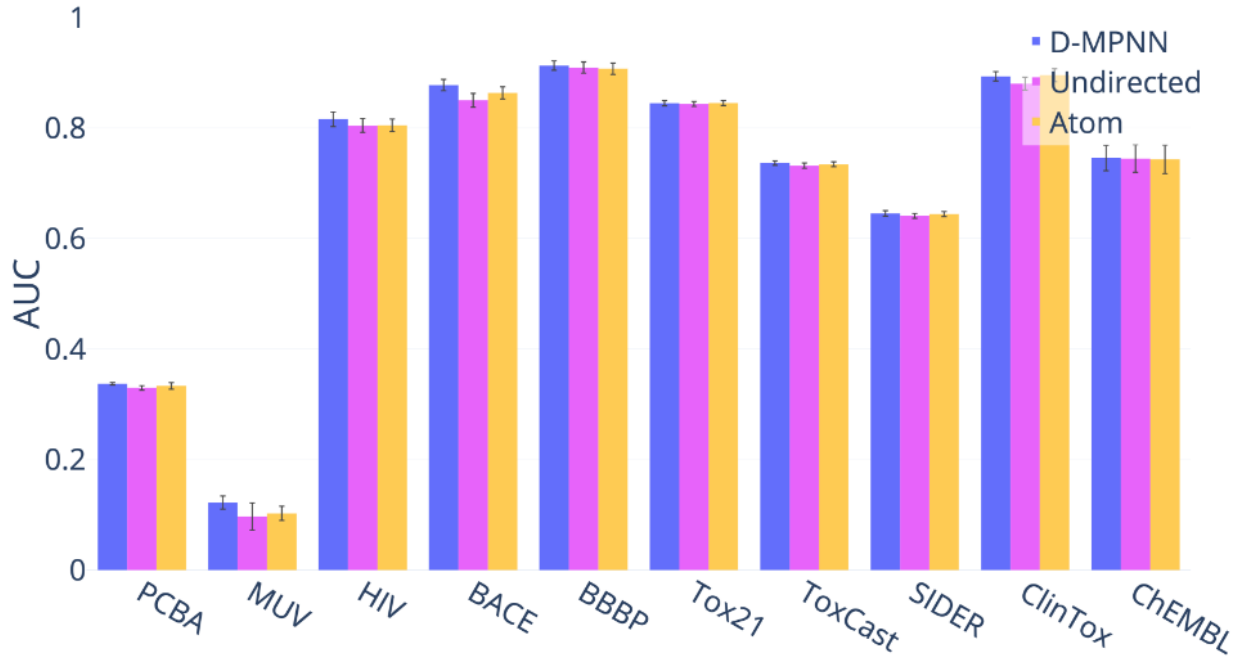
Figure 14: Performance of D-MPNN on random and scaffold splits for several public datasets. Only the results on PDBbind-Core, HIV, and ChEMBL are not statistically significant.

RDKit Features

Next, we examined the impact of adding additional molecule-level features from RDKit to our model. Figure 16 shows the effect on model performance. The results appear to be highly dataset-dependent. Some datasets, such as QM9 and ESOL, show marked improvement with the addition of features, while other datasets, such as PCBA and HIV, actually show worse performance with the features. We hypothesize that this is because the features are particularly relevant to certain tasks while possibly confusing and distracting the model on other tasks. This implies that our model’s performance on a given dataset may be further optimized by selecting different features more relevant to the task of interest.



(a) Regression Datasets (lower = better).



(b) Classification Datasets (higher = better).

Figure 15: Comparison of performance of different message passing paradigms.

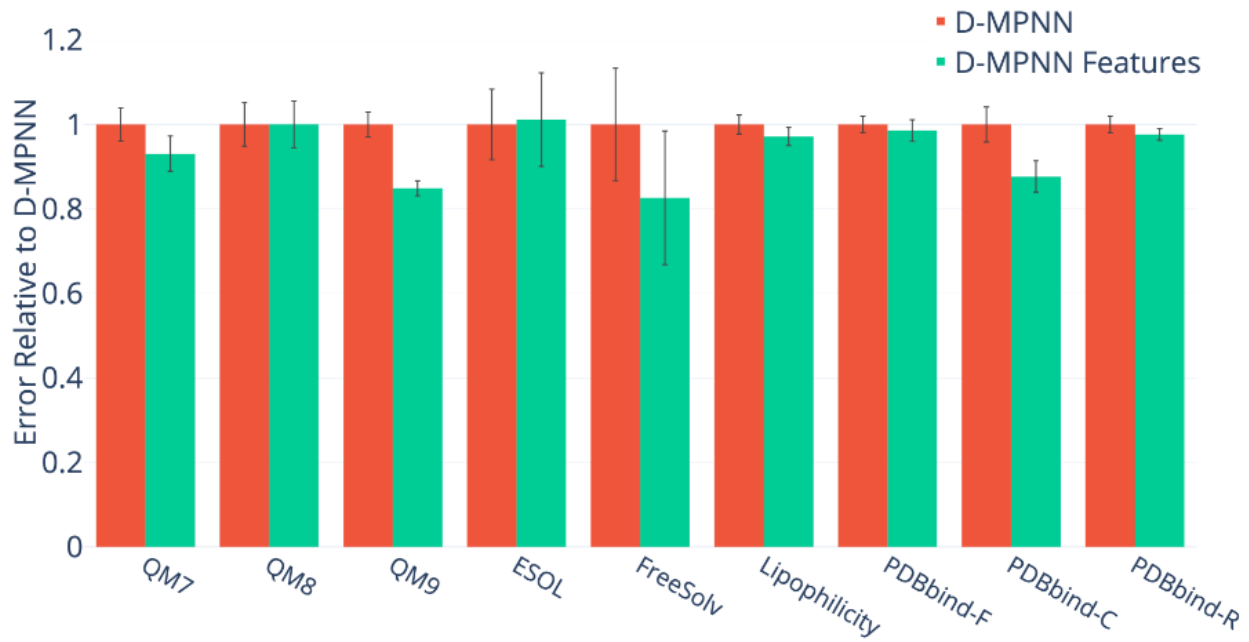
Another interesting trend is the effect of adding features to the three PDBbind datasets. The features appear to help on all three datasets, but the benefit is much more pronounced on the extremely small PDBbind-C (core) dataset than it is on the larger PDBbind-R (refined) and PDBbind-F (full) datasets. This indicates that the features may help compensate for the lack of training data and thus may be particularly relevant in low-data regimes. In particular, we hypothesize that the features may help to regularize a representation derived from a small dataset: because the features are derived from more general chemical knowledge, they implicitly provide the model some understanding of a larger chemical domain. Thus, it is worthwhile to consider the addition of features both when they are particularly relevant to the task of interest and when the dataset is especially small.

Hyperparameter Optimization

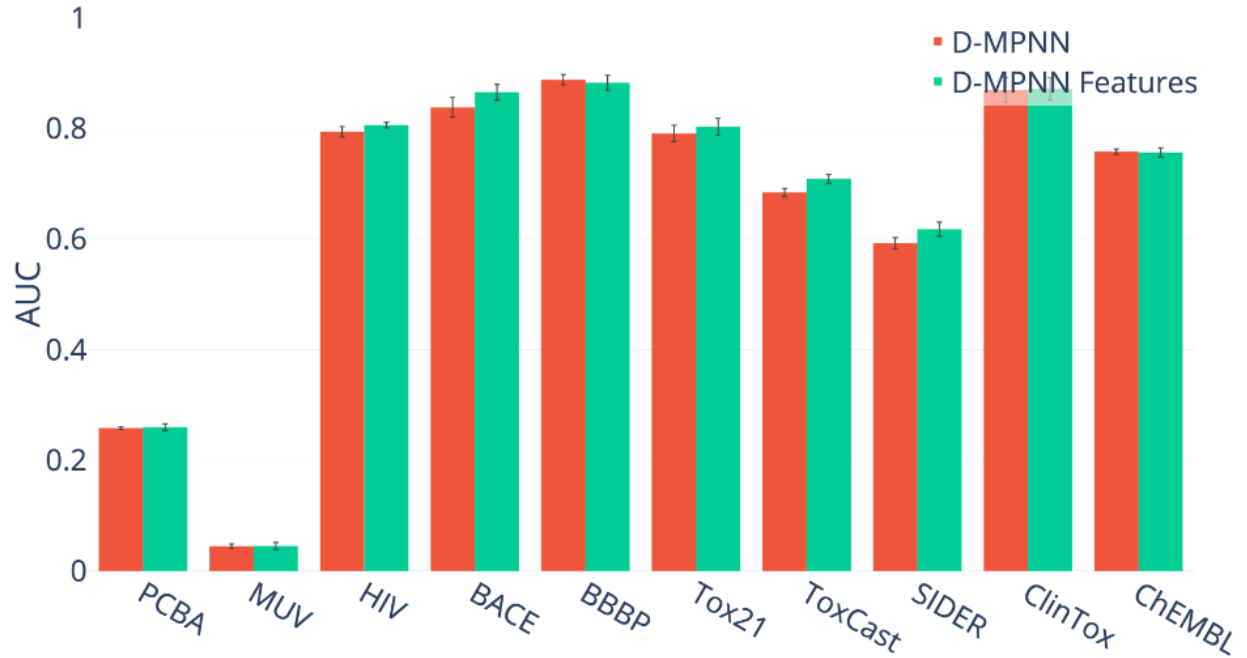
To improve model performance, we performed Bayesian Optimization to select the best model hyperparameters for each dataset. Figure 17 illustrates the benefit of performing this optimization, as model performance improves on virtually every dataset. Interestingly, some datasets are particularly sensitive to hyperparameters. While most datasets experience a moderate 2-5% improvement in performance following hyperparameter optimization, the quantum mechanics datasets (QM7, QM8, and QM9) and PCBA see dramatic improvements in performance, with our D-MPNN model performing 37% better on QM9 after optimization.

Ensembling

To maximize performance, we trained an ensemble of models. For each dataset, we selected the best single model—i.e. the best hyperparameters along with the RDKit features if the features improved performance—and we trained five models instead of one. The results appear in Figure 19. On most datasets, ensembling only provides a small 1-5% benefit, but as with hyperparameter optimization, there are certain datasets, particularly the quantum mechanics datasets, which especially benefit from the effect of ensembling.

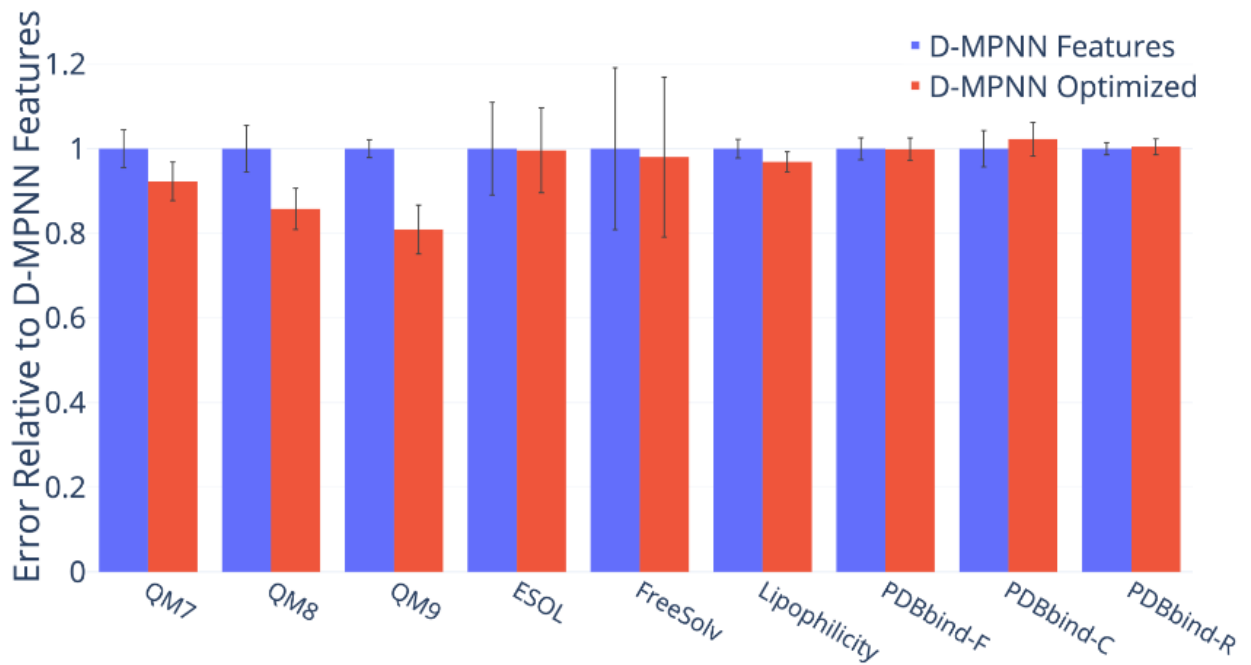


(a) Regression Datasets (lower = better).

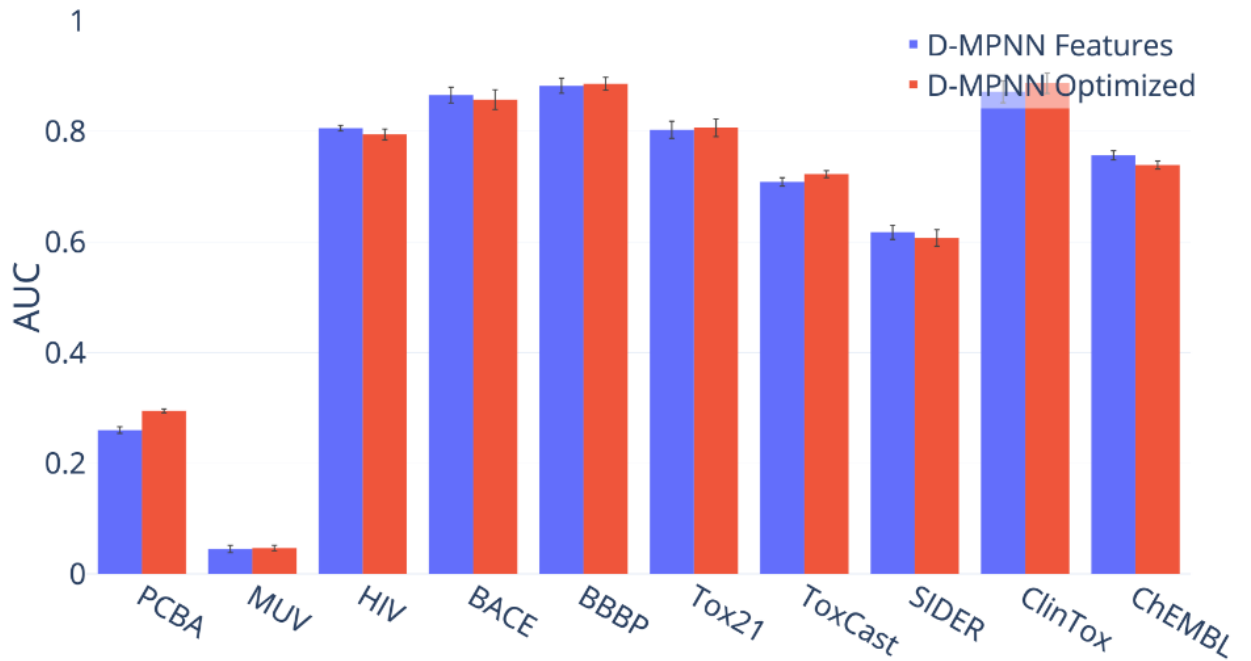


(b) Classification Datasets (higher = better).

Figure 16: Effect of adding molecule-level features generated with RDKit to our model.



(a) Regression Datasets (lower = better).



(b) Classification Datasets (higher = better).

Figure 17: Effect of performing Bayesian hyperparameter optimization on the depth, hidden size, number of fully connected layers, and dropout of the D-MPNN.

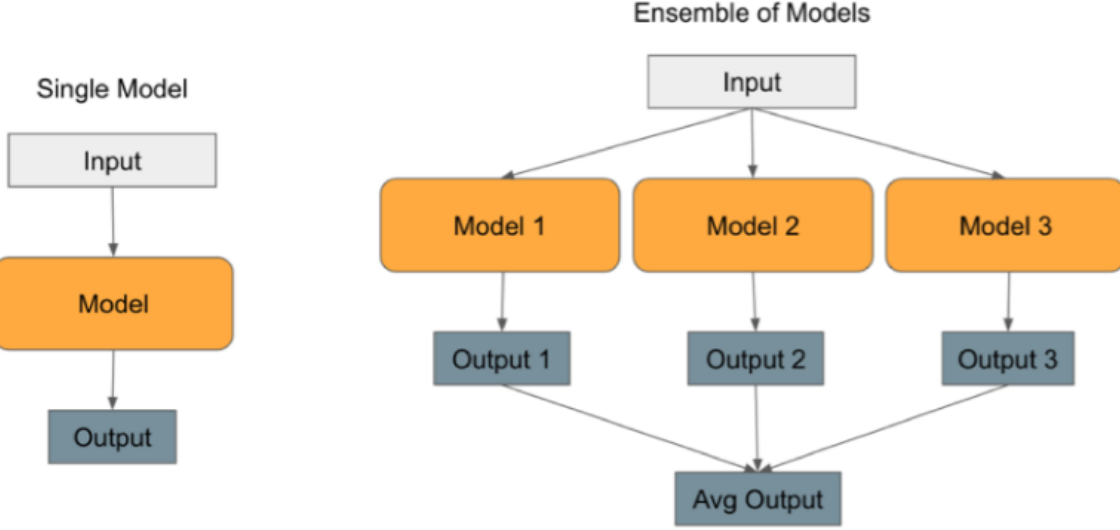
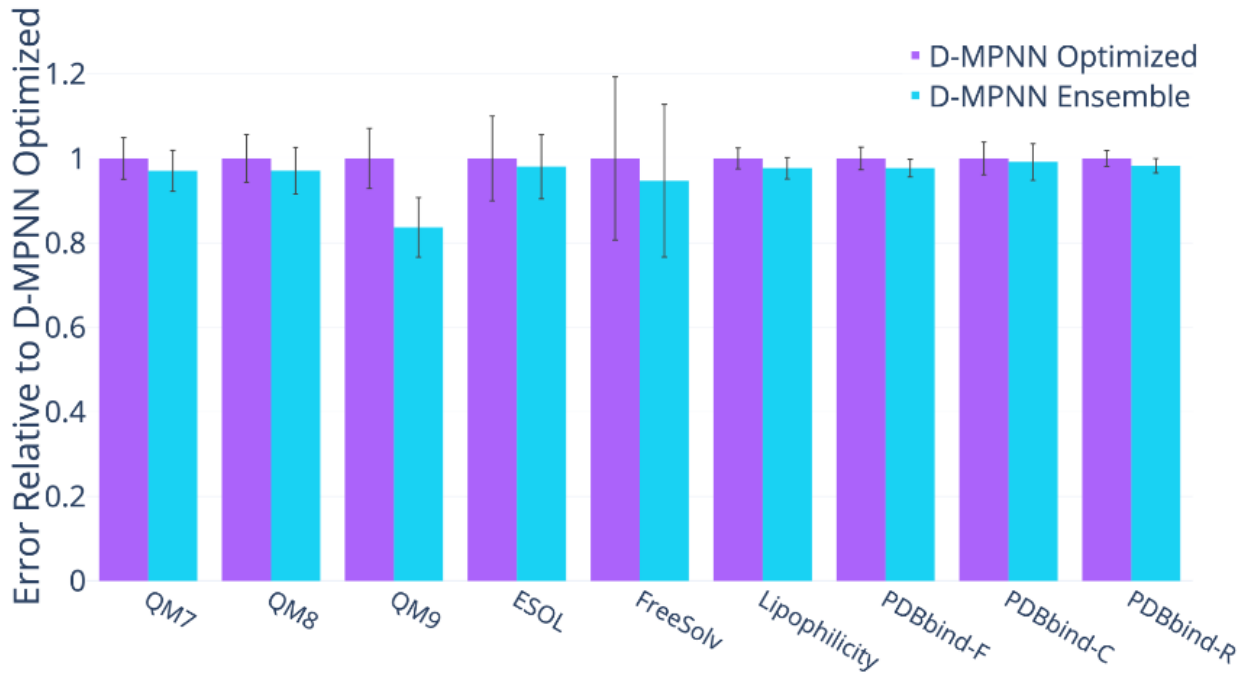


Figure 18: An illustration of ensembling models. On the left is a single model, which takes input and makes a prediction. On the right is an ensemble of 3 models. Each model takes the same input and makes a prediction independently, and then the predictions are averaged to generate the ensemble’s prediction.

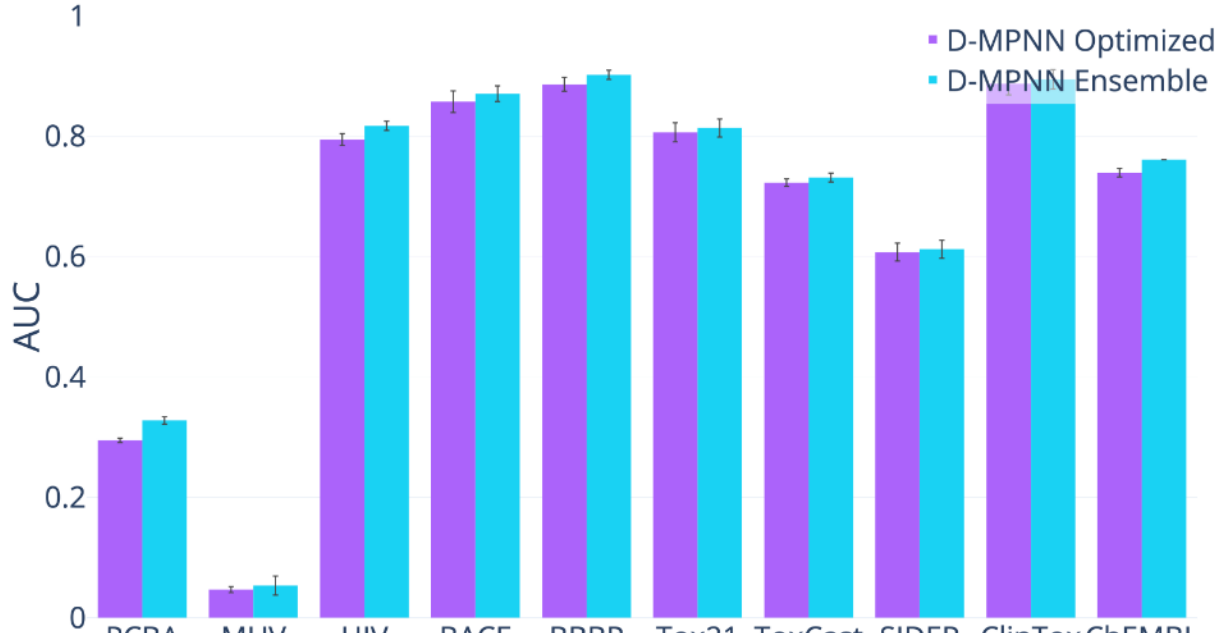
While each of the latter three optimizations (RDKit descriptors, hyperparameter optimization, and ensembling) mostly do not produce statistically significant differences on their own, altogether they improve the model’s performance with p-value less than 0.05 on 7 out of 19 public datasets.

Effect of Data Size

Finally, we analyze the effect of data size on the performance of our model, using the ChEMBL dataset. ChEMBL is a large dataset of 456,331 molecules on 1,310 targets, but is extremely sparse: only half of the 1,310 targets have at least 300 labels. For this analysis, we use the original scaffold-based split of Mayr et al.,¹² containing 3 cross-validation folds. From Figure 20, we hypothesize that our D-MPNN struggles on low-label targets in comparison to this baseline. As our D-MPNN model does not use any human-engineered fingerprints or descriptors and must therefore learn its features completely from scratch based on the input data, it would be unsurprising if the average ROC-AUC score of D-MPNN is worse than



(a) Regression Datasets (lower = better).



(b) Classification Datasets (higher = better).

Figure 19: Effect of using an ensemble of five models instead of a single model.

that of the feed-forward network running on human-engineered descriptors in Mayr et al.¹². When we filter the ChEMBL dataset by pruning low-data targets at different thresholds, we find that our D-MPNN indeed may outperform the best model of Mayr et al.¹² at larger data thresholds (Figure 20), though our results are not fully conclusive.

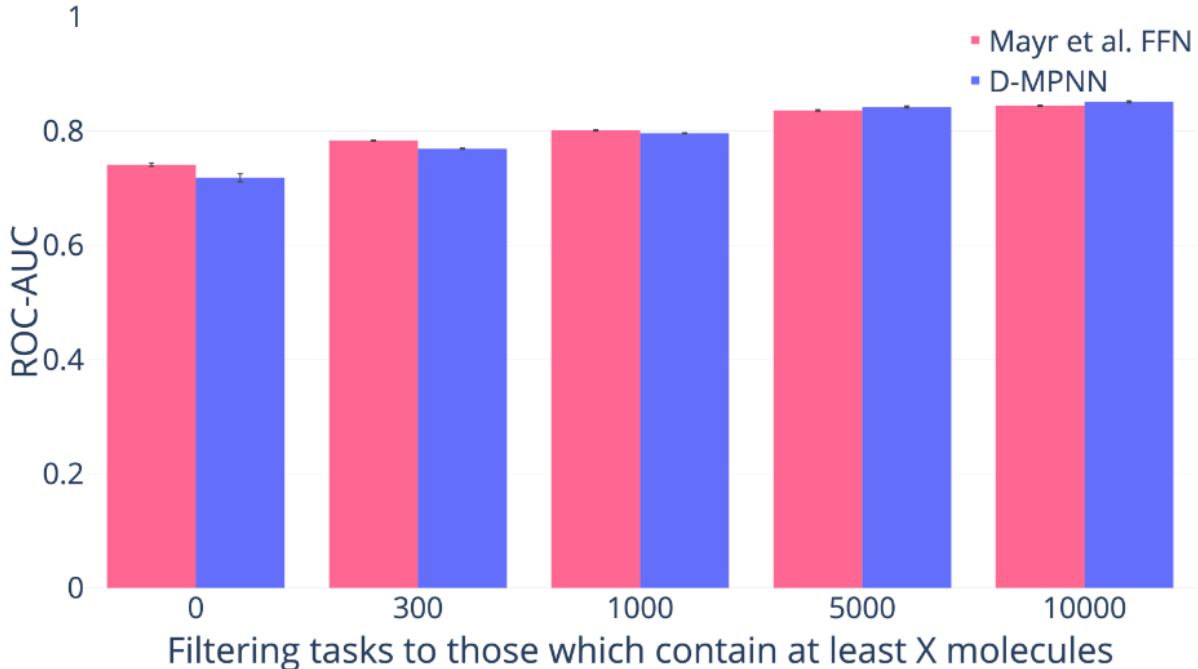


Figure 20: Effect of data size on the performance of the model from Mayr et al.¹² and of our D-MPNN model (higher = better). Although this analysis is not fully conclusive, we note that p-values for statistical significance range from 0.01 to 0.10.

Conclusion and Future Work

In this paper, we performed an extensive comparison of molecular property prediction models based on either fixed descriptors or learned molecular representations, evaluating these models on both public and proprietary datasets. We also introduced a directed bond-based message passing neural network architecture, the D-MPNN, which outperforms existing strong baselines on public datasets and achieves similarly strong results on proprietary datasets. Furthermore, our model’s performance on scaffold-based data splits illustrates its ability to

generalize to new classes of molecules. These results indicate that learned molecular representations are indeed ready for “prime time” use in industrial property prediction settings.

Several important avenues of future research remain which hold the potential to significantly improve our model’s efficacy and utility. The first is the incorporation of additional 3D information into our model, which currently includes only a very restricted and naive representation of such features. On datasets where 3D structural information is available, our model sometimes underperforms previous baselines when those baselines are allowed access to 3D features. The second avenue of improvement is a principled pretraining approach, which some authors have already begun to explore.^{64,65} Such an approach could enable models to transfer learning from large chemical datasets to much smaller datasets, thereby improving performance in limited data settings. Finally, our increased understanding of how estimation of model generalizability is affected by split type opens the door to future work in uncertainty quantification and domain of applicability assessment.

Acknowledgement

We thank MIT, the Machine Learning for Pharmaceutical Discovery and Synthesis (MLPDS) consortium, Amgen Inc., BASF, and Novartis for funding this research. The MIT authors are funded by MIT, in particular the MLPDS consortium; the authors at companies are funded by their respective organizations. The authors declare no competing financial interest.

We would like to thank the other members of the computer science and chemical engineering groups in the Machine Learning for Pharmaceutical Discovery and Synthesis consortium for their helpful feedback throughout the research process. We would also like to thank the other industry members of the consortium for useful discussions regarding how to use our model in a real-world setting. We thank Nadine Schneider and Niko Fechner at Novartis for helping to analyze our model on internal Novartis data and for feedback on the manuscript. We thank Ryan White, Stephanie Geuns-Meyer, and Florian Boulnois at Amgen Inc. for

their help enabling us to run experiments on Amgen datasets. In addition, we thank Lior Hirschfeld for his work on our web-based user interface.⁵³ Finally, we thank Zhenqin Wu for his aid in recreating the original data splits of Wu et al.,² and we thank Andreas Mayr for helpful suggestions regarding adapting the model from Mayr et al.¹² to new classification and regression datasets.

Supporting Information Available

The following files are available free of charge.

In our Supporting Information, we provide links to our code and to a demonstration of our web-based user interface. We also provide further comparisons of model performance on both scaffold-based and random splits of the data, and we provide tables with all raw performance numbers (including p-values) which appear in the charts in this paper. In addition, we analyze the class balance of classification datasets, and we provide a list of the RDKit calculated features used by our model.

References

- (1) Duvenaud, D. K.; Maclaurin, D.; Iparraguirre, J.; Bombarell, R.; Hirzel, T.; Aspuru-Guzik, A.; Adams, R. P. Convolutional Networks on Graphs for Learning Molecular Fingerprints. *Advances in Neural Information Processing Systems* **2015**, 2224–2232.
- (2) Wu, Z.; Ramsundar, B.; Feinberg, E.; Gomes, J.; Geniesse, C.; Pappu, A. S.; Leswing, K.; Pande, V. MoleculeNet: A Benchmark for Molecular Machine Learning. *Chem. Sci.* **2018**, *9*, 513530.
- (3) Kearnes, S.; McCloskey, K.; Berndl, M.; Pande, V.; Riley, P. Molecular Graph Convolutions: Moving Beyond Fingerprints. *J. Comput.-Aided Mol. Des.* **2016**, *30*, 595–608.

(4) Gilmer, J.; Schoenholz, S. S.; Riley, P. F.; Vinyals, O.; Dahl, G. E. Neural Message Passing for Quantum Chemistry. *Proceedings of the 34th International Conference on Machine Learning* **2017**,

(5) Li, Y.; Tarlow, D.; Brockschmidt, M.; Zemel, R. Gated Graph Sequence Neural Networks. *arXiv preprint arXiv:1511.05493* **2015**,

(6) Kipf, T. N.; Welling, M. Semi-Supervised Classification with Graph Convolutional Networks. *arXiv preprint arXiv:1609.02907* **2016**,

(7) Defferrard, M.; Bresson, X.; Vandergheynst, P. Convolutional Neural Networks on Graphs with Fast Localized Spectral Filtering. *Advances in Neural Information Processing Systems* **2016**, 3844–3852.

(8) Bruna, J.; Zaremba, W.; Szlam, A.; LeCun, Y. Spectral Networks and Locally Connected Networks on Graphs. *arXiv preprint arXiv:1312.6203* **2013**,

(9) Coley, C. W.; Barzilay, R.; Green, W. H.; Jaakkola, T. S.; Jensen, K. F. Convolutional Embedding of Attributed Molecular Graphs for Physical Property Prediction. *J. Chem. Inf. Model.* **57**, 1757–1772.

(10) Schütt, K. T.; Arbabzadah, F.; Chmiela, S.; Müller, K. R.; Tkatchenko, A. Quantum-Chemical Insights from Deep Tensor Neural Networks. *Nat. Commun.* **2017**, *8*, 13890.

(11) Battaglia, P.; Pascanu, R.; Lai, M.; Rezende, D. J. Interaction Networks for Learning about Objects, Relations and Physics. *Advances in Neural Information Processing Systems* **2016**, 4502–4510.

(12) Mayr, A.; Klambauer, G.; Unterthiner, T.; Steijaert, M.; Wegner, J. K.; Ceulemans, H.; Clevert, D.-A.; Hochreiter, S. Large-Scale Comparison of Machine Learning Methods for Drug Target Prediction on ChEMBL. *Chem. Sci.* **2018**, *9*, 5441–5451.

(13) Sheridan, R. P. The relative importance of domain applicability metrics for estimating prediction errors in QSAR varies with training set diversity. *J. Chem. Inf. Model.* **2015**, *55*, 1098–1107.

(14) Shahriari, B.; Swersky, K.; Wang, Z.; Adams, R. P.; de Freitas, N. Taking the Human Out of the Loop: A Review of Bayesian Optimization. *Proceedings of the IEEE* **2016**, *104*, 148–175.

(15) Dietterich, T. G. Ensemble Methods in Machine Learning. *International Workshop on Multiple Classifier Systems* **2000**, 1–15.

(16) Hamilton, W.; Ying, Z.; Leskovec, J. Inductive Representation Learning on Large Graphs. *Advances in Neural Information Processing Systems* **2017**, 1024–1034.

(17) Scarselli, F.; Gori, M.; Tsoi, A. C.; Hagenbuchner, M.; Monfardini, G. The Graph Neural Network Model. *IEEE Transactions on Neural Networks* **2009**, *20*, 61–80.

(18) Henaff, M.; Bruna, J.; LeCun, Y. Deep Convolutional Networks on Graph-Structured Data. *arXiv preprint arXiv:1506.05163* **2015**,

(19) Dai, H.; Dai, B.; Song, L. Discriminative Embeddings of Latent Variable Models for Structured Data. *International Conference on Machine Learning* **2016**, 2702–2711.

(20) Lei, T.; Jin, W.; Barzilay, R.; Jaakkola, T. Deriving Neural Architectures from Sequence and Graph Kernels. *arXiv preprint arXiv:1705.09037* **2017**,

(21) Kusner, M. J.; Paige, B.; Hernández-Lobato, J. M. Grammar Variational Autoencoder. *arXiv preprint arXiv:1703.01925* **2017**,

(22) Gómez-Bombarelli, R.; Wei, J. N.; Duvenaud, D.; Hernández-Lobato, J. M.; Sánchez-Lengeling, B.; Sheberla, D.; Aguilera-Iparraguirre, J.; Hirzel, T. D.; Adams, R. P.; Aspuru-Guzik, A. Automatic Chemical Design Using a Data-Driven Continuous Representation of Molecules. *ACS Cent. Sci.* **2018**, *4*, 268–276.

(23) Jin, W.; Barzilay, R.; Jaakkola, T. Junction Tree Variational Autoencoder for Molecular Graph Generation. *arXiv preprint arXiv:1802.04364* **2018**,

(24) Jin, W.; Yang, K.; Barzilay, R.; Jaakkola, T. Learning Multimodal Graph-to-Graph Translation for Molecular Optimization. *arXiv preprint arXiv:1812.01070* **2018**,

(25) Cortes, C.; Vapnik, V. Support Vector Machine. *Machine Learning* **1995**, *20*, 273–297.

(26) Breiman, L. Random Forests. *Machine Learning* **2001**, *45*, 5–32.

(27) Mauri, A.; Consonni, V.; Pavan, M.; Todeschini, R. Dragon Software: An Easy Approach to Molecular Descriptor Calculations. *Match* **2006**, *56*, 237–248.

(28) Rogers, D.; Hahn, M. Extended-Connectivity Fingerprints. *J. Chem. Inf. Model.* **2010**, *50*, 742–754.

(29) Swamidass, S. J.; Chen, J.; Bruand, J.; Phung, P.; Ralaivola, L.; Baldi, P. Kernels for Small Molecules and the Prediction of Mutagenicity, Toxicity and Anti-Cancer Activity. *Bioinformatics* **2005**, *21*, i359–i368.

(30) Cao, D.-S.; Xu, Q.-S.; Hu, Q.-N.; Liang, Y.-Z. ChemoPy: Freely Available Python Package for Computational Biology and Chemoinformatics. *Bioinformatics* **2013**, *29*, 1092–1094.

(31) Durant, J. L.; Leland, B. A.; Henry, D. R.; Nourse, J. G. Reoptimization of MDL Keys for Use in Drug Discovery. *J. Chem. Inf. Model.* **2002**, *42*, 1273–1280.

(32) Moriwaki, H.; Tian, Y.-S.; Kawashita, N.; Takagi, T. Mordred: A Molecular Descriptor Calculator. *J. Cheminf.* **2018**, *10*, 4.

(33) Schütt, K.; Kindermans, P.-J.; Felix, H. E. S.; Chmiela, S.; Tkatchenko, A.; Müller, K.-R. SchNet: A Continuous-Filter Convolutional Neural Network for Modeling Quantum Interactions. *Advances in Neural Information Processing Systems* **2017**, 991–1001.

(34) Kondor, R.; Son, H. T.; Pan, H.; Anderson, B.; Trivedi, S. Covariant Compositional Networks for Learning Graphs. *arXiv preprint arXiv:1801.02144* **2018**,

(35) Faber, F. A.; Hutchison, L.; Huang, B.; Gilmer, J.; Schoenholz, S. S.; Dahl, G. E.; Vinyals, O.; Kearnes, S.; Riley, P. F.; von Lilienfeld, O. A. Machine Learning Prediction Errors Better than DFT Accuracy. *arXiv preprint arXiv:1702.05532* **2017**,

(36) Feinberg, E. N.; Sur, D.; Wu, Z.; Husic, B. E.; Mai, H.; Li, Y.; Sun, S.; Yang, J.; Ramsundar, B.; Pande, V. S. PotentialNet for Molecular Property Prediction. *ACS Cent. Sci.* **2018**, *4*, 1520–1530.

(37) Lee, A. A.; Yang, Q.; Bassyouni, A.; Butler, C. R.; Hou, X.; Jenkinson, S.; Price, D. A. Ligand Biological Activity Predicted by Cleaning Positive and Negative Chemical Correlations. *Proc. Natl. Acad. Sci. U. S. A.* **2019**,

(38) Weininger, D. SMILES, A Chemical Language and Information System. 1. Introduction to Methodology and Encoding Rules. *J. Chem. Inf. Model.* **1988**, *28*, 31–36.

(39) Ishiguro, K.; Maeda, S.-i.; Koyama, M. Graph Warp Module: An Auxiliary Module for Boosting the Power of Graph Neural Networks. *arXiv preprint arXiv:1902.01020* **2019**,

(40) Liu, K.; Sun, X.; Jia, L.; Ma, J.; Xing, H.; Wu, J.; Gao, H.; Sun, Y.; Boulnois, F.; Fan, J. Chemi-net: A Graph Convolutional Network for Accurate Drug Property Prediction. *arXiv preprint arXiv:1803.06236* **2018**,

(41) Mahé, P.; Ueda, N.; Akutsu, T.; Perret, J.-L.; Vert, J.-P. Extensions of Marginalized Graph Kernels. *Proceedings of the Twenty-First International Conference on Machine learning* **2004**, 70.

(42) Koller, D.; Friedman, N.; Bach, F. Probabilistic Graphical Models: Principles and Techniques. *MIT Press* **2009**,

(43) Nair, V.; Hinton, G. E. Rectified Linear Units Improve Restricted Boltzmann Machines. *Proceedings of the 27th International Conference on Machine Learning* **2010**,

(44) Landrum, G. RDKit: Open-Source Cheminformatics. **2006**, <https://rdkit.org/docs/index.html>, last visited 2019-05-24.

(45) Pedregosa, F.; Varoquaux, G.; Gramfort, A.; Michel, V.; Thirion, B.; Grisel, O.; Blondel, M.; Prettenhofer, P.; Weiss, R.; Dubourg, V. Scikit-learn: Machine Learning in Python. *Journal of Machine Learning Research* **2011**, *12*, 2825–2830.

(46) Irwin, J. J.; Shoichet, B. K. ZINC—A Free Database of Commercially Available Compounds for Virtual Screening. *J. Chem. Inf. Model.* **2005**, *45*, 177–182.

(47) Kim, S.; Thiessen, P. A.; Bolton, E. E.; Chen, J.; Fu, G.; Gindulyte, A.; Han, L.; He, J.; He, S.; Shoemaker, B. A. PubChem Substance and Compound Databases. *Nucleic Acids Res.* **2015**, *44*, D1202–D1213.

(48) Sartor, M. A.; Leikauf, G. D.; Medvedovic, M. LRpath: A Logistic Regression Approach for Identifying Enriched Biological Groups in Gene Expression Data. *Bioinformatics* **2008**, *25*, 211–217.

(49) Distributed Asynchronous Hyperparameter Optimization in Python. <https://github.com/hyperopt/hyperopt>, last visited 2019-05-24.

(50) Paszke, A.; Gross, S.; Chintala, S.; Chanan, G.; Yang, E.; DeVito, Z.; Lin, Z.; Desmaison, A.; Antiga, L.; Lerer, A. Automatic differentiation in PyTorch. *31st Conference on Neural Information Processing Systems* **2017**,

(51) Message Passing Neural Networks for Molecule Property Prediction. <https://github.com/swansonk14/chemprop>, last visited 2019-05-24.

(52) Descriptor computation(chemistry) and (optional) storage for machine learning. <https://github.com/bp-kelley/descriptastorus>, last visited 2019-05-24.

(53) Chempool Machine Learning for Molecular Property Prediction. <http://chemprop.csail.mit.edu>, last visited 2019-05-24.

(54) Friedman, J. H. Greedy Function Approximation: A Gradient Boosting Machine. *Annals of Statistics* **2001**, 1189–1232.

(55) Cramer, J. S. Logit Models from Economics and Other Fields. **2003**,

(56) Lusci, A.; Pollastri, G.; Baldi, P. Deep Architectures and Deep Learning in Chemoinformatics: The Prediction of Aqueous Solubility for Drug-like Molecules. *J. Chem. Inf. Model.* **2013**, 53, 1563–1575.

(57) Cortes, C.; Vapnik, V. Support-Vector Networks. *Machine Learning* **1995**, 273–297.

(58) Ma, J.; Sheridan, R. P.; Liaw, A.; Dahl, G. E.; Svetnik, V. Deep Neural Nets as a Method for Quantitative Structure–Activity Relationships. *J. Chem. Inf. Model.* **2015**, 55, 263–274.

(59) Ramsundar, B.; Liu, B.; Wu, Z.; Verras, A.; Tudor, M.; Sheridan, R. P.; Pande, V. Is Multitask Deep Learning Practical for Pharma? *J. Chem. Inf. Model.* **2017**, 57, 2068–2076.

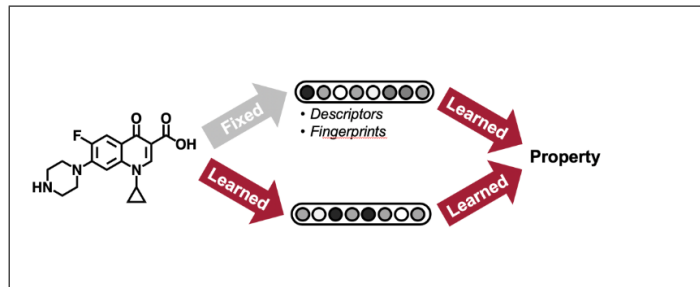
(60) Swamidass, S. J.; Azencott, C.-A.; Lin, T.-W.; Gramajo, H.; Tsai, S.-C.; Baldi, P. Influence Relevance Voting: An Accurate and Interpretable Virtual High Throughput Screening Method. *J. Chem. Inf. Model.* **2009**, 49, 756–766.

(61) Smith, J. S.; Isayev, O.; Roitberg, A. E. ANI-1: An Extensible Neural Network Potential with DFT Accuracy at Force Field Computational Cost. *Chem. Sci.* **2017**, 8, 3192–3203.

(62) Ramsundar, B.; Eastman, P.; Leswing, K.; Walters, P.; Pande, V. Deep Learning for the Life Sciences. *O'Reilly Media* **2019**,

- (63) Scripts for running lsc model on other datasets. https://github.com/yangkevin2/lsc_experiments, last visited 2019-05-24.
- (64) Navarin, N.; Tran, D. V.; Sperduti, A. Pre-training Graph Neural Networks with Kernels. *arXiv preprint arXiv:1811.06930* **2018**,
- (65) Goh, G. B.; Siegel, C.; Vishnu, A.; Hodas, N. Using Rule-Based Labels for Weak Supervised Learning: A ChemNet for Transferable Chemical Property Prediction. *Proceedings of the 24th ACM SIGKDD International Conference on Knowledge Discovery & Data Mining* **2018**, 302–310.

Graphical TOC Entry



Supporting information for: Are Learned Molecular Representations Ready For Prime Time?

Kevin Yang,^{*,†} Kyle Swanson,^{*,†} Wengong Jin,[†] Connor Coley,[‡] Philipp Eiden,[¶]
Hua Gao,[§] Angel Guzman-Perez,[§] Timothy Hopper,[§] Brian Kelley,^{||} Miriam
Mathea,[¶] Andrew Palmer,[¶] Volker Settels,[¶] Tommi Jaakkola,[†] Klavs Jensen,[‡]
and Regina Barzilay[†]

[†]*Computer Science and Artificial Intelligence Laboratory, MIT, Cambridge, MA*

[‡]*Department of Chemical Engineering, MIT, Cambridge, MA*

[¶]*BASF SE, Ludwigshafen, Germany*

[§]*Amgen Inc., Cambridge, MA*

^{||}*Novartis Institutes for BioMedical Research, Cambridge, MA*

E-mail: yangk@mit.edu; swansonk@mit.edu

Code

Our code is publicly available at <https://github.com/swansonk14/chemprop>, which also includes a web interface that supports non-programmatic training and predicting with our model. Code for computing the RDKit features is available at <https://github.com/bp-kelley/descriptastorus>. A public web demonstration of our model's prediction capability on public datasets is available at <http://chemprop.csail.mit.edu> (see Figure S1 for a screenshot of the demonstration).

In addition, we ran the baseline from Mayr et al.^{S1} using the code at https://github.com/yangkevin2/lsc_experiments.

Chemprop Home Train Predict Data Checkpoints

Kyle Swanson · Create User

Predict

Model checkpoint

model

Text Input Upload File Draw Molecule

Draw a molecule

Draw a molecule

C N O S F Cl Br P X

c1ccccc1

Predict

Download Predictions

SMILES: c1ccccc1

property: -2.155125540697954

Chemprop v0.1 © 2019

Source code

Figure S1: Screenshot of the prediction page of our web interface.

Additional Dataset Statistics

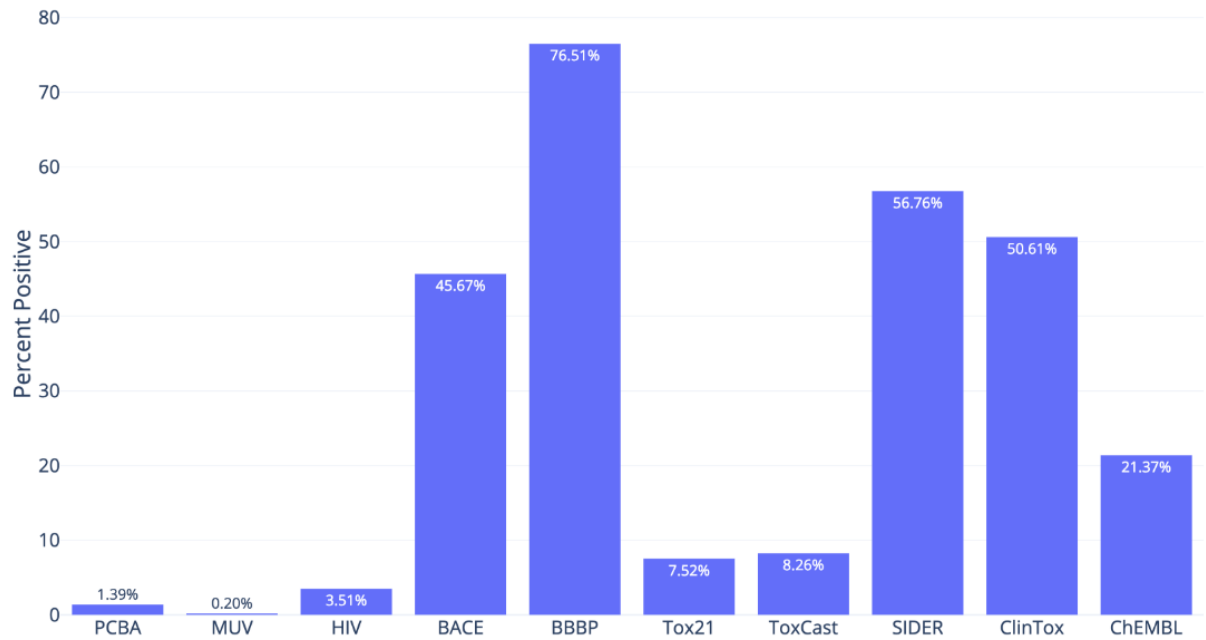


Figure S2: Class balance on the publicly available classification datasets. The Y-axis is the average percent of positives in the tasks in a dataset, weighted by the number of molecules with known values for each task.

In addition to the class balance statistics in Figure S2, we also analyze the class imbalances introduced in both random and scaffold splits, quantifying the imbalance using the following metric. Let r be the fraction of the less common class (0 or 1) in the full dataset, and let r_t be the same fraction for a particular test fold for one of our splits. Then we measure imbalance for a particular property and test fold by $\max\left(\frac{r}{r_t}, \frac{r_t}{r}\right)$ (that is, the ratio of the larger over the smaller) and average across all properties and test folds for each dataset. Thus, a higher metric indicates greater class imbalance introduced by data splitting. On rare occasions for both the random and scaffold split, r_t is 0 due to the sparsity and imbalance of some properties in datasets that contain a large number of properties. We omit these cases from the average, and for each dataset we denote the number of property-test fold pairs for which this occurred. (Such properties are omitted when calculating the average AUC for that particular test fold.) Overall, as indicated in Figure S3 and Tables S1 and S2, the scaffold

split is more imbalanced than the random split, but the numbers are comparable. On no dataset does the scaffold split test set's class balance differ (on average) from the full dataset's class balance by more than a factor of 2.

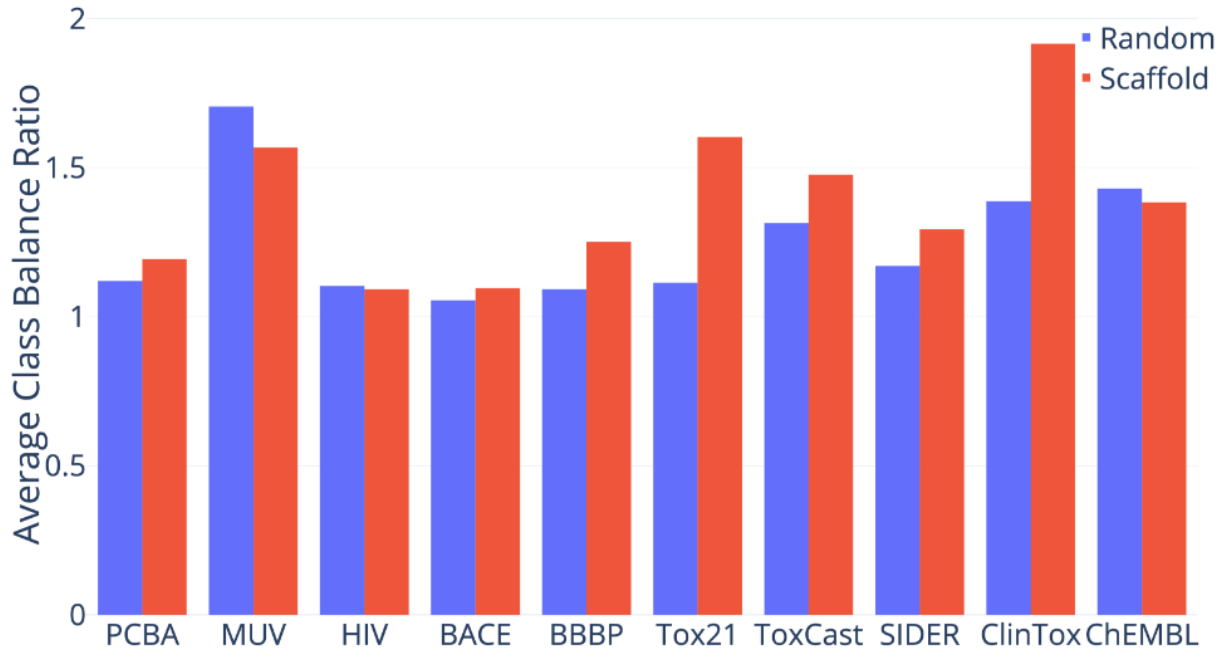


Figure S3: Ratio of class balance between the full dataset and the test set on the publicly available classification datasets (see text for definition of the ratio).

Table S1: Class Balance Ratio (Random Split).

Dataset	Class Balance Ratio	# Failed Property-Fold Pairs	# Property-Fold Pairs
PCBA	1.1197	0	384
MUV	1.705	2	51
HIV	1.1034	0	3
BACE	1.0551	0	10
BBBP	1.0923	0	10
Tox21	1.1136	0	120
ToxCast	1.3137	103	6170
SIDER	1.1704	2	270
ClinTox	1.3871	0	20
ChEMBL	1.4297	236	3930

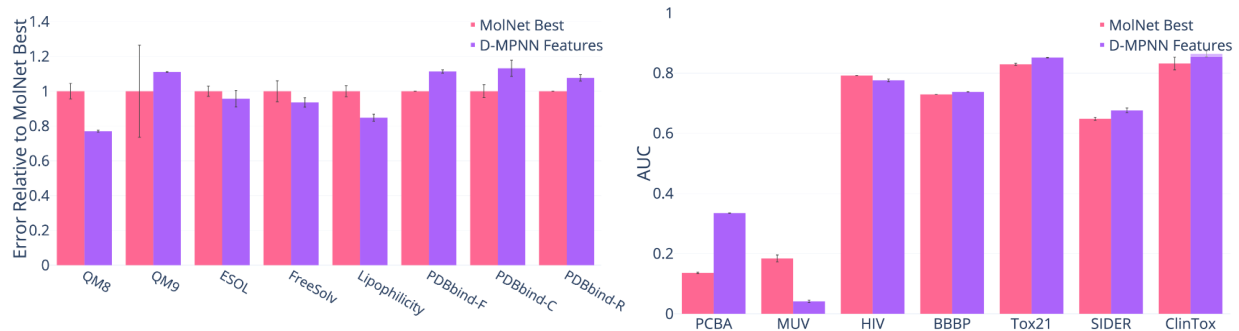
Table S2: Class Balance Ratio (Scaffold Split).

Dataset	Class Balance Ratio	# Failed Property-Fold Pairs	# Property-Fold Pairs
PCBA	1.1928	0	384
MUV	1.5674	3	51
HIV	1.0922	0	3
BACE	1.0956	0	10
BBBP	1.2513	0	10
Tox21	1.6025	0	120
ToxCast	1.4764	180	6170
SIDER	1.2937	1	270
ClinTox	1.9153	0	20
ChEMBL	1.3833	322	3930

Comparison to Baselines

Comparison to MoleculeNet

Comparison between our D-MPNN with RDKit features and the best model from MoleculeNet using the splits from MoleculeNet.^{S2} We were unable to reproduce the splits from MoleculeNet on QM7, BACE, and ToxCast, so we leave out those datasets. The QM8, QM9, and PDBbind datasets include 3D coordinates that our model does not use but some MoleculeNet models may use.



(a) Regression Datasets (lower = better).

(b) Classification Datasets (higher = better).

Figure S4: Comparison to MoleculeNet models on Wu et al.'s^{S2} original splits.

Table S3: Comparison to MoleculeNet models on Wu et al.’s^{S2} original splits.

Dataset	Metric	Split Type	MolNet ^{S2} Best	D-MPNN Features
QM8	MAE	Random	0.014 \pm 0.001	0.011 \pm 0.000 (-23.03% p=0.04)
QM9	MAE	Random	2.400 \pm 1.100	2.666 \pm 0.006 (+11.07% p=0.72)
ESOL	RMSE	Random	0.580 \pm 0.030	0.555 \pm 0.047 (-4.33% p=0.52)
FreeSolv	RMSE	Random	1.150 \pm 0.120	1.075 \pm 0.054 (-6.48% p=0.43)
Lipophilicity	RMSE	Random	0.655 \pm 0.036	0.555 \pm 0.023 (-15.26% p=0.06)
PCBA	PRC-AUC	Random	0.136 \pm 0.004	0.335 \pm 0.001 (+146.05% p=0.00)
MUV	PRC-AUC	Random	0.184 \pm 0.020	0.041 \pm 0.007 (-77.66% p=0.01)
HIV	ROC-AUC	Scaffold	0.792 \pm 0.000	0.776 \pm 0.008 (-2.05% p=0.06)
BBBP	ROC-AUC	Scaffold	0.729 \pm 0.000	0.738 \pm 0.001 (+1.17% p=0.00)
Tox21	ROC-AUC	Random	0.829 \pm 0.006	0.851 \pm 0.002 (+2.69% p=0.03)
SIDER	ROC-AUC	Random	0.648 \pm 0.009	0.676 \pm 0.014 (+4.32% p=0.10)
ClinTox	ROC-AUC	Random	0.832 \pm 0.037	0.864 \pm 0.017 (+3.83% p=0.31)

Comparison to Mayr et al.^{S1}

Comparison between our best single model (i.e. optimized hyperparameters and optionally RDKit features but without ensembling) and the feed-forward network (FFN) architecture of Mayr et al.^{S1} using their best descriptor set. We ran this comparison only on scaffold split due to computational cost; as the model of Mayr et al.^{S1} uses hyperparameter optimization spanning 40 different parameter settings for 300 epochs each, their hyperparameter optimization is actually more expensive than that of our D-MPNN.

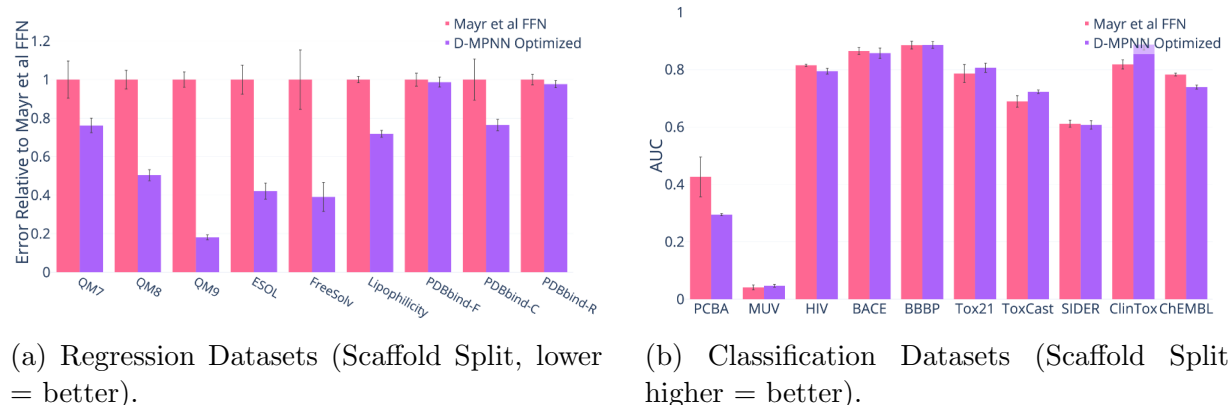


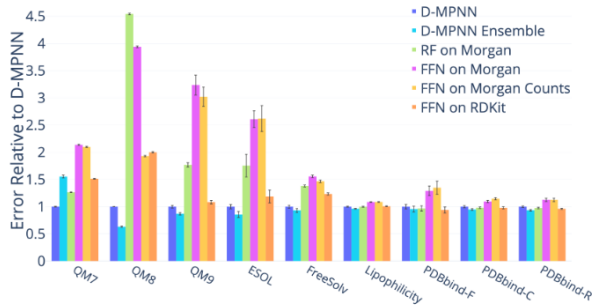
Figure S5: Comparison to Mayr et al..^{S1}

Table S4: Comparison to Mayr et al.^{S1} (Scaffold Split).

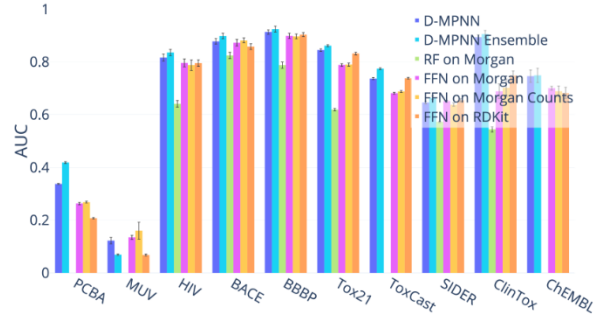
Dataset	Metric	Mayr et al. ^{S1} FFN	D-MPNN Optimized
QM7	MAE	119.220 \pm 36.490	90.869 \pm 14.199 (-23.78% p=0.05)
QM8	MAE	0.024 \pm 0.004	0.012 \pm 0.002 (-49.62% p=0.00)
QM9	MAE	13.117 \pm 0.907	2.370 \pm 0.294 (-81.93% p=0.00)
ESOL	RMSE	2.344 \pm 0.561	0.987 \pm 0.314 (-57.89% p=0.00)
FreeSolv	RMSE	4.513 \pm 2.196	1.763 \pm 1.075 (-60.93% p=0.01)
Lipophilicity	RMSE	0.856 \pm 0.044	0.615 \pm 0.048 (-28.17% p=0.00)
PDBbind-F	RMSE	1.415 \pm 0.148	1.397 \pm 0.117 (-1.28% p=0.77)
PDBbind-C	RMSE	2.507 \pm 0.845	1.916 \pm 0.236 (-23.59% p=0.06)
PDBbind-R	RMSE	1.514 \pm 0.135	1.479 \pm 0.087 (-2.34% p=0.50)
PCBA	PRC-AUC	0.426 \pm 0.120	0.295 \pm 0.006 (-30.87% p=0.20)
MUV	PRC-AUC	0.041 \pm 0.015	0.047 \pm 0.009 (+13.48% p=0.63)
HIV	ROC-AUC	0.815 \pm 0.006	0.794 \pm 0.017 (-2.53% p=0.19)
BACE	ROC-AUC	0.865 \pm 0.037	0.857 \pm 0.057 (-0.89% p=0.73)
BBBP	ROC-AUC	0.885 \pm 0.043	0.886 \pm 0.036 (+0.10% p=0.96)
Tox21	ROC-AUC	0.786 \pm 0.099	0.806 \pm 0.050 (+2.55% p=0.58)
ToxCast	ROC-AUC	0.689 \pm 0.063	0.723 \pm 0.020 (+4.86% p=0.14)
SIDER	ROC-AUC	0.611 \pm 0.038	0.607 \pm 0.047 (-0.67% p=0.83)
ClinTox	ROC-AUC	0.818 \pm 0.050	0.887 \pm 0.058 (+8.44% p=0.02)
ChEMBL	ROC-AUC	0.783 \pm 0.008	0.739 \pm 0.012 (-5.56% p=0.04)

Comparison to Other Baselines

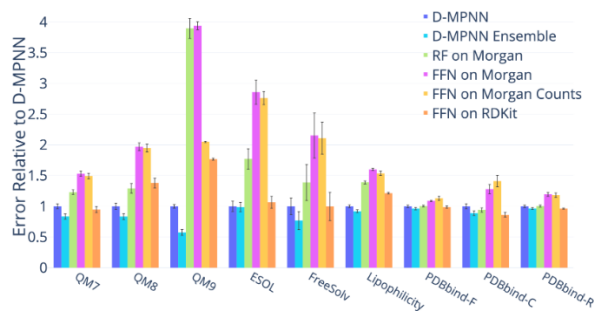
Comparison to several baselines using feed-forward neural networks on molecular fingerprints or descriptors.



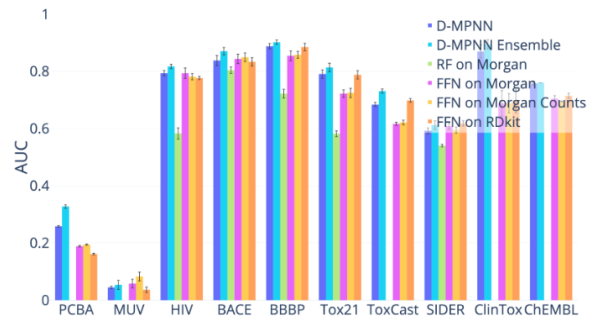
(a) Regression Datasets (Random Split, lower = better).



(b) Classification Datasets (Random Split, higher = better).



(c) Regression Datasets (Scaffold Split, lower = better).



(d) Classification Datasets (Scaffold Split, higher = better).

Figure S6: Comparison to Baselines.

Table S5: Comparison to Baselines, Part I (Random Split).

Dataset	Metric	D-MPNN	D-MPNN Ensemble
QM7	MAE	66.475 \pm 2.088	59.379 \pm 2.315 (-10.67% p=0.00)
QM8	MAE	0.011 \pm 0.000	0.017 \pm 0.001 (+55.42% p=0.00)
QM9	MAE	3.101 \pm 0.010	1.959 \pm 0.066 (-36.82% p=0.00)
ESOL	RMSE	0.665 \pm 0.052	0.578 \pm 0.046 (-13.08% p=0.00)
FreeSolv	RMSE	1.167 \pm 0.150	0.998 \pm 0.207 (-14.43% p=0.07)
Lipophilicity	RMSE	0.596 \pm 0.050	0.555 \pm 0.067 (-6.83% p=0.16)
PDBbind-F	RMSE	1.311 \pm 0.034	1.262 \pm 0.031 (-3.75% p=0.01)
PDBbind-C	RMSE	2.151 \pm 0.285	2.057 \pm 0.353 (-4.39% p=0.53)
PDBbind-R	RMSE	1.395 \pm 0.087	1.322 \pm 0.077 (-5.22% p=0.08)
PCBA	PRC-AUC	0.337 \pm 0.004	0.418 \pm 0.006 (+24.03% p=0.00)
MUV	PRC-AUC	0.122 \pm 0.020	0.069 \pm 0.005 (-43.38% p=0.05)
HIV	ROC-AUC	0.816 \pm 0.023	0.836 \pm 0.020 (+2.40% p=0.38)
BACE	ROC-AUC	0.878 \pm 0.032	0.898 \pm 0.034 (+2.31% p=0.20)
BBBP	ROC-AUC	0.913 \pm 0.026	0.925 \pm 0.036 (+1.23% p=0.45)
Tox21	ROC-AUC	0.845 \pm 0.015	0.861 \pm 0.012 (+1.95% p=0.03)
ToxCast	ROC-AUC	0.737 \pm 0.013	0.774 \pm 0.011 (+5.09% p=0.00)
SIDER	ROC-AUC	0.646 \pm 0.016	0.664 \pm 0.021 (+2.79% p=0.06)
ClinTox	ROC-AUC	0.894 \pm 0.027	0.906 \pm 0.043 (+1.33% p=0.47)
ChEMBL	ROC-AUC	0.746 \pm 0.040	0.749 \pm 0.046 (+0.41% p=0.94)

Table S6: Comparison to Baselines, Part II (Random Split).

Dataset	RF on Morgan	FFN on Morgan
QM7	124.667 \pm 3.928 (+87.54% p=0.00)	134.720 \pm 3.724 (+102.66% p=0.00)
QM8	0.014 \pm 0.000 (+26.49% p=0.00)	0.024 \pm 0.000 (+113.72% p=0.00)
QM9	14.089 \pm 0.079 (+354.34% p=0.00)	12.215 \pm 0.076 (+293.92% p=0.00)
ESOL	1.176 \pm 0.086 (+76.86% p=0.00)	2.152 \pm 0.386 (+223.59% p=0.00)
FreeSolv	2.048 \pm 0.769 (+75.50% p=0.01)	3.043 \pm 0.567 (+160.82% p=0.00)
Lipophilicity	0.823 \pm 0.035 (+38.06% p=0.00)	0.928 \pm 0.044 (+55.65% p=0.00)
PDBbind-F	1.309 \pm 0.035 (-0.15% p=0.90)	1.423 \pm 0.023 (+8.54% p=0.00)
PDBbind-C	2.083 \pm 0.324 (-3.20% p=0.63)	2.778 \pm 0.599 (+29.12% p=0.02)
PDBbind-R	1.369 \pm 0.064 (-1.90% p=0.46)	1.528 \pm 0.093 (+9.50% p=0.01)
PCBA	—	0.263 \pm 0.008 (-22.03% p=0.00)
MUV	—	0.135 \pm 0.013 (+10.25% p=0.47)
HIV	0.641 \pm 0.022 (-21.45% p=0.01)	0.796 \pm 0.026 (-2.42% p=0.43)
BACE	0.825 \pm 0.039 (-6.08% p=0.01)	0.873 \pm 0.040 (-0.61% p=0.75)
BBBP	0.788 \pm 0.038 (-13.77% p=0.00)	0.899 \pm 0.033 (-1.61% p=0.30)
Tox21	0.619 \pm 0.015 (-26.75% p=0.00)	0.788 \pm 0.017 (-6.70% p=0.00)
ToxCast	—	0.681 \pm 0.011 (-7.52% p=0.00)
SIDER	0.572 \pm 0.007 (-11.38% p=0.00)	0.652 \pm 0.010 (+0.89% p=0.36)
ClinTox	0.544 \pm 0.031 (-39.13% p=0.00)	0.688 \pm 0.088 (-22.99% p=0.00)
ChEMBL	—	0.700 \pm 0.012 (-6.10% p=0.20)

Table S7: Comparison to Baselines, Part III (Random Split).

Dataset	FFN on Morgan Counts	FFN on RDKit
QM7	123.314 \pm 3.936 (+85.50% p=0.00)	75.857 \pm 2.447 (+14.11% p=0.00)
QM8	0.023 \pm 0.000 (+109.94% p=0.00)	0.017 \pm 0.000 (+51.26% p=0.00)
QM9	5.984 \pm 0.076 (+92.96% p=0.00)	6.201 \pm 0.074 (+99.97% p=0.00)
ESOL	2.009 \pm 0.379 (+202.09% p=0.00)	0.721 \pm 0.068 (+8.37% p=0.07)
FreeSolv	3.057 \pm 0.881 (+161.99% p=0.00)	1.384 \pm 0.440 (+18.66% p=0.17)
Lipophilicity	0.874 \pm 0.043 (+46.58% p=0.00)	0.735 \pm 0.039 (+23.36% p=0.00)
PDBbind-F	1.424 \pm 0.032 (+8.64% p=0.00)	1.321 \pm 0.029 (+0.76% p=0.50)
PDBbind-C	2.901 \pm 0.812 (+34.84% p=0.02)	2.020 \pm 0.376 (-6.10% p=0.40)
PDBbind-R	1.599 \pm 0.093 (+14.62% p=0.00)	1.367 \pm 0.089 (-2.04% p=0.49)
PCBA	0.268 \pm 0.006 (-20.43% p=0.00)	0.207 \pm 0.005 (-38.59% p=0.00)
MUV	0.160 \pm 0.055 (+30.81% p=0.38)	0.068 \pm 0.006 (-44.37% p=0.05)
HIV	0.788 \pm 0.035 (-3.47% p=0.36)	0.796 \pm 0.021 (-2.49% p=0.38)
BACE	0.882 \pm 0.030 (+0.41% p=0.80)	0.858 \pm 0.034 (-2.28% p=0.21)
BBBP	0.897 \pm 0.029 (-1.82% p=0.21)	0.904 \pm 0.024 (-1.07% p=0.41)
Tox21	0.790 \pm 0.020 (-6.54% p=0.00)	0.832 \pm 0.016 (-1.57% p=0.09)
ToxCast	0.688 \pm 0.011 (-6.63% p=0.00)	0.738 \pm 0.010 (+0.20% p=0.79)
SIDER	0.638 \pm 0.020 (-1.21% p=0.36)	0.654 \pm 0.019 (+1.33% p=0.30)
ClinTox	0.702 \pm 0.105 (-21.49% p=0.00)	0.749 \pm 0.055 (-16.26% p=0.00)
ChEMBL	0.689 \pm 0.035 (-7.67% p=0.20)	0.682 \pm 0.037 (-8.52% p=0.18)

Table S8: Comparison to Baselines, Part I (Scaffold Split).

Dataset	Metric	D-MPNN	D-MPNN Ensemble
QM7	MAE	105.775 ± 13.202	88.201 ± 13.899 (-16.61% p=0.02)
QM8	MAE	0.0143 ± 0.0023	0.012 ± 0.002 (-16.69% p=0.04)
QM9	MAE	3.451 ± 0.174	1.983 ± 0.289 (-42.53% p=0.02)
ESOL	RMSE	0.980 ± 0.258	0.968 ± 0.237 (-1.21% p=0.92)
FreeSolv	RMSE	2.177 ± 0.914	1.670 ± 1.008 (-23.27% p=0.27)
Lipophilicity	RMSE	0.653 ± 0.046	0.600 ± 0.049 (-8.04% p=0.04)
PDBbind-F	RMSE	1.419 ± 0.089	1.365 ± 0.092 (-3.79% p=0.22)
PDBbind-C	RMSE	2.138 ± 0.278	1.900 ± 0.262 (-11.12% p=0.08)
PDBbind-R	RMSE	1.507 ± 0.095	1.453 ± 0.080 (-3.60% p=0.20)
PCBA	PRC-AUC	0.258 ± 0.005	0.328 ± 0.011 (+26.88% p=0.01)
MUV	PRC-AUC	0.0447 ± 0.0074	0.053 ± 0.027 (+19.59% p=0.64)
HIV	ROC-AUC	0.794 ± 0.016	0.817 ± 0.013 (+2.94% p=0.19)
BACE	ROC-AUC	0.838 ± 0.056	0.871 ± 0.041 (+3.89% p=0.17)
BBBP	ROC-AUC	0.888 ± 0.029	0.902 ± 0.024 (+1.56% p=0.28)
Tox21	ROC-AUC	0.791 ± 0.047	0.814 ± 0.047 (+2.89% p=0.30)
ToxCast	ROC-AUC	0.684 ± 0.023	0.731 ± 0.023 (+6.89% p=0.00)
SIDER	ROC-AUC	0.593 ± 0.032	0.612 ± 0.047 (+3.31% p=0.30)
ClinTox	ROC-AUC	0.870 ± 0.072	0.895 ± 0.050 (+2.86% p=0.39)
ChEMBL	ROC-AUC	0.758 ± 0.008	0.761 ± 0.000 (+0.39% p=0.60)

Table S9: Comparison to Baselines, Part II (Scaffold Split).

Dataset	RF on Morgan	FFN on Morgan
QM7	130.146 \pm 12.179 (+23.04% p=0.00)	161.956 \pm 12.556 (+53.11% p=0.00)
QM8	0.019 \pm 0.004 (+29.25% p=0.01)	0.028 \pm 0.003 (+96.90% p=0.00)
QM9	13.441 \pm 0.980 (+289.49% p=0.00)	13.591 \pm 0.386 (+293.86% p=0.00)
ESOL	1.734 \pm 0.512 (+76.99% p=0.00)	2.801 \pm 0.610 (+185.88% p=0.00)
FreeSolv	3.019 \pm 2.021 (+38.72% p=0.26)	4.683 \pm 2.518 (+115.12% p=0.02)
Lipophilicity	0.908 \pm 0.052 (+38.99% p=0.00)	1.045 \pm 0.042 (+60.11% p=0.00)
PDBbind-F	1.425 \pm 0.060 (+0.44% p=0.86)	1.544 \pm 0.054 (+8.85% p=0.00)
PDBbind-C	2.011 \pm 0.240 (-5.93% p=0.30)	2.737 \pm 0.518 (+28.06% p=0.01)
PDBbind-R	1.514 \pm 0.079 (+0.44% p=0.87)	1.802 \pm 0.157 (+19.53% p=0.00)
PCBA	—	0.189 \pm 0.005 (-26.83% p=0.00)
MUV	—	0.058 \pm 0.027 (+29.71% p=0.49)
HIV	0.583 \pm 0.034 (-26.59% p=0.01)	0.794 \pm 0.031 (-0.02% p=1.00)
BACE	0.804 \pm 0.035 (-4.04% p=0.14)	0.843 \pm 0.052 (+0.64% p=0.83)
BBBP	0.722 \pm 0.049 (-18.68% p=0.00)	0.855 \pm 0.054 (-3.76% p=0.12)
Tox21	0.582 \pm 0.031 (-26.42% p=0.00)	0.722 \pm 0.041 (-8.67% p=0.01)
ToxCast	—	0.616 \pm 0.017 (-9.87% p=0.00)
SIDER	0.540 \pm 0.013 (-8.79% p=0.00)	0.608 \pm 0.035 (+2.69% p=0.31)
ClinTox	—	0.688 \pm 0.142 (-20.88% p=0.01)
ChEMBL	—	0.705 \pm 0.018 (-7.03% p=0.04)

Table S10: Comparison to Baselines, Part III (Scaffold Split).

Dataset	FFN on Morgan Counts	FFN on RDKit
QM7	100.180 \pm 16.776 (-5.29% p=0.43)	119.220 \pm 36.490 (+12.71% p=0.30)
QM8	0.020 \pm 0.004 (+37.75% p=0.00)	0.024 \pm 0.004 (+70.30% p=0.00)
QM9	6.099 \pm 0.099 (+76.75% p=0.00)	13.117 \pm 0.907 (+280.12% p=0.00)
ESOL	1.043 \pm 0.304 (+6.48% p=0.63)	2.344 \pm 0.561 (+139.24% p=0.00)
FreeSolv	2.172 \pm 1.593 (-0.21% p=0.99)	4.513 \pm 2.196 (+107.33% p=0.01)
Lipophilicity	0.792 \pm 0.032 (+21.34% p=0.00)	0.856 \pm 0.044 (+31.02% p=0.00)
PDBbind-F	1.402 \pm 0.079 (-1.20% p=0.66)	1.415 \pm 0.148 (-0.25% p=0.95)
PDBbind-C	1.842 \pm 0.252 (-13.80% p=0.03)	2.507 \pm 0.845 (+17.29% p=0.22)
PDBbind-R	1.451 \pm 0.054 (-3.73% p=0.14)	1.514 \pm 0.135 (+0.44% p=0.90)
PCBA	0.161 \pm 0.005 (-37.49% p=0.00)	0.426 \pm 0.120 (+65.06% p=0.14)
MUV	0.036 \pm 0.016 (-18.44% p=0.51)	0.041 \pm 0.015 (-8.03% p=0.75)
HIV	0.777 \pm 0.009 (-2.15% p=0.25)	0.815 \pm 0.006 (+2.67% p=0.17)
BACE	0.833 \pm 0.046 (-0.55% p=0.84)	0.865 \pm 0.037 (+3.22% p=0.24)
BBBP	0.885 \pm 0.040 (-0.32% p=0.86)	0.885 \pm 0.043 (-0.31% p=0.87)
Tox21	0.788 \pm 0.046 (-0.37% p=0.89)	0.786 \pm 0.099 (-0.55% p=0.90)
ToxCast	0.699 \pm 0.020 (+2.12% p=0.17)	0.689 \pm 0.063 (+0.76% p=0.81)
SIDER	0.618 \pm 0.031 (+4.32% p=0.10)	0.611 \pm 0.038 (+3.19% p=0.26)
ClinTox	0.697 \pm 0.131 (-19.91% p=0.01)	0.818 \pm 0.050 (-5.94% p=0.09)
ChEMBL	0.715 \pm 0.015 (-5.70% p=0.05)	0.783 \pm 0.008 (+3.27% p=0.07)

Proprietary Datasets

Amgen

Comparison of our D-MPNN in both its unoptimized and optimized form against baseline models on Amgen internal datasets using a time split of the data. Note that rPPB is in logit while Sol and RLM are in \log_{10} .

Table S11: Comparison to Baselines on Amgen, Part I. Note: The metric for hPXR (class) is ROC-AUC; all others are RMSE. *Only one run.

Dataset	D-MPNN	D-MPNN Ensemble	RF on Morgan
rPPB	1.057 \pm 0.026	0.964 \pm 0.007 (-8.78% p=0.00)	1.089 \pm 0.009 (+3.11% p=0.00)
Sol	0.706 \pm 0.013	0.675 \pm 0.001 (-4.42% p=0.05)	0.729 \pm 0.000 (+3.22% p=0.10)
RLM	0.331 \pm 0.004	0.298 \pm 0.003 (-9.72% p=0.01)	0.360* (+8.78%)
hPXR	36.584 \pm 0.751	34.604 \pm 0.568 (-5.41% p=0.07)	41.600 \pm 0.070 (+13.71% p=0.01)
hPXR (class)	0.842 \pm 0.008	0.858 \pm 0.002 (+1.95% p=0.07)	0.598 \pm 0.004 (-28.98% p=0.00)

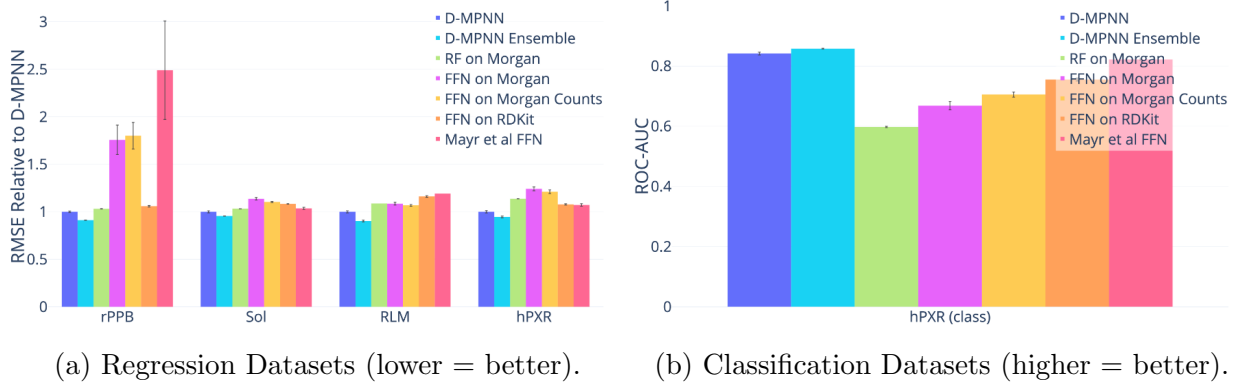


Figure S7: Comparison to Baselines on Amgen.

Table S12: Comparison to Baselines on Amgen, Part II. Note: The metric for hPXR (class) is ROC-AUC; all others are MSE.

Dataset	FFN on Morgan	FFN on Morgan Counts
rPPB	1.856 ± 0.517 (+75.69% p=0.00)	1.903 ± 0.468 (+80.09% p=0.00)
Sol	0.802 ± 0.017 (+13.64% p=0.02)	0.779 ± 0.008 (+10.31% p=0.01)
RLM	0.359 ± 0.005 (+8.48% p=0.01)	0.353 ± 0.003 (+6.81% p=0.01)
hPXR	45.428 ± 1.255 (+24.17% p=0.01)	44.305 ± 1.226 (+21.10% p=0.01)
hPXR (class)	0.669 ± 0.024 (-20.56% p=0.01)	0.705 ± 0.015 (-16.18% p=0.01)

Table S13: Comparison to Baselines on Amgen, Part III. Note: The metric for hPXR (class) is ROC-AUC; all others are MSE.

Dataset	FFN on RDKit	Mayr et al. ^{S1}
rPPB	1.119 ± 0.027 (+5.87% p=0.00)	2.632 ± 1.730 (+149.12% p=0.02)
Sol	0.765 ± 0.003 (+8.30% p=0.02)	0.732 ± 0.013 (+3.62% p=0.14)
RLM	0.384 ± 0.003 (+16.14% p=0.00)	$0.394 \pm$ only run once (+19.20%)
hPXR	39.426 ± 0.465 (+7.77% p=0.03)	39.230 ± 0.836 (+7.23% p=0.06)
hPXR (class)	0.755 ± 0.008 (-10.25% p=0.01)	0.822 ± 0.004 (-2.32% p=0.06)

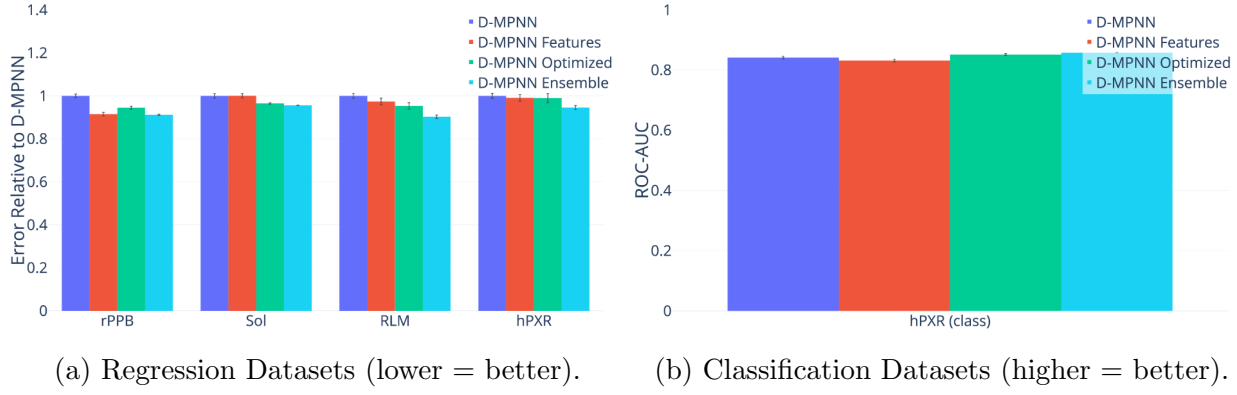


Figure S8: Optimizations on Amgen.

Amgen Model Optimizations

Table S14: Optimizations on Amgen, Part I. Note: The metric for hPXR (class) is ROC-AUC; all others are RMSE.

Dataset	D-MPNN	D-MPNN Features
rPPB	1.057 ± 0.026	0.967 ± 0.028 (-8.50% p=0.00)
Sol	0.706 ± 0.013	0.706 ± 0.013 (+0.04% p=0.98)
RLM	0.331 ± 0.004	0.322 ± 0.005 (-2.64% p=0.14)
hPXR	36.584 ± 0.751	36.252 ± 0.980 (-0.91% p=0.69)
hPXR (class)	0.842 ± 0.008	0.832 ± 0.007 (-1.18% p=0.25)

Table S15: Optimizations on Amgen, Part II. Note: The metric for hPXR (class) is ROC-AUC; all others are RMSE.

Dataset	D-MPNN Optimized	D-MPNN Ensemble
rPPB	0.999 ± 0.024 (-5.48% p=0.00)	0.964 ± 0.007 (-8.78% p=0.00)
Sol	0.681 ± 0.004 (-3.54% p=0.09)	0.675 ± 0.001 (-4.42% p=0.05)
RLM	0.315 ± 0.005 (-4.66% p=0.05)	0.298 ± 0.003 (-9.72% p=0.01)
hPXR	36.206 ± 1.326 (-1.03% p=0.71)	34.604 ± 0.568 (-5.41% p=0.07)
hPXR (class)	0.852 ± 0.006 (+1.20% p=0.22)	0.858 ± 0.002 (+1.95% p=0.07)

BASF

Comparison of our D-MPNN in both its unoptimized and optimized form against baseline models on BASF internal datasets using a scaffold split of the data.

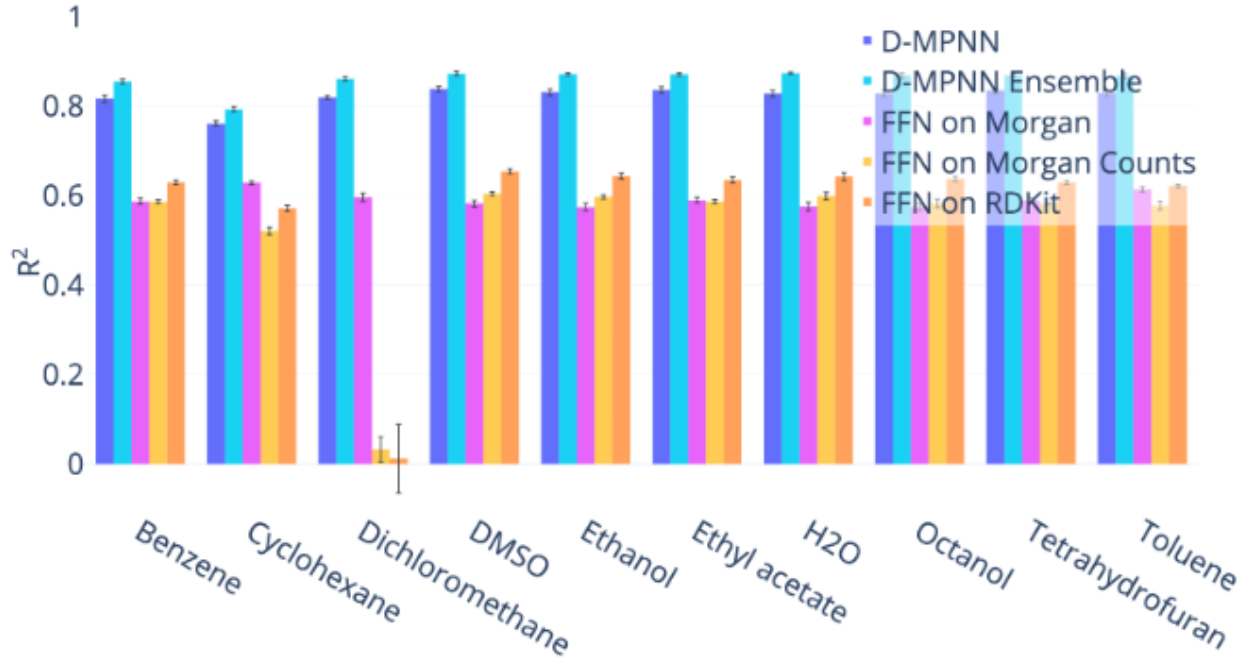


Figure S9: Comparison to Baselines on BASF (higher = better).

Table S16: Comparison to Baselines on BASF, Part I. Note: All numbers are R^2 .

Dataset	D-MPNN	D-MPNN Ensemble	RF on Morgan
Benzene	0.817 ± 0.014	0.855 ± 0.009 (+4.65% p=0.06)	0.587 ± 0.011 (-28.13% p=0.00)
Cyclohexane	0.761 ± 0.010	0.793 ± 0.011 (+4.22% p=0.06)	0.629 ± 0.007 (-17.38% p=0.00)
Dichloromethane	0.820 ± 0.007	0.861 ± 0.008 (+5.06% p=0.02)	0.596 ± 0.016 (-27.23% p=0.00)
DMSO	0.838 ± 0.010	0.873 ± 0.008 (+4.12% p=0.04)	0.582 ± 0.012 (-30.57% p=0.00)
Ethanol	0.831 ± 0.013	0.872 ± 0.005 (+4.85% p=0.04)	0.574 ± 0.015 (-30.90% p=0.00)
Ethyl acetate	0.837 ± 0.012	0.871 ± 0.006 (+4.17% p=0.04)	0.590 ± 0.011 (-29.49% p=0.00)
H2O	0.828 ± 0.012	0.874 ± 0.004 (+5.53% p=0.03)	0.576 ± 0.017 (-30.51% p=0.00)
Octanol	0.829 ± 0.013	0.869 ± 0.010 (+4.82% p=0.05)	0.574 ± 0.014 (-30.68% p=0.00)
Tetrahydrofuran	0.835 ± 0.012	0.869 ± 0.006 (+4.01% p=0.05)	0.589 ± 0.008 (-29.44% p=0.00)
Toluene	0.829 ± 0.011	0.868 ± 0.010 (+4.65% p=0.05)	0.614 ± 0.010 (-25.95% p=0.00)

Table S17: Comparison to Baselines on BASF, Part II. Note: All numbers are R^2 .

Dataset	FFN on Morgan	FFN on Morgan Counts	FFN on RDKit
Benzene	0.587 ± 0.007 (-28.21% p=0.00)	0.630 ± 0.009 (-22.89% p=0.00)	0.742 ± 0.007 (-9.23% p=0.01)
Cyclohexane	0.521 ± 0.014 (-31.53% p=0.00)	0.572 ± 0.012 (-24.86% p=0.00)	0.682 ± 0.007 (-10.32% p=0.01)
Dichloromethane	0.032 ± 0.047 (-96.04% p=0.00)	0.012 ± 0.133 (-98.55% p=0.01)	0.695 ± 0.014 (-15.15% p=0.01)
DMSO	0.604 ± 0.007 (-27.92% p=0.00)	0.654 ± 0.009 (-21.95% p=0.00)	0.755 ± 0.007 (-9.92% p=0.01)
Ethanol	0.597 ± 0.008 (-28.13% p=0.00)	0.644 ± 0.012 (-22.54% p=0.00)	0.755 ± 0.005 (-9.21% p=0.01)
Ethyl acetate	0.587 ± 0.008 (-29.82% p=0.00)	0.635 ± 0.012 (-24.10% p=0.00)	0.748 ± 0.009 (-10.58% p=0.01)
H2O	0.599 ± 0.014 (-27.73% p=0.00)	0.643 ± 0.016 (-22.38% p=0.00)	0.754 ± 0.002 (-8.99% p=0.01)
Octanol	0.583 ± 0.017 (-29.66% p=0.00)	0.638 ± 0.009 (-23.05% p=0.00)	0.749 ± 0.007 (-9.60% p=0.01)
Tetrahydrofuran	0.582 ± 0.002 (-30.38% p=0.00)	0.629 ± 0.007 (-24.65% p=0.00)	0.747 ± 0.013 (-10.55% p=0.01)
Toluene	0.578 ± 0.016 (-30.34% p=0.00)	0.622 ± 0.005 (-25.02% p=0.00)	0.756 ± 0.005 (-8.82% p=0.01)

BASF Model Optimization

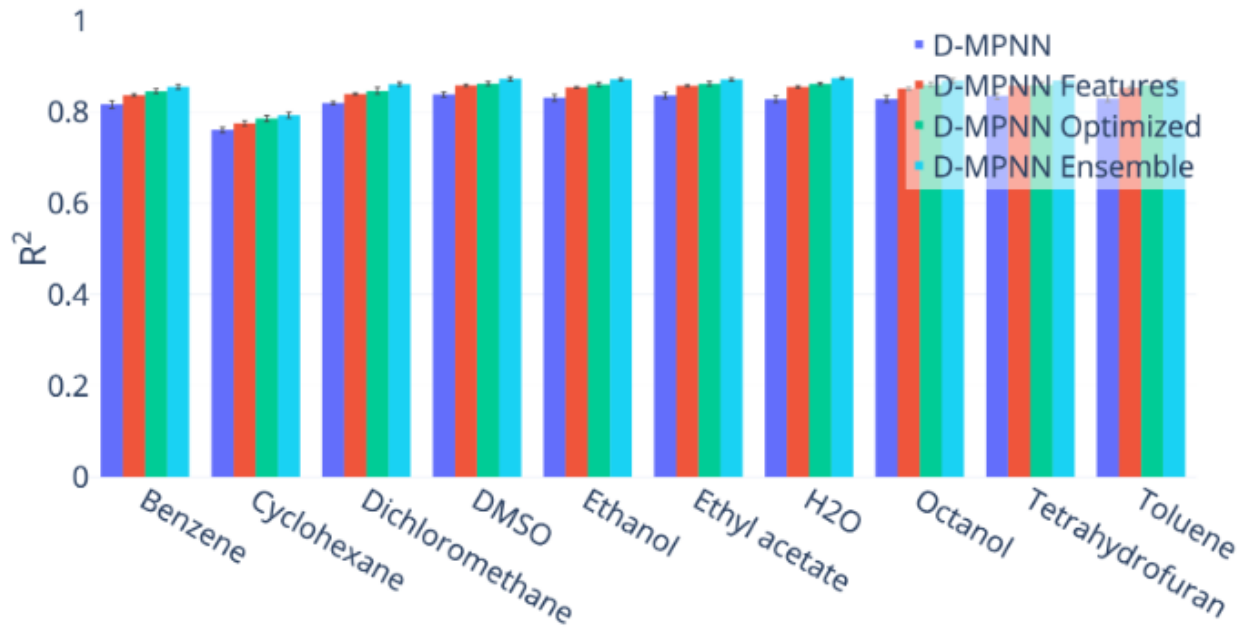


Figure S10: Optimizations on BASF (higher = better).

Table S18: Optimizations on BASF, Part I. Note: All numbers are R^2 .

Dataset	D-MPNN	D-MPNN Features
Benzene	0.817 ± 0.014	0.837 ± 0.005 (+2.43% p=0.15)
Cyclohexane	0.761 ± 0.010	0.775 ± 0.009 (+1.90% p=0.20)
Dichloromethane	0.820 ± 0.007	0.840 ± 0.005 (+2.44% p=0.05)
DMSO	0.838 ± 0.010	0.858 ± 0.005 (+2.38% p=0.09)
Ethanol	0.831 ± 0.013	0.854 ± 0.004 (+2.72% p=0.10)
Ethyl acetate	0.837 ± 0.012	0.858 ± 0.004 (+2.51% p=0.10)
H2O	0.828 ± 0.012	0.855 ± 0.005 (+3.20% p=0.07)
Octanol	0.829 ± 0.013	0.851 ± 0.007 (+2.72% p=0.11)
Tetrahydrofuran	0.835 ± 0.012	0.858 ± 0.005 (+2.71% p=0.09)
Toluene	0.829 ± 0.011	0.853 ± 0.005 (+2.85% p=0.08)

Table S19: Optimizations on BASF, Part II. Note: All numbers are R^2 .

Dataset	D-MPNN Optimized	D-MPNN Ensemble
Benzene	$0.846 \pm 0.008 (+3.54\% \text{ p}=0.09)$	$0.855 \pm 0.009 (+4.65\% \text{ p}=0.06)$
Cyclohexane	$0.786 \pm 0.012 (+3.27\% \text{ p}=0.11)$	$0.793 \pm 0.011 (+4.22\% \text{ p}=0.06)$
Dichloromethane	$0.847 \pm 0.013 (+3.28\% \text{ p}=0.08)$	$0.861 \pm 0.008 (+5.06\% \text{ p}=0.02)$
DMSO	$0.862 \pm 0.007 (+2.86\% \text{ p}=0.08)$	$0.873 \pm 0.008 (+4.12\% \text{ p}=0.04)$
Ethanol	$0.861 \pm 0.008 (+3.53\% \text{ p}=0.08)$	$0.872 \pm 0.005 (+4.85\% \text{ p}=0.04)$
Ethyl acetate	$0.862 \pm 0.008 (+3.06\% \text{ p}=0.09)$	$0.871 \pm 0.006 (+4.17\% \text{ p}=0.04)$
H ₂ O	$0.862 \pm 0.005 (+4.06\% \text{ p}=0.05)$	$0.874 \pm 0.004 (+5.53\% \text{ p}=0.03)$
Octanol	$0.860 \pm 0.009 (+3.81\% \text{ p}=0.07)$	$0.869 \pm 0.010 (+4.82\% \text{ p}=0.05)$
Tetrahydrofuran	$0.860 \pm 0.010 (+2.95\% \text{ p}=0.11)$	$0.869 \pm 0.006 (+4.01\% \text{ p}=0.05)$
Toluene	$0.860 \pm 0.010 (+3.66\% \text{ p}=0.08)$	$0.868 \pm 0.010 (+4.65\% \text{ p}=0.05)$

Novartis

Comparison of our D-MPNN in both its unoptimized and optimized form against baseline models on a Novartis internal dataset using a time split of the data.

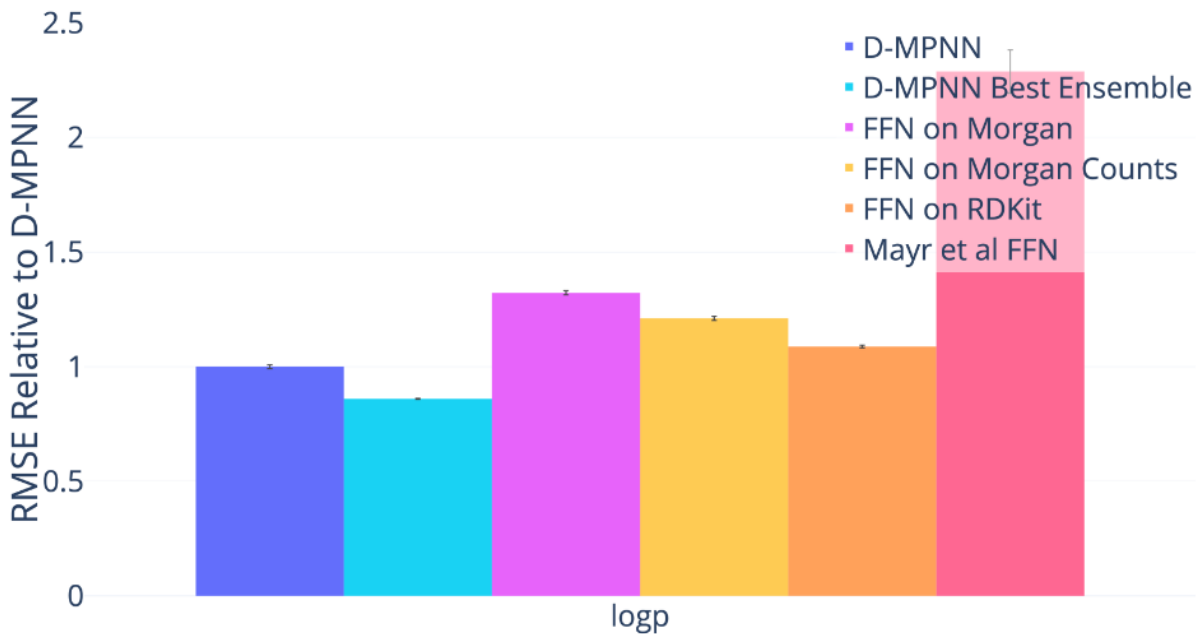


Figure S11: Comparison to Baselines on Novartis (lower = better).

Table S20: Comparison to Baselines on Novartis, Part I. Note: All numbers are RMSE.

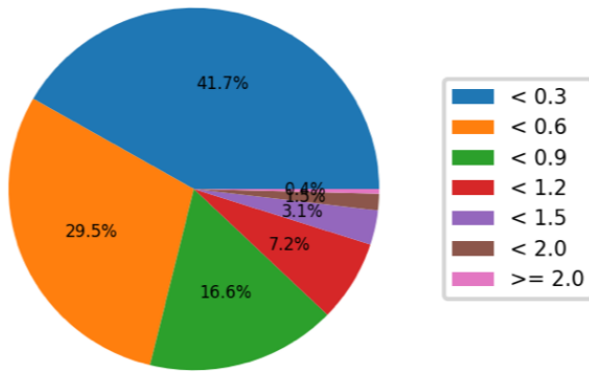
Dataset	D-MPNN	D-MPNN Ensemble	FFN on Morgan
LogP	0.692 ± 0.017	0.595 ± 0.004 (-14.02% p=0.00)	0.915 ± 0.020 (+32.23% p=0.00)

Table S21: Comparison to Baselines on Novartis, Part II. Note: All numbers are RMSE.

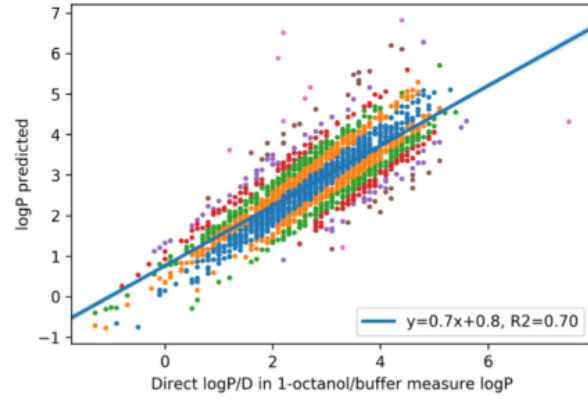
Dataset	FFN on Morgan Counts	FFN on RDKit	Mayr et al. ^{S1}
LogP	0.838 ± 0.019 (+21.10% p=0.00)	0.753 ± 0.013 (+8.82% p=0.00)	1.583 ± 0.207 (+128.76% p=0.00)

Additional Novartis Results

We provide additional results for different versions of our D-MPNN model as well as for a Lasso regression model^{S3} on the Novartis dataset in Figures S12, S13, and S14. These results showcase the importance of proper normalization for the additional RDKit features. Our base D-MPNN predicts a logP within 0.3 of the ground truth on 47.4% of the test set, comparable to the best Lasso baseline. However, augmenting our model with features normalized using a Gaussian distribution assumption (simply subtracting the mean and dividing by the standard deviation for each feature) results in only 43.0% of test set predictions within 0.3 of the ground truth. But using properly normalized CDFs drastically improves this number to 51.2%. Note that the Lasso baseline runs on Morgan fingerprints as well as RDKit features using properly normalized CDFs.

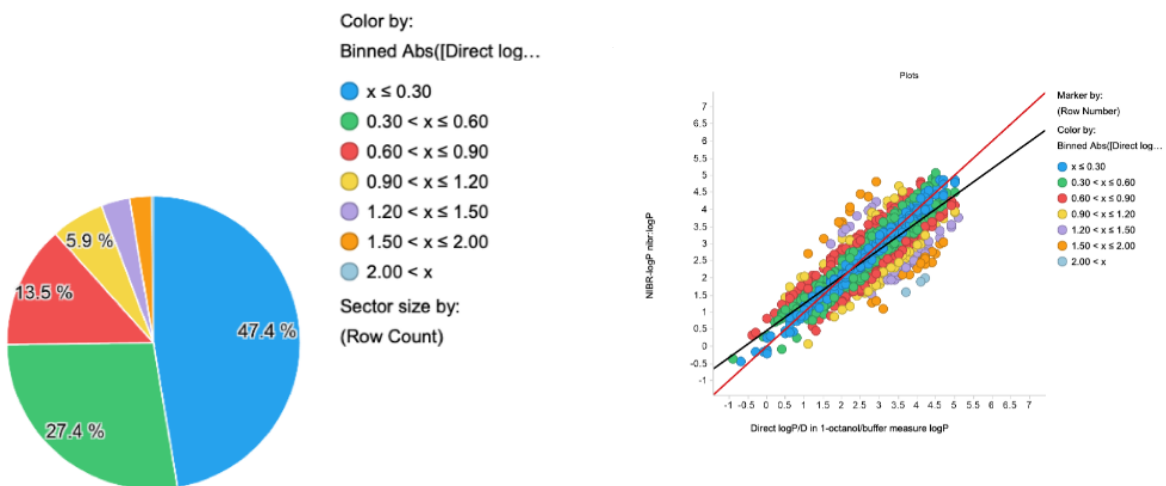


(a) Binned distribution of errors for Lasso baseline.



(b) Scatterplot of Lasso baseline predictions vs. ground truth.

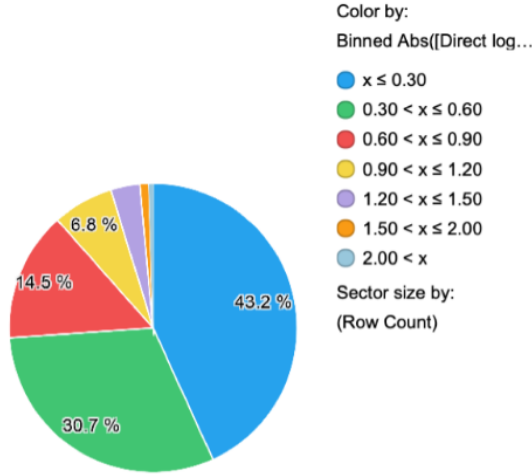
Figure S12: Performance of Lasso models on the proprietary Novartis logP dataset. For each model, a pie chart shows the binned distribution of errors on the test set, and a scatterplot shows the predictions vs. ground truth for individual data points.



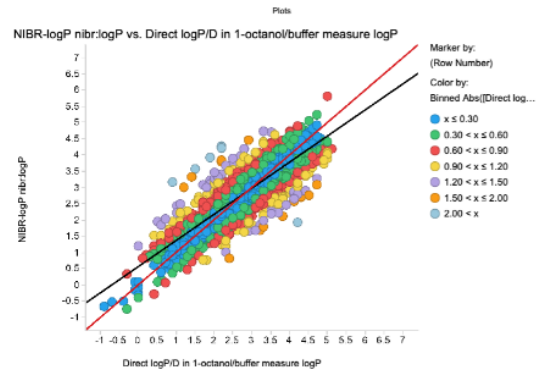
(a) Binned distribution of errors for D-MPNN.

(b) Scatterplot of predictions vs. ground truth for D-MPNN.

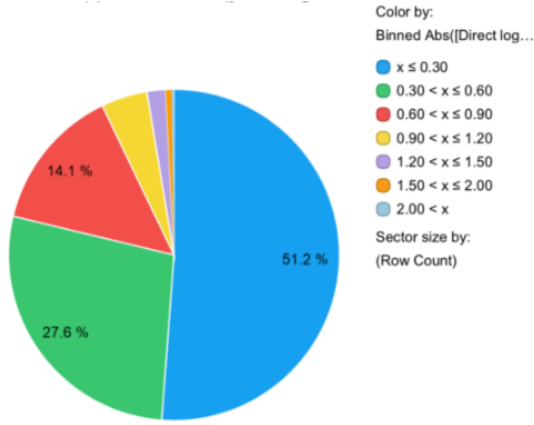
Figure S13: Performance of base D-MPNN model on the proprietary Novartis logP dataset. A pie chart shows the binned distribution of errors on the test set, and a scatterplot shows the predictions vs. ground truth for individual data points.



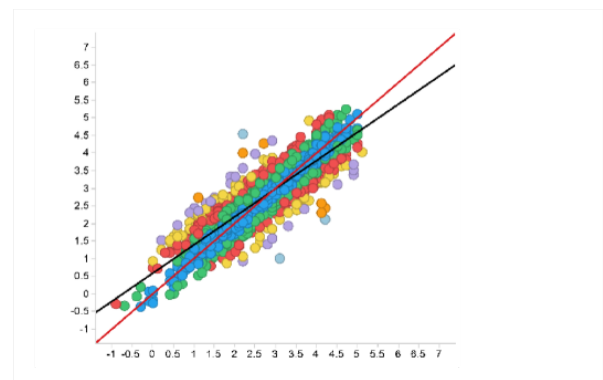
(a) Binned distribution of errors for D-MPNN with features normalized according to a Gaussian distribution assumption.



(b) Scatterplot of predictions vs. ground truth for D-MPNN with features normalized according to a Gaussian distribution assumption.



(c) Binned distribution of errors for D-MPNN with features normalized using CDFs.



(d) Scatterplot of predictions vs. ground truth for D-MPNN with features normalized using CDFs.

Figure S14: Performance of D-MPNN models with features on proprietary Novartis logP dataset. For each model, a pie chart shows the binned distribution of errors on the test set, and a scatterplot shows the predictions vs. ground truth for individual data points.

Sliding Time Window Splits

We additionally evaluated our model on sliding time window splits where chronological data splits were available. For each dataset we divided it chronologically into 14 equally sized chunks. For each contiguous group of 5 chunks, we used the first 3 as training, the fourth as validation, and the fifth as test, for a total of 10 3:1:1 splits. Due to constraints of computational cost, we only evaluated on 3 of the splits for the Amgen datasets RLM, Sol, and hPXR. Overall, the time window split results are very noisy due to the smaller dataset size, so it is hard to make many strong conclusions, but overall the relative ranking of model architectures stays approximately stable compared to the full time splits.

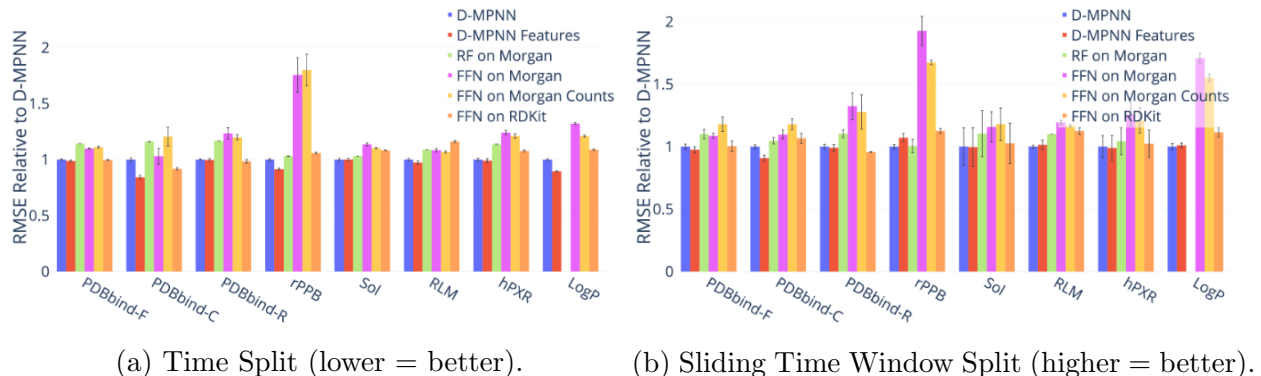


Figure S15: Comparison to Baselines Using Time and Sliding Time Window Splits.

Table S22: Comparison to Baselines Using Time Split, Part I. *Only one run.

Dataset	D-MPNN	D-MPNN Features	RF on Morgan
PDBbind-F	2.187 ± 0.041	2.161 ± 0.055 (-1.20% p=0.26)	2.500 ± 0.002 (+14.31% p=0.00)
PDBbind-C	3.632 ± 0.170	3.058 ± 0.207 (-15.81% p=0.00)	4.218 ± 0.014 (+16.12% p=0.00)
PDBbind-R	2.424 ± 0.046	2.417 ± 0.084 (-0.28% p=0.83)	2.830 ± 0.001 (+16.72% p=0.00)
rPPB	1.057 ± 0.026	0.967 ± 0.028 (-8.50% p=0.00)	1.089 ± 0.009 (+3.11% p=0.00)
Sol	0.706 ± 0.013	0.706 ± 0.013 (+0.04% p=0.98)	0.729 ± 0.000 (+3.22% p=0.10)
RLM	0.331 ± 0.004	0.322 ± 0.005 (-2.64% p=0.14)	0.360^* (+8.78%)
hPXR	36.584 ± 0.751	36.252 ± 0.980 (-0.91% p=0.69)	41.600 ± 0.070 (+13.71% p=0.01)
LogP	0.692 ± 0.017	0.620 ± 0.011 (-10.48% p=0.00)	—

Table S23: Comparison to Baselines Using Time Split, Part II.

Dataset	FFN on Morgan	FFN on Morgan Counts	FFN on RDKit
PDBbind-F	2.403 \pm 0.044 (+9.88% p=0.00)	2.431 \pm 0.055 (+11.16% p=0.00)	2.180 \pm 0.033 (-0.34% p=0.67)
PDBbind-C	3.743 \pm 0.808 (+3.05% p=0.68)	4.380 \pm 0.964 (+20.57% p=0.04)	3.334 \pm 0.114 (-8.21% p=0.00)
PDBbind-R	2.993 \pm 0.380 (+23.45% p=0.00)	2.908 \pm 0.185 (+19.95% p=0.00)	2.387 \pm 0.126 (-1.56% p=0.40)
rPPB	1.856 \pm 0.517 (+75.69% p=0.00)	1.903 \pm 0.468 (+80.09% p=0.00)	1.119 \pm 0.027 (+5.87% p=0.00)
Sol	0.802 \pm 0.017 (+13.64% p=0.02)	0.779 \pm 0.008 (+10.31% p=0.01)	0.765 \pm 0.003 (+8.30% p=0.02)
RLM	0.359 \pm 0.005 (+8.48% p=0.01)	0.353 \pm 0.003 (+6.81% p=0.01)	0.384 \pm 0.003 (+16.14% p=0.00)
hPXR	45.428 \pm 1.255 (+24.17% p=0.01)	44.305 \pm 1.226 (+21.10% p=0.01)	39.426 \pm 0.465 (+7.77% p=0.03)
LogP	0.915 \pm 0.020 (+32.23% p=0.00)	0.838 \pm 0.019 (+21.10% p=0.00)	0.753 \pm 0.013 (+8.82% p=0.00)

Table S24: Comparison to Baselines Using Sliding Time Window Split, Part I. *Only one run.

Dataset	D-MPNN	D-MPNN Features	RF on Morgan
PDBbind-F	1.259 \pm 0.085	1.227 \pm 0.096 (-2.50% p=0.46)	1.385 \pm 0.149 (+9.99% p=0.05)
PDBbind-C	1.548 \pm 0.081	1.405 \pm 0.114 (-9.22% p=0.01)	1.622 \pm 0.125 (+4.77% p=0.15)
PDBbind-R	1.347 \pm 0.086	1.335 \pm 0.118 (-0.89% p=0.80)	1.486 \pm 0.136 (+10.32% p=0.02)
rPPB	1.310 \pm 0.078	1.404 \pm 0.140 (+7.12% p=0.10)	1.318 \pm 0.217 (+0.57% p=0.92)
Sol	0.992 \pm 0.260	0.988 \pm 0.267 (-0.42% p=0.99)	1.095 \pm 0.316 (+10.44% p=0.70)
RLM	0.395 \pm 0.005	0.401 \pm 0.015 (+1.44% p=0.60)	0.434* (+9.97%)
hPXR	47.812 \pm 7.330	47.316 \pm 8.259 (-1.04% p=0.95)	49.868 \pm 9.046 (+4.30% p=0.79)
LogP	0.726 \pm 0.055	0.734 \pm 0.042 (+1.05% p=0.74)	—

Table S25: Comparison to Baselines Using Sliding Time Window Split, Part II.

Dataset	FFN on Morgan	FFN on Morgan Counts	FFN on RDKit
PDBbind-F	1.368 \pm 0.083 (+8.67% p=0.02)	1.485 \pm 0.235 (+17.95% p=0.02)	1.264 \pm 0.169 (+0.41% p=0.93)
PDBbind-C	1.697 \pm 0.175 (+9.63% p=0.04)	1.825 \pm 0.211 (+17.88% p=0.00)	1.651 \pm 0.194 (+6.67% p=0.16)
PDBbind-R	1.783 \pm 0.460 (+32.33% p=0.02)	1.721 \pm 0.584 (+27.80% p=0.08)	1.289 \pm 0.010 (-4.28% p=0.06)
rPPB	2.524 \pm 0.483 (+92.64% p=0.00)	2.194 \pm 0.075 (+67.39% p=0.00)	1.475 \pm 0.084 (+12.57% p=0.00)
Sol	1.148 \pm 0.209 (+15.74% p=0.50)	1.170 \pm 0.223 (+17.96% p=0.46)	1.018 \pm 0.276 (+2.61% p=0.92)
RLM	0.472 \pm 0.007 (+19.44% p=0.00)	0.461 \pm 0.004 (+16.70% p=0.00)	0.444 \pm 0.011 (+12.48% p=0.02)
hPXR	60.244 \pm 8.015 (+26.00% p=0.19)	57.859 \pm 8.343 (+21.02% p=0.26)	48.961 \pm 9.012 (+2.40% p=0.88)
LogP	1.240 \pm 0.091 (+70.80% p=0.00)	1.126 \pm 0.064 (+55.10% p=0.00)	0.810 \pm 0.089 (+11.56% p=0.03)

Experimental Error

Comparison of Amgen’s internal model and our D-MPNN (evaluated on a chronological split) to experimental error. Note that the experimental error is not evaluated on the exact same time split as the two models since it can only be measured on molecules which were tested more than once, but even so the difference in performance is striking.

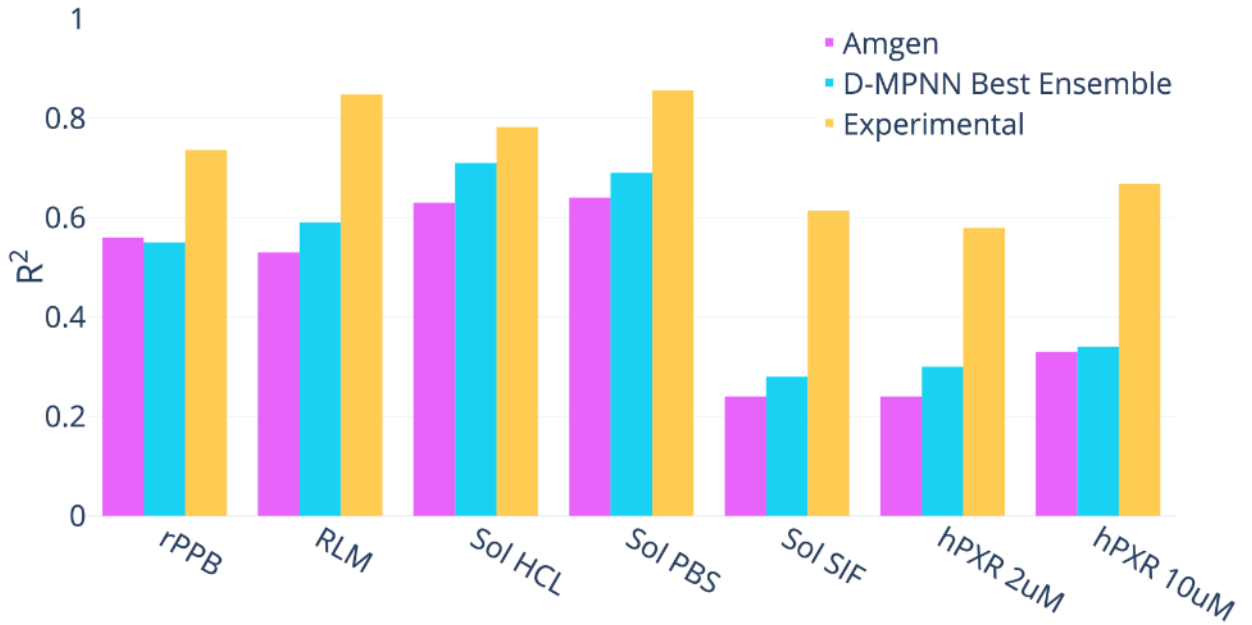


Figure S16: Experimental Error on Amgen (higher = better).

Table S26: Experimental Error on Amgen. Note: All numbers are R^2 .

Dataset	Amgen	D-MPNN Optimized	Experimental
rPPB	0.56	0.55	0.736
RLM	0.53	0.59	0.848
Sol HCL	0.63	0.71	0.782
Sol PBS	0.64	0.69	0.856
Sol SIF	0.24	0.28	0.614
hPXR 2uM	0.24	0.3	0.579
hPXR 10uM	0.33	0.34	0.668

Analysis of Split Type

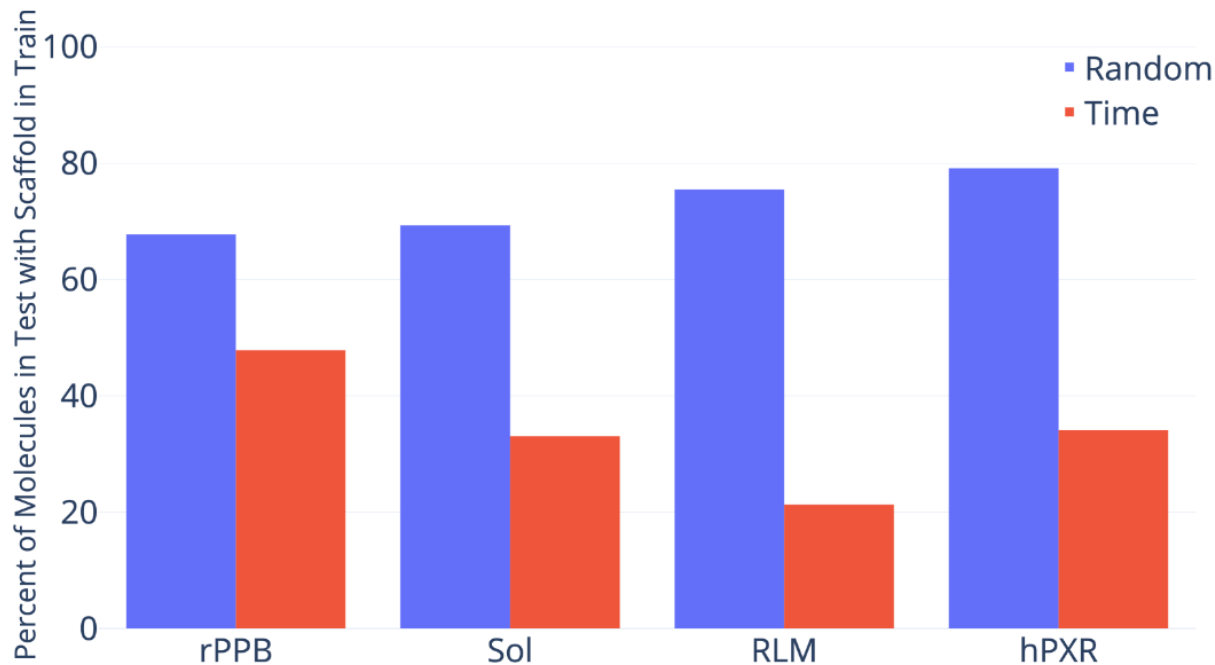


Figure S17: Overlap of molecular scaffolds between the train and test sets for a random or chronological split of four Amgen regression datasets. Overlap is defined as the percent of molecules in the test set which share a scaffold with a molecule in the train set.

Table S27: Overlap of molecular scaffolds between the train and test sets for a random or chronological split of four Amgen regression datasets. Overlap is defined as the percent of molecules in the test set which share a scaffold with a molecule in the train set.

Dataset	Random	Time
rPPB	67.74%	47.84%
Sol	69.31%	33.07%
RLM	75.45%	21.32%
hPXR	79.12%	34.14%

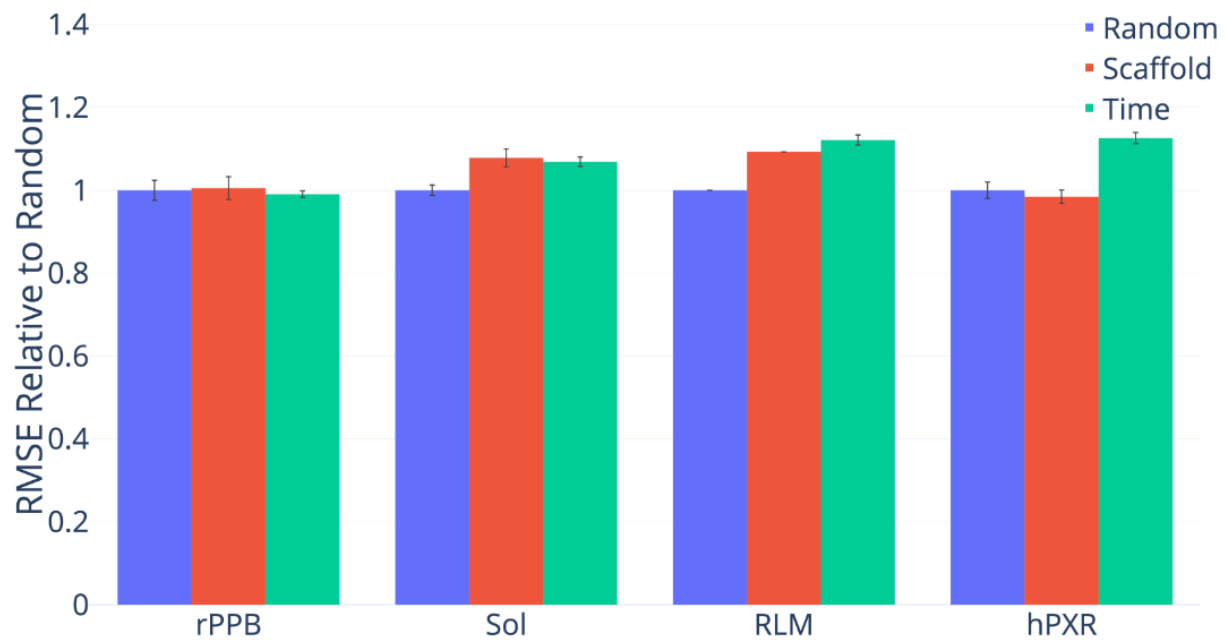


Figure S18: D-MPNN Performance by Split Type on Amgen datasets (lower = better).

Table S28: D-MPNN Performance by Split Type on Amgen datasets. Note: All numbers are RMSE.

Dataset	Random	Scaffold	Time
rPPB	1.067 ± 0.081	$1.072 \pm 0.093 (+0.53\% \text{ p}=0.66)$	$1.057 \pm 0.026 (+0.53\% \text{ p}=0.27)$
Sol	0.661 ± 0.014	$0.712 \pm 0.025 (+7.82\% \text{ p}=0.03)$	$0.706 \pm 0.013 (+7.82\% \text{ p}=0.02)$
RLM	0.295 ± 0.000	$0.322 \pm 0.000 (+9.26\%)$	$0.331 \pm 0.004 (+9.26\%)$
hPXR	32.490 ± 1.124	$31.984 \pm 0.908 (-1.56\% \text{ p}=0.40)$	$36.584 \pm 0.751 (-1.56\% \text{ p}=0.01)$

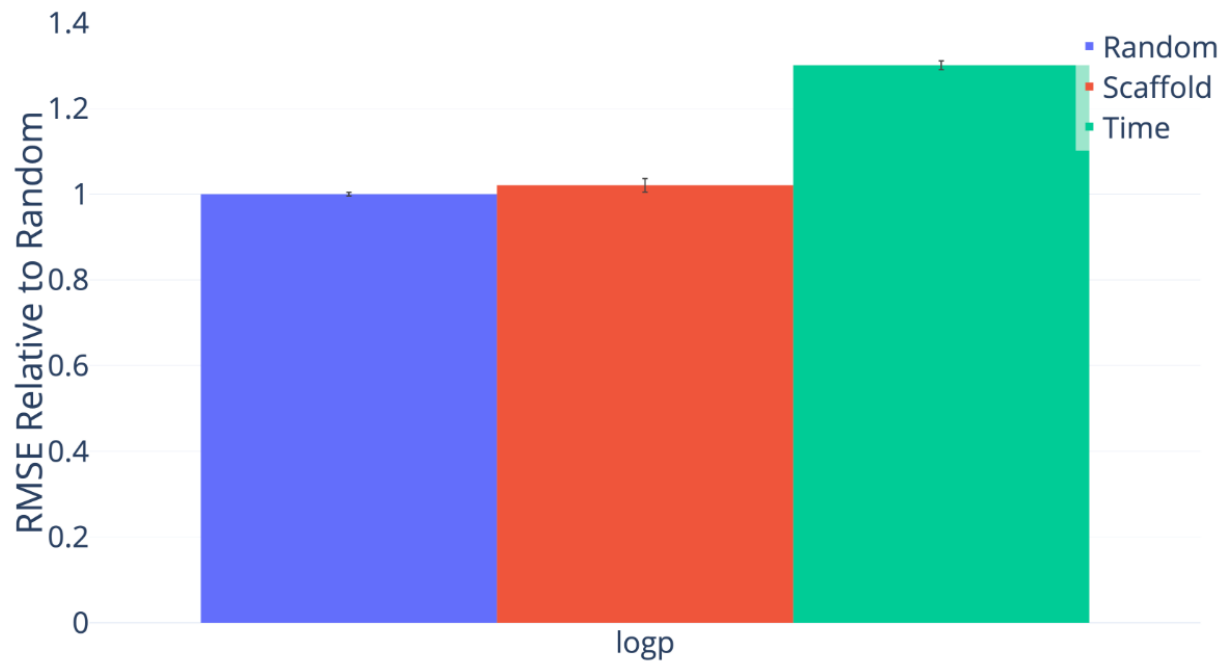


Figure S19: D-MPNN Performance by Split Type on Novartis datasets (lower = better).

Table S29: Performance of D-MPNN on different data splits on Novartis datasets. Note: All numbers are RMSE.

Dataset	Random	Scaffold	Time
LogP	0.532 ± 0.007	0.543 ± 0.027 (+2.07% p=0.00)	0.692 ± 0.017 (+2.07% p=0.00)

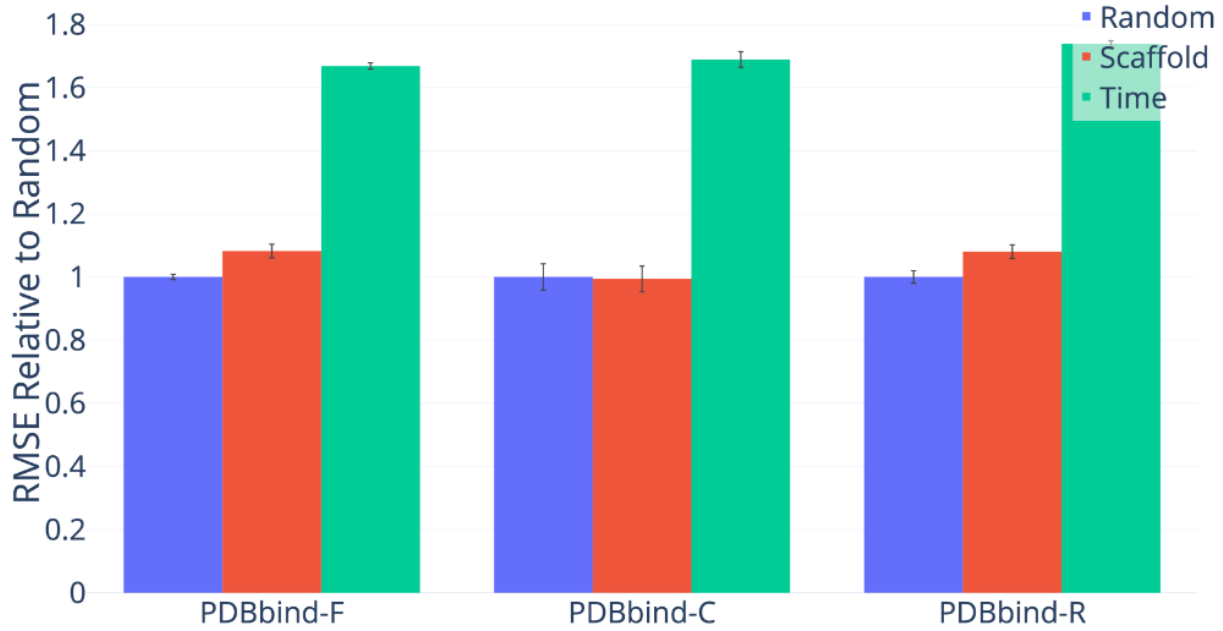


Figure S20: D-MPNN Performance by Split Type on PDBBind (lower = better).

Table S30: D-MPNN Performance by Split Type on PDBBind. Note: All numbers are RMSE.

Dataset	Random	Scaffold	Time
PDBbind-F	1.311 ± 0.034	$1.419 \pm 0.089 (+8.20\% \text{ p}=0.00)$	$2.187 \pm 0.041 (+8.20\% \text{ p}=0.00)$
PDBbind-C	2.151 ± 0.285	$2.138 \pm 0.278 (-0.64\% \text{ p}=0.74)$	$3.632 \pm 0.170 (-0.64\% \text{ p}=0.00)$
PDBbind-R	1.395 ± 0.087	$1.507 \pm 0.095 (+8.04\% \text{ p}=0.00)$	$2.424 \pm 0.046 (+8.04\% \text{ p}=0.00)$

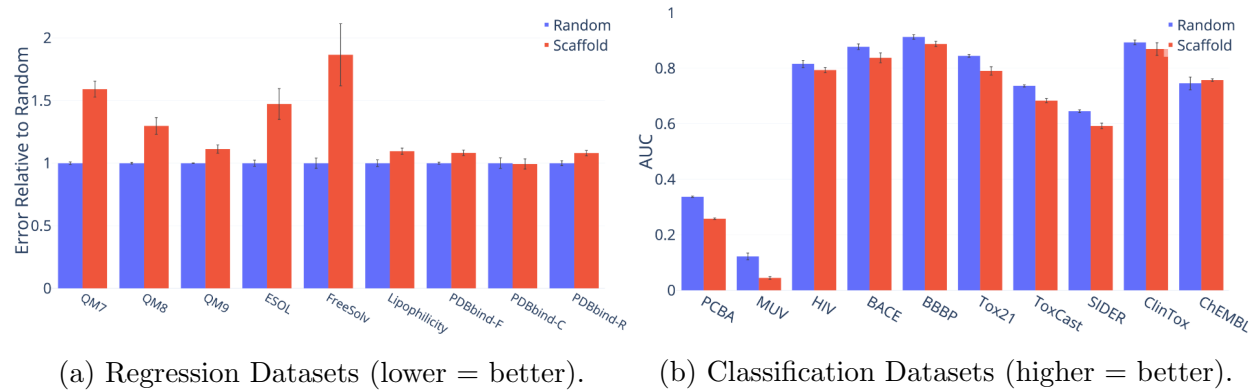


Figure S21: D-MPNN Performance by Split Type on Public Datasets.

Table S31: D-MPNN Performance by Split Type on Public Datasets.

Dataset	Metric	Random	Scaffold
QM7	MAE	66.475 ± 2.088	$105.775 \pm 13.202 (+59.12\% \text{ p}=0.00)$
QM8	MAE	0.011 ± 0.000	$0.014 \pm 0.002 (+29.75\% \text{ p}=0.00)$
QM9	MAE	3.101 ± 0.010	$3.451 \pm 0.174 (+11.28\% \text{ p}=0.03)$
ESOL	RMSE	0.665 ± 0.052	$0.980 \pm 0.258 (+47.31\% \text{ p}=0.00)$
FreeSolv	RMSE	1.167 ± 0.150	$2.177 \pm 0.914 (+86.56\% \text{ p}=0.00)$
Lipophilicity	RMSE	0.596 ± 0.050	$0.653 \pm 0.046 (+9.54\% \text{ p}=0.00)$
PDBbind-F	RMSE	1.311 ± 0.034	$1.419 \pm 0.089 (+8.20\% \text{ p}=0.00)$
PDBbind-C	RMSE	2.151 ± 0.285	$2.138 \pm 0.278 (-0.64\% \text{ p}=0.74)$
PDBbind-R	RMSE	1.395 ± 0.087	$1.507 \pm 0.095 (+8.04\% \text{ p}=0.00)$
PCBA	PRC-AUC	0.337 ± 0.004	$0.258 \pm 0.005 (-23.43\% \text{ p}=0.00)$
MUV	PRC-AUC	0.122 ± 0.020	$0.045 \pm 0.007 (-63.44\% \text{ p}=0.01)$
HIV	ROC-AUC	0.816 ± 0.023	$0.794 \pm 0.016 (-2.73\% \text{ p}=0.14)$
BACE	ROC-AUC	0.878 ± 0.032	$0.838 \pm 0.056 (-4.55\% \text{ p}=0.00)$
BBBP	ROC-AUC	0.913 ± 0.026	$0.888 \pm 0.029 (-2.78\% \text{ p}=0.00)$
Tox21	ROC-AUC	0.845 ± 0.015	$0.791 \pm 0.047 (-6.42\% \text{ p}=0.00)$
ToxCast	ROC-AUC	0.737 ± 0.013	$0.684 \pm 0.023 (-7.16\% \text{ p}=0.00)$
SIDER	ROC-AUC	0.646 ± 0.016	$0.593 \pm 0.032 (-8.25\% \text{ p}=0.00)$
ClinTox	ROC-AUC	0.894 ± 0.027	$0.870 \pm 0.072 (-2.70\% \text{ p}=0.01)$
ChEMBL	ROC-AUC	0.746 ± 0.040	$0.758 \pm 0.008 (+1.60\% \text{ p}=0.47)$

Ablations

Message Type

Here we describe the implementation and performance of our atom-based and undirected bond-based messages. For the most direct comparison, we implemented these as options in our model; the changes are only a few lines of code in each case. Therefore, in each case, we simply detail the differences from our directed bond-based messages.

Atom Messages

We initialize messages based on atom features rather than bond features, according to $h_v^0 = \tau(W_i x_v)$ rather than $h_{vw}^0 = \tau(W_i \text{ cat}(x_v, e_{vw}))$, with matrix dimensions adjusted accordingly.

During message passing, each atom receives messages according to $m_v^{t+1} = \sum_{k \in \{N(v)\}} h_k^t$.

Finally, m_v is the sum of all of the atom hidden states at the end of message passing.

Undirected Bond Messages

The only difference between undirected bonds and our D-MPNN is that before each message passing step, for each pair of bonded atoms v and w , we set h_{vw}^t and h_{wv}^t to each be equal to their average. Consequently, the hidden state for each directed bond is always equal to the hidden state of its reverse bond, resulting in message passing on undirected bonds.

Comparison of Different Message Types

Comparison of performance using different message passing paradigms. Our D-MPNN uses directed messages.

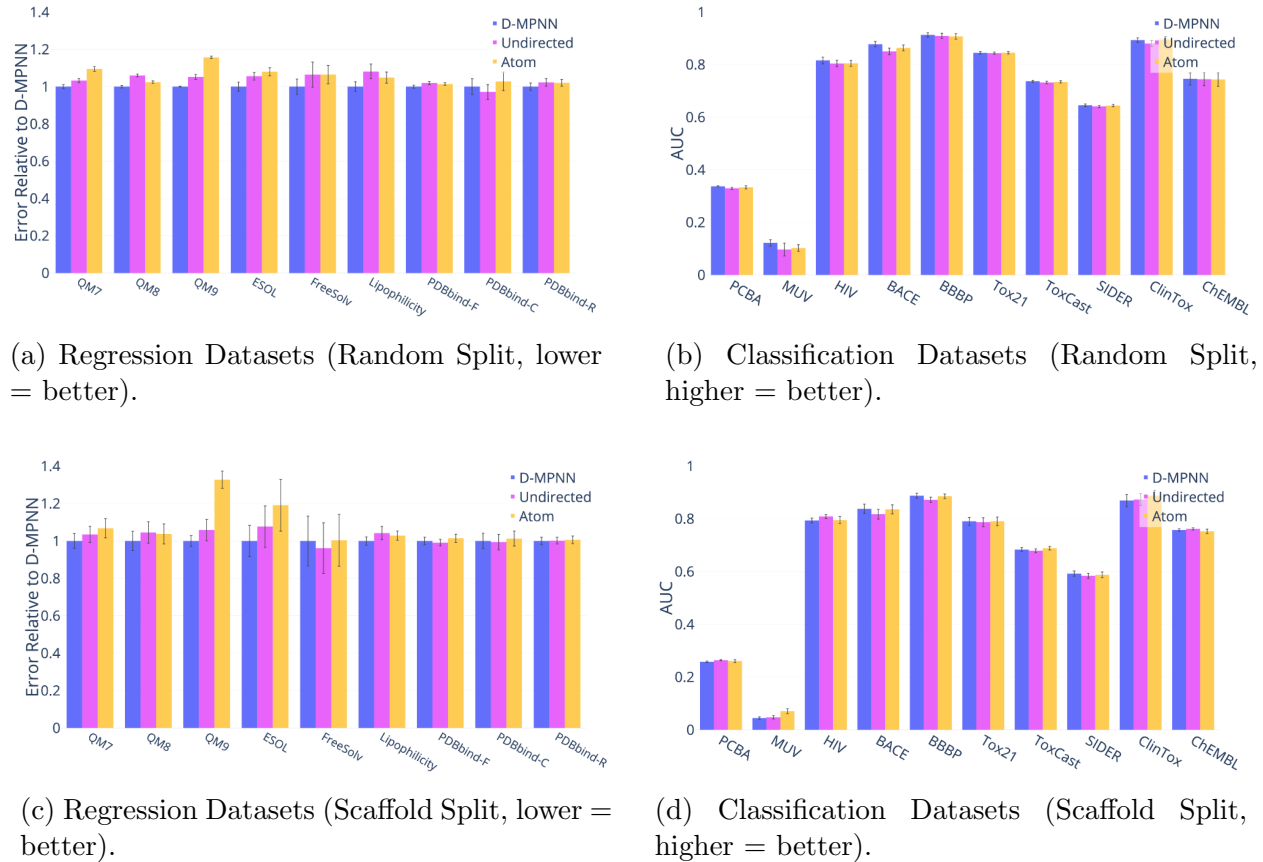


Figure S22: Message Type.

Table S32: Message Type (Random Split).

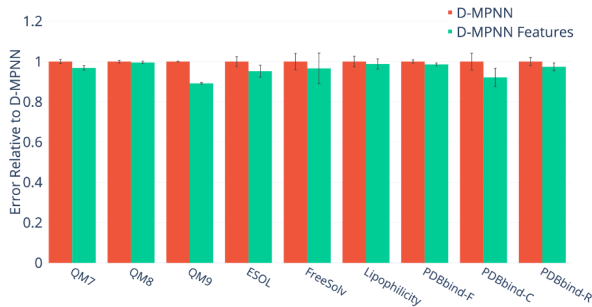
Dataset	Metric	D-MPNN	Undirected	Atom
QM7	MAE	66.475 \pm 2.088	68.628 \pm 2.177 (+3.24% p=0.05)	72.811 \pm 2.737 (+9.53% p=0.00)
QM8	MAE	0.0110 \pm 0.0002	0.012 \pm 0.000 (+5.99% p=0.00)	0.011 \pm 0.000 (+2.43% p=0.03)
QM9	MAE	3.101 \pm 0.010	3.263 \pm 0.069 (+5.23% p=0.06)	3.589 \pm 0.033 (+15.73% p=0.00)
ESOL	RMSE	0.665 \pm 0.052	0.702 \pm 0.042 (+5.62% p=0.11)	0.719 \pm 0.045 (+8.05% p=0.04)
FreeSolv	RMSE	1.167 \pm 0.150	1.242 \pm 0.249 (+6.44% p=0.43)	1.243 \pm 0.182 (+6.50% p=0.34)
Lipophilicity	RMSE	0.596 \pm 0.050	0.645 \pm 0.075 (+8.15% p=0.12)	0.625 \pm 0.056 (+4.87% p=0.25)
PDBbind-F	RMSE	1.311 \pm 0.034	1.337 \pm 0.036 (+1.98% p=0.13)	1.330 \pm 0.027 (+1.42% p=0.21)
PDBbind-C	RMSE	2.151 \pm 0.285	2.090 \pm 0.270 (-2.86% p=0.63)	2.211 \pm 0.339 (+2.79% p=0.68)
PDBbind-R	RMSE	1.395 \pm 0.087	1.427 \pm 0.090 (+2.30% p=0.44)	1.424 \pm 0.082 (+2.07% p=0.46)
PCBA	PRC-AUC	0.337 \pm 0.004	0.330 \pm 0.007 (-2.23% p=0.25)	0.333 \pm 0.010 (-1.15% p=0.61)
MUV	PRC-AUC	0.1222 \pm 0.0204	0.097 \pm 0.042 (-20.66% p=0.45)	0.103 \pm 0.022 (-16.05% p=0.38)
HIV	ROC-AUC	0.816 \pm 0.023	0.805 \pm 0.022 (-1.40% p=0.59)	0.805 \pm 0.019 (-1.33% p=0.60)
BACE	ROC-AUC	0.878 \pm 0.032	0.850 \pm 0.039 (-3.13% p=0.12)	0.864 \pm 0.035 (-1.63% p=0.37)
BBBP	ROC-AUC	0.913 \pm 0.026	0.910 \pm 0.032 (-0.40% p=0.79)	0.908 \pm 0.033 (-0.63% p=0.68)
Tox21	ROC-AUC	0.845 \pm 0.015	0.844 \pm 0.014 (-0.14% p=0.86)	0.845 \pm 0.014 (+0.04% p=0.96)
ToxCast	ROC-AUC	0.737 \pm 0.013	0.732 \pm 0.015 (-0.61% p=0.49)	0.735 \pm 0.014 (-0.27% p=0.75)
SIDER	ROC-AUC	0.646 \pm 0.016	0.641 \pm 0.014 (-0.73% p=0.50)	0.644 \pm 0.014 (-0.23% p=0.83)
ClinTox	ROC-AUC	0.894 \pm 0.027	0.881 \pm 0.037 (-1.49% p=0.38)	0.896 \pm 0.037 (+0.22% p=0.89)
ChEMBL	ROC-AUC	0.746 \pm 0.040	0.745 \pm 0.043 (-0.14% p=0.98)	0.744 \pm 0.045 (-0.31% p=0.95)

Table S33: Message Type (Scaffold Split).

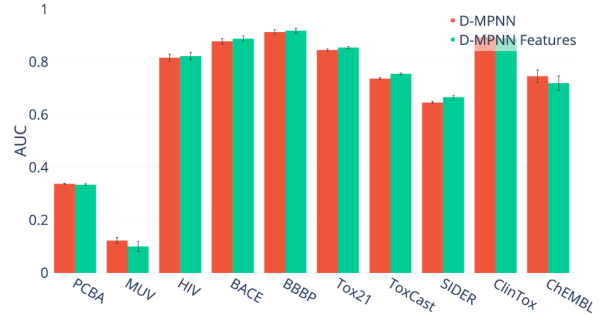
Dataset	Metric	D-MPNN	Undirected	Atom
QM7	MAE	105.775 \pm 13.202	109.494 \pm 14.420 (+3.52% p=0.56)	112.960 \pm 17.211 (+6.79% p=0.32)
QM8	MAE	0.0143 \pm 0.0023	0.015 \pm 0.003 (+4.54% p=0.57)	0.015 \pm 0.002 (+3.76% p=0.63)
QM9	MAE	3.451 \pm 0.174	3.654 \pm 0.343 (+5.89% p=0.46)	4.583 \pm 0.274 (+32.82% p=0.03)
ESOL	RMSE	0.980 \pm 0.258	1.055 \pm 0.343 (+7.68% p=0.59)	1.167 \pm 0.430 (+19.13% p=0.27)
FreeSolv	RMSE	2.177 \pm 0.914	2.093 \pm 0.936 (-3.86% p=0.84)	2.185 \pm 0.952 (+0.37% p=0.99)
Lipophilicity	RMSE	0.653 \pm 0.046	0.681 \pm 0.074 (+4.22% p=0.34)	0.672 \pm 0.051 (+2.86% p=0.41)
PDBbind-F	RMSE	1.419 \pm 0.089	1.407 \pm 0.078 (-0.85% p=0.75)	1.439 \pm 0.100 (+1.43% p=0.64)
PDBbind-C	RMSE	2.138 \pm 0.278	2.125 \pm 0.280 (-0.59% p=0.92)	2.165 \pm 0.272 (+1.26% p=0.83)
PDBbind-R	RMSE	1.507 \pm 0.095	1.510 \pm 0.086 (+0.15% p=0.96)	1.517 \pm 0.097 (+0.62% p=0.83)
PCBA	PRC-AUC	0.258 \pm 0.005	0.264 \pm 0.004 (+2.36% p=0.21)	0.261 \pm 0.010 (+1.12% p=0.69)
MUV	PRC-AUC	0.0447 \pm 0.0074	0.047 \pm 0.011 (+6.26% p=0.75)	0.071 \pm 0.016 (+58.69% p=0.13)
HIV	ROC-AUC	0.794 \pm 0.016	0.809 \pm 0.014 (+1.94% p=0.34)	0.795 \pm 0.023 (+0.20% p=0.93)
BACE	ROC-AUC	0.838 \pm 0.056	0.818 \pm 0.059 (-2.39% p=0.46)	0.836 \pm 0.055 (-0.21% p=0.94)
BBBP	ROC-AUC	0.888 \pm 0.029	0.872 \pm 0.032 (-1.75% p=0.29)	0.886 \pm 0.028 (-0.25% p=0.87)
Tox21	ROC-AUC	0.791 \pm 0.047	0.787 \pm 0.054 (-0.43% p=0.88)	0.791 \pm 0.051 (+0.02% p=1.00)
ToxCast	ROC-AUC	0.684 \pm 0.023	0.679 \pm 0.022 (-0.69% p=0.65)	0.689 \pm 0.021 (+0.68% p=0.65)
SIDER	ROC-AUC	0.593 \pm 0.032	0.584 \pm 0.031 (-1.40% p=0.57)	0.588 \pm 0.034 (-0.76% p=0.76)
ClinTox	ROC-AUC	0.870 \pm 0.072	0.873 \pm 0.073 (+0.41% p=0.91)	0.888 \pm 0.064 (+2.14% p=0.56)
ChEMBL	ROC-AUC	0.758 \pm 0.008	0.762 \pm 0.007 (+0.57% p=0.57)	0.753 \pm 0.014 (-0.67% p=0.65)

RDKit Features

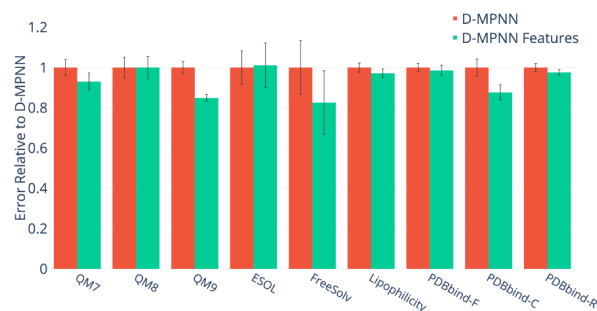
Effect of adding RDKit features to our optimized D-MPNN.



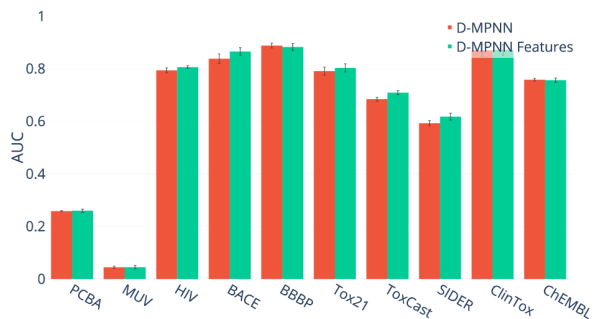
(a) Regression Datasets (Random Split, lower = better).



(b) Classification Datasets (Random Split, lower = better).



(c) Regression Datasets (Scaffold Split, lower = better).



(d) Classification Datasets (Scaffold Split, higher = better).

Figure S23: RDKit Features.

Table S34: RDKit Features (Random Split).

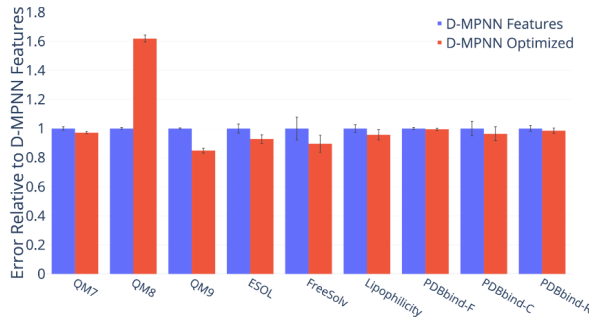
Dataset	Metric	D-MPNN	D-MPNN Features
QM7	MAE	66.475 \pm 2.088	64.390 \pm 2.361 (-3.14% p=0.07)
QM8	MAE	0.0110 \pm 0.0002	0.011 \pm 0.000 (-0.42% p=0.64)
QM9	MAE	3.101 \pm 0.010	2.766 \pm 0.022 (-10.79% p=0.00)
ESOL	RMSE	0.665 \pm 0.052	0.633 \pm 0.062 (-4.77% p=0.25)
FreeSolv	RMSE	1.167 \pm 0.150	1.127 \pm 0.282 (-3.39% p=0.70)
Lipophilicity	RMSE	0.596 \pm 0.050	0.589 \pm 0.048 (-1.18% p=0.76)
PDBbind-F	RMSE	1.311 \pm 0.034	1.293 \pm 0.028 (-1.41% p=0.22)
PDBbind-C	RMSE	2.151 \pm 0.285	1.983 \pm 0.309 (-7.84% p=0.24)
PDBbind-R	RMSE	1.395 \pm 0.087	1.359 \pm 0.086 (-2.61% p=0.37)
PCBA	PRC-AUC	0.337 \pm 0.004	0.334 \pm 0.006 (-0.86% p=0.57)
MUV	PRC-AUC	0.1222 \pm 0.0204	0.100 \pm 0.034 (-18.34% p=0.43)
HIV	ROC-AUC	0.816 \pm 0.023	0.822 \pm 0.024 (+0.72% p=0.79)
BACE	ROC-AUC	0.878 \pm 0.032	0.888 \pm 0.031 (+1.20% p=0.48)
BBBP	ROC-AUC	0.913 \pm 0.026	0.918 \pm 0.028 (+0.54% p=0.70)
Tox21	ROC-AUC	0.845 \pm 0.015	0.854 \pm 0.013 (+1.12% p=0.17)
ToxCast	ROC-AUC	0.737 \pm 0.013	0.755 \pm 0.010 (+2.46% p=0.01)
SIDER	ROC-AUC	0.646 \pm 0.016	0.667 \pm 0.019 (+3.25% p=0.03)
ClinTox	ROC-AUC	0.894 \pm 0.027	0.889 \pm 0.036 (-0.51% p=0.75)
ChEMBL	ROC-AUC	0.746 \pm 0.040	0.719 \pm 0.047 (-3.61% p=0.53)

Table S35: RDKit Features (Scaffold Split).

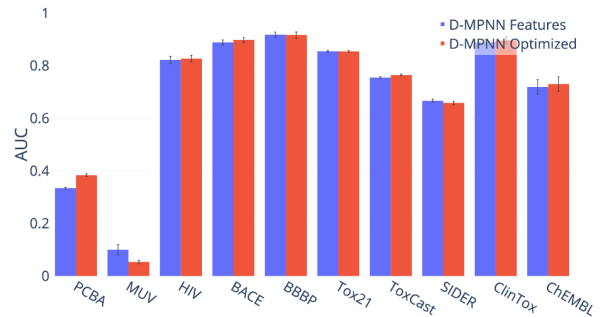
Dataset	Metric	D-MPNN	D-MPNN Features
QM7	MAE	105.775 ± 13.202	98.442 ± 13.936 (-6.93% p=0.26)
QM8	MAE	0.014 ± 0.002	0.014 ± 0.003 (+0.02% p=1.00)
QM9	MAE	3.451 ± 0.174	2.929 ± 0.106 (-15.12% p=0.05)
ESOL	RMSE	0.980 ± 0.258	0.991 ± 0.343 (+1.14% p=0.94)
FreeSolv	RMSE	2.177 ± 0.914	1.799 ± 1.088 (-17.37% p=0.42)
Lipophilicity	RMSE	0.653 ± 0.046	0.634 ± 0.045 (-2.85% p=0.38)
PDBbind-F	RMSE	1.419 ± 0.089	1.398 ± 0.115 (-1.45% p=0.66)
PDBbind-C	RMSE	2.138 ± 0.278	1.874 ± 0.253 (-12.35% p=0.05)
PDBbind-R	RMSE	1.507 ± 0.095	1.472 ± 0.066 (-2.35% p=0.36)
PCBA	PRC-AUC	0.258 ± 0.005	0.260 ± 0.010 (+0.62% p=0.83)
MUV	PRC-AUC	0.045 ± 0.007	0.045 ± 0.011 (+0.73% p=0.97)
HIV	ROC-AUC	0.794 ± 0.016	0.806 ± 0.009 (+1.49% p=0.38)
BACE	ROC-AUC	0.838 ± 0.056	0.865 ± 0.045 (+3.26% p=0.26)
BBBP	ROC-AUC	0.888 ± 0.029	0.882 ± 0.043 (-0.62% p=0.74)
Tox21	ROC-AUC	0.791 ± 0.047	0.803 ± 0.049 (+1.52% p=0.59)
ToxCast	ROC-AUC	0.684 ± 0.023	0.709 ± 0.024 (+3.61% p=0.04)
SIDER	ROC-AUC	0.593 ± 0.032	0.618 ± 0.041 (+4.24% p=0.16)
ClinTox	ROC-AUC	0.870 ± 0.072	0.872 ± 0.063 (+0.21% p=0.95)
ChEMBL	ROC-AUC	0.758 ± 0.008	0.757 ± 0.014 (-0.17% p=0.90)

Hyperparameter Optimization

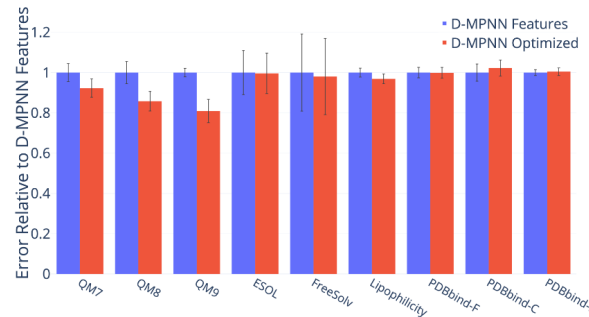
Effect of performing Bayesian hyperparameter optimization on the depth, hidden size, number of fully connected layers, and dropout of our model. Optimization was done on random splits and then the optimized model was applied to both random and scaffold splits.



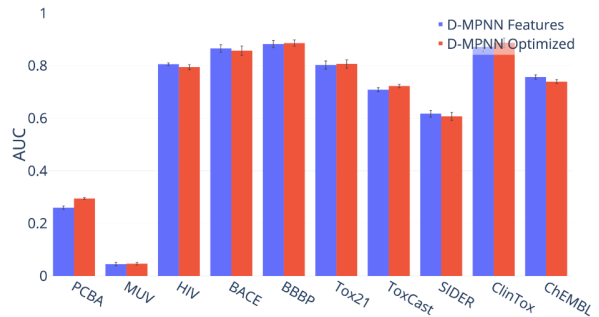
(a) Regression Datasets (Random Split, lower = better).



(b) Classification Datasets (Random Split, higher = better).



(c) Regression Datasets (Scaffold Split, lower = better).



(d) Classification Datasets (Scaffold Split, higher = better).

Figure S24: Hyperparameter Optimization.

Table S36: Hyperparameter Optimization (Random Split).

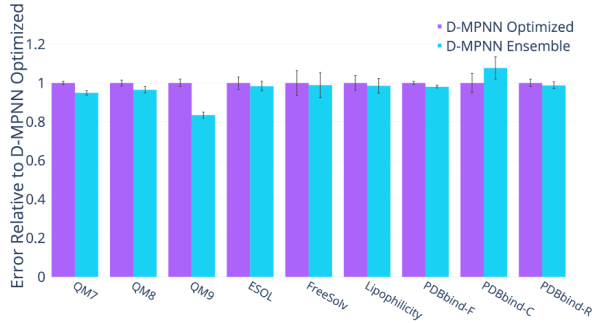
Dataset	Metric	D-MPNN Features	D-MPNN Optimized
QM7	MAE	64.390 \pm 2.361 (-3.14%)	62.542 \pm 1.649 (-5.92% p=0.07)
QM8	MAE	0.011 \pm 0.000 (-0.42%)	0.018 \pm 0.001 (+61.13% p=0.00)
QM9	MAE	2.766 \pm 0.022 (-10.79%)	2.346 \pm 0.080 (-24.34% p=0.01)
ESOL	RMSE	0.633 \pm 0.062 (-4.77%)	0.587 \pm 0.060 (-11.70% p=0.12)
FreeSolv	RMSE	1.127 \pm 0.282 (-3.39%)	1.009 \pm 0.207 (-13.49% p=0.31)
Lipophilicity	RMSE	0.589 \pm 0.048 (-1.18%)	0.563 \pm 0.067 (-5.48% p=0.35)
PDBbind-F	RMSE	1.293 \pm 0.028 (-1.41%)	1.286 \pm 0.033 (-1.88% p=0.67)
PDBbind-C	RMSE	1.983 \pm 0.309 (-7.84%)	1.910 \pm 0.299 (-11.24% p=0.60)
PDBbind-R	RMSE	1.359 \pm 0.086 (-2.61%)	1.338 \pm 0.082 (-4.08% p=0.60)
PCBA	PRC-AUC	0.334 \pm 0.006 (-0.86%)	0.383 \pm 0.009 (+13.63% p=0.02)
MUV	PRC-AUC	0.100 \pm 0.034 (-18.34%)	0.053 \pm 0.012 (-56.31% p=0.15)
HIV	ROC-AUC	0.822 \pm 0.024 (+0.72%)	0.827 \pm 0.023 (+1.31% p=0.82)
BACE	ROC-AUC	0.888 \pm 0.031 (+1.20%)	0.898 \pm 0.031 (+2.26% p=0.52)
BBBP	ROC-AUC	0.918 \pm 0.028 (+0.54%)	0.917 \pm 0.037 (+0.37% p=0.92)
Tox21	ROC-AUC	0.854 \pm 0.013 (+1.12%)	0.854 \pm 0.012 (+1.09% p=0.97)
ToxCast	ROC-AUC	0.755 \pm 0.010 (+2.46%)	0.764 \pm 0.011 (+3.77% p=0.08)
SIDER	ROC-AUC	0.667 \pm 0.019 (+3.25%)	0.658 \pm 0.020 (+1.93% p=0.35)
ClinTox	ROC-AUC	0.889 \pm 0.036 (-0.51%)	0.897 \pm 0.042 (+0.30% p=0.69)
ChEMBL	ROC-AUC	0.719 \pm 0.047 (-3.61%)	0.730 \pm 0.048 (-2.15% p=0.81)

Table S37: Hyperparameter Optimization (Scaffold Split).

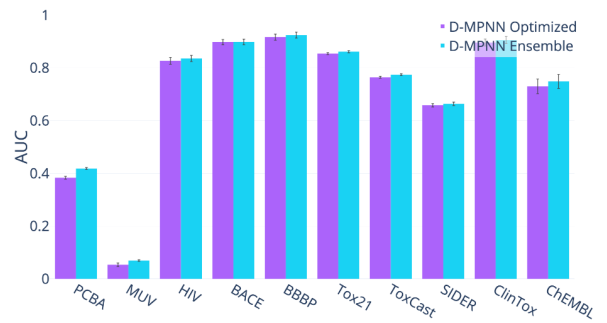
Dataset	Metric	D-MPNN Features	D-MPNN Optimized
QM7	MAE	98.442 \pm 13.936 (-6.93%)	90.869 \pm 14.199 (-14.09% p=0.26)
QM8	MAE	0.014 \pm 0.003 (+0.02%)	0.012 \pm 0.002 (-14.20% p=0.09)
QM9	MAE	2.929 \pm 0.106 (-15.12%)	2.370 \pm 0.294 (-31.32% p=0.09)
ESOL	RMSE	0.991 \pm 0.343 (+1.14%)	0.987 \pm 0.314 (+0.75% p=0.98)
FreeSolv	RMSE	1.799 \pm 1.088 (-17.37%)	1.763 \pm 1.075 (-18.99% p=0.94)
Lipophilicity	RMSE	0.634 \pm 0.045 (-2.85%)	0.615 \pm 0.048 (-5.88% p=0.37)
PDBbind-F	RMSE	1.398 \pm 0.115 (-1.45%)	1.397 \pm 0.117 (-1.53% p=0.98)
PDBbind-C	RMSE	1.874 \pm 0.253 (-12.35%)	1.916 \pm 0.236 (-10.38% p=0.71)
PDBbind-R	RMSE	1.472 \pm 0.066 (-2.35%)	1.479 \pm 0.087 (-1.91% p=0.85)
PCBA	PRC-AUC	0.260 \pm 0.010 (+0.62%)	0.295 \pm 0.006 (+14.10% p=0.04)
MUV	PRC-AUC	0.045 \pm 0.011 (+0.73%)	0.047 \pm 0.009 (+4.37% p=0.86)
HIV	ROC-AUC	0.806 \pm 0.009 (+1.49%)	0.794 \pm 0.017 (+0.07% p=0.41)
BACE	ROC-AUC	0.865 \pm 0.045 (+3.26%)	0.857 \pm 0.057 (+2.30% p=0.73)
BBBP	ROC-AUC	0.882 \pm 0.043 (-0.62%)	0.886 \pm 0.036 (-0.21% p=0.84)
Tox21	ROC-AUC	0.803 \pm 0.049 (+1.52%)	0.806 \pm 0.050 (+1.98% p=0.87)
ToxCast	ROC-AUC	0.709 \pm 0.024 (+3.61%)	0.723 \pm 0.020 (+5.65% p=0.19)
SIDER	ROC-AUC	0.618 \pm 0.041 (+4.24%)	0.607 \pm 0.047 (+2.49% p=0.61)
ClinTox	ROC-AUC	0.872 \pm 0.063 (+0.21%)	0.887 \pm 0.058 (+1.99% p=0.58)
ChEMBL	ROC-AUC	0.757 \pm 0.014 (-0.17%)	0.739 \pm 0.012 (-2.47% p=0.25)

Ensembling

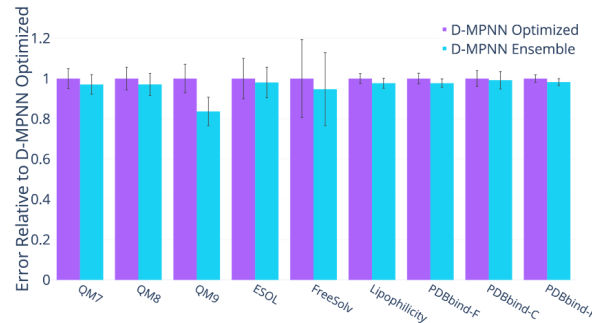
Benefit of ensembling five models instead of a single model. All results are using our best model settings (i.e. optimized hyperparameters and RDKit features, if they improved performance in the single model setting).



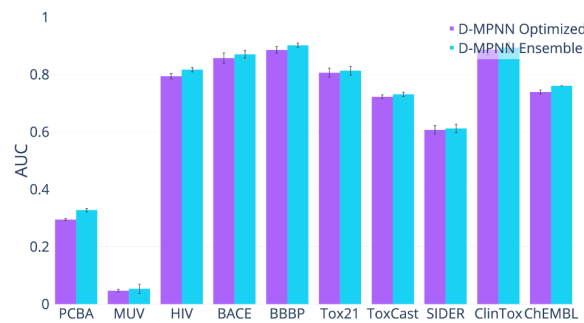
(a) Regression Datasets (Random Split, lower = better).



(b) Classification Datasets (Random Split, higher = better).



(c) Regression Datasets (Scaffold Split, lower = better).



(d) Classification Datasets (Scaffold Split, higher = better).

Figure S25: Ensembling.

Table S38: Ensembling (Random Split).

Dataset	Metric	D-MPNN Optimized	D-MPNN Ensemble
QM7	MAE	62.542 \pm 1.649 (-5.92%)	59.379 \pm 2.315 (-10.67% p=0.01)
QM8	MAE	0.018 \pm 0.001 (+61.13%)	0.017 \pm 0.001 (+55.42% p=0.14)
QM9	MAE	2.346 \pm 0.080 (-24.34%)	1.959 \pm 0.066 (-36.82% p=0.02)
ESOL	RMSE	0.587 \pm 0.060 (-11.70%)	0.578 \pm 0.046 (-13.08% p=0.71)
FreeSolv	RMSE	1.009 \pm 0.207 (-13.49%)	0.998 \pm 0.207 (-14.43% p=0.91)
Lipophilicity	RMSE	0.563 \pm 0.067 (-5.48%)	0.555 \pm 0.067 (-6.83% p=0.79)
PDBbind-F	RMSE	1.286 \pm 0.033 (-1.88%)	1.262 \pm 0.031 (-3.75% p=0.12)
PDBbind-C	RMSE	1.910 \pm 0.299 (-11.24%)	2.057 \pm 0.353 (-4.39% p=0.34)
PDBbind-R	RMSE	1.338 \pm 0.082 (-4.08%)	1.322 \pm 0.077 (-5.22% p=0.66)
PCBA	PRC-AUC	0.383 \pm 0.009 (+13.63%)	0.418 \pm 0.006 (+24.03% p=0.03)
MUV	PRC-AUC	0.053 \pm 0.012 (-56.31%)	0.069 \pm 0.005 (-43.38% p=0.16)
HIV	ROC-AUC	0.827 \pm 0.023 (+1.31%)	0.836 \pm 0.020 (+2.40% p=0.66)
BACE	ROC-AUC	0.898 \pm 0.031 (+2.26%)	0.898 \pm 0.034 (+2.31% p=0.98)
BBBP	ROC-AUC	0.917 \pm 0.037 (+0.37%)	0.925 \pm 0.036 (+1.23% p=0.65)
Tox21	ROC-AUC	0.854 \pm 0.012 (+1.09%)	0.861 \pm 0.012 (+1.95% p=0.22)
ToxCast	ROC-AUC	0.764 \pm 0.011 (+3.77%)	0.774 \pm 0.011 (+5.09% p=0.08)
SIDER	ROC-AUC	0.658 \pm 0.020 (+1.93%)	0.664 \pm 0.021 (+2.79% p=0.56)
ClinTox	ROC-AUC	0.897 \pm 0.042 (+0.30%)	0.906 \pm 0.043 (+1.33% p=0.64)
ChEMBL	ROC-AUC	0.730 \pm 0.048 (-2.15%)	0.749 \pm 0.046 (+0.41% p=0.67)

Table S39: Ensembling (Scaffold Split).

Dataset	Metric	D-MPNN Optimized	D-MPNN Ensemble
QM7	MAE	90.869 \pm 14.199 (-14.09%)	88.201 \pm 13.899 (-16.61% p=0.68)
QM8	MAE	0.012 \pm 0.002 (-14.20%)	0.012 \pm 0.002 (-16.69% p=0.72)
QM9	MAE	2.370 \pm 0.294 (-31.32%)	1.983 \pm 0.289 (-42.53% p=0.25)
ESOL	RMSE	0.987 \pm 0.314 (+0.75%)	0.968 \pm 0.237 (-1.21% p=0.88)
FreeSolv	RMSE	1.763 \pm 1.075 (-18.99%)	1.670 \pm 1.008 (-23.27% p=0.85)
Lipophilicity	RMSE	0.615 \pm 0.048 (-5.88%)	0.600 \pm 0.049 (-8.04% p=0.54)
PDBbind-F	RMSE	1.397 \pm 0.117 (-1.53%)	1.365 \pm 0.092 (-3.79% p=0.51)
PDBbind-C	RMSE	1.916 \pm 0.236 (-10.38%)	1.900 \pm 0.262 (-11.12% p=0.89)
PDBbind-R	RMSE	1.479 \pm 0.087 (-1.91%)	1.453 \pm 0.080 (-3.60% p=0.51)
PCBA	PRC-AUC	0.295 \pm 0.006 (+14.10%)	0.328 \pm 0.011 (+26.88% p=0.04)
MUV	PRC-AUC	0.047 \pm 0.009 (+4.37%)	0.053 \pm 0.027 (+19.59% p=0.72)
HIV	ROC-AUC	0.794 \pm 0.017 (+0.07%)	0.817 \pm 0.013 (+2.94% p=0.21)
BACE	ROC-AUC	0.857 \pm 0.057 (+2.30%)	0.871 \pm 0.041 (+3.89% p=0.56)
BBBP	ROC-AUC	0.886 \pm 0.036 (-0.21%)	0.902 \pm 0.024 (+1.56% p=0.28)
Tox21	ROC-AUC	0.806 \pm 0.050 (+1.98%)	0.814 \pm 0.047 (+2.89% p=0.75)
ToxCast	ROC-AUC	0.723 \pm 0.020 (+5.65%)	0.731 \pm 0.023 (+6.89% p=0.40)
SIDER	ROC-AUC	0.607 \pm 0.047 (+2.49%)	0.612 \pm 0.047 (+3.31% p=0.82)
ClinTox	ROC-AUC	0.887 \pm 0.058 (+1.99%)	0.895 \pm 0.050 (+2.86% p=0.76)
ChEMBL	ROC-AUC	0.739 \pm 0.012 (-2.47%)	0.761 \pm 0.000 (+0.39% p=0.09)

Effect of Data Size

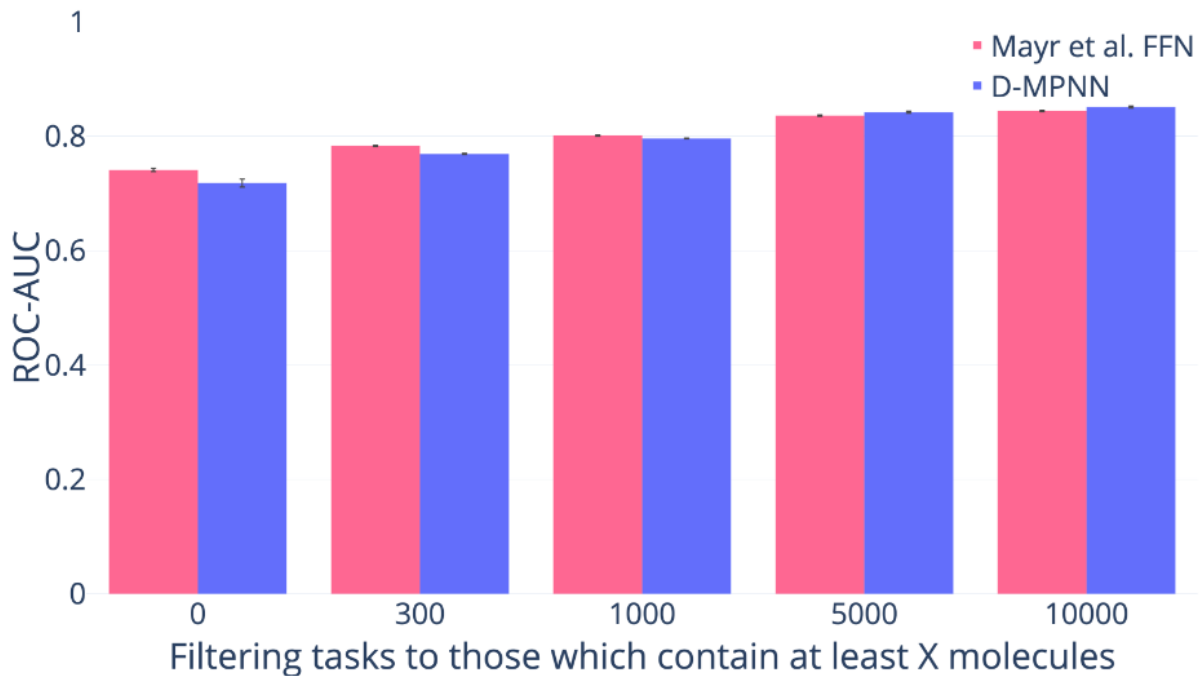


Figure S26: Effect of Data Size on ChEMBL (higher = better).

Table S40: Effect of Data Size on ChEMBL. All numbers are ROC-AUC.

Min # of Compounds	Mayr et al. ^{S1} FFN	D-MPNN
0	0.741 ± 0.005	0.718 ± 0.012 (-3.10% p=0.09)
300	0.783 ± 0.002	0.769 ± 0.002 (-1.79% p=0.01)
1,000	0.801 ± 0.002	0.796 ± 0.001 (-0.62% p=0.06)
5,000	0.836 ± 0.002	0.842 ± 0.003 (+0.72% p=0.10)
10,000	0.844 ± 0.002	0.851 ± 0.003 (+0.83% p=0.08)

RDKit-Calculated Features

We used the following list of 200 RDKit functions to calculate the RDKit features used by our model.

BalabanJ	BertzCT	Chi0
Chi0n	Chi0v	Chi1

Chi1n	Chi1v	Chi2n
Chi2v	Chi3n	Chi3v
Chi4n	Chi4v	EState_VSA1
EState_VSA10	EState_VSA11	EState_VSA2
EState_VSA3	EState_VSA4	EState_VSA5
EState_VSA6	EState_VSA7	EState_VSA8
EState_VSA9	ExactMolWt	FpDensityMorgan1
FpDensityMorgan2	FpDensityMorgan3	FractionCSP3
HallKierAlpha	HeavyAtomCount	HeavyAtomMolWt
Ipc	Kappa1	Kappa2
Kappa3	LabuteASA	MaxAbsEStateIndex
MaxAbsPartialCharge	MaxEStateIndex	MaxPartialCharge
MinAbsEStateIndex	MinAbsPartialCharge	MinEStateIndex
MinPartialCharge	MolLogP	MolMR
MolWt	NHOHCount	NOCount
NumAliphaticCarbocycles	NumAliphaticHeterocycles	NumAliphaticRings
NumAromaticCarbocycles	NumAromaticHeterocycles	NumAromaticRings
NumHAcceptors	NumHDonors	NumHeteroatoms
NumRadicalElectrons	NumRotatableBonds	NumSaturatedCarbocycles
NumSaturatedHeterocycles	NumSaturatedRings	NumValenceElectrons
PEOE_VSA1	PEOE_VSA10	PEOE_VSA11
PEOE_VSA12	PEOE_VSA13	PEOE_VSA14
PEOE_VSA2	PEOE_VSA3	PEOE_VSA4
PEOE_VSA5	PEOE_VSA6	PEOE_VSA7
PEOE_VSA8	PEOE_VSA9	RingCount
SMR_VSA1	SMR_VSA10	SMR_VSA2
SMR_VSA3	SMR_VSA4	SMR_VSA5

SMR_VSA6	SMR_VSA7	SMR_VSA8
SMR_VSA9	SlogP_VSA1	SlogP_VSA10
SlogP_VSA11	SlogP_VSA12	SlogP_VSA2
SlogP_VSA3	SlogP_VSA4	SlogP_VSA5
SlogP_VSA6	SlogP_VSA7	SlogP_VSA8
SlogP_VSA9	TPSA	VSA_EState1
VSA_EState10	VSA_EState2	VSA_EState3
VSA_EState4	VSA_EState5	VSA_EState6
VSA_EState7	VSA_EState8	VSA_EState9
fr_Al_COO	fr_Al_OH	fr_Al_OH_noTert
fr_ArN	fr_Ar_COO	fr_Ar_N
fr_Ar_NH	fr_Ar_OH	fr_COO
fr_COO2	fr_C_O	fr_C_O_noCOO
fr_C_S	fr_HOCCN	fr_Imine
fr_NH0	fr_NH1	fr_NH2
fr_N_O	fr_Ndealkylation1	fr_Ndealkylation2
fr_Nhpyrrole	fr_SH	fr_aldehyde
fr_alkyl_carbamate	fr_alkyl_halide	fr_allylic_oxid
fr_amide	fr_amidine	fr_aniline
fr_aryl_methyl	fr_azide	fr_azo
fr_barbitur	fr_benzene	fr_benzodiazepine
fr_bicyclic	fr_diazo	fr_dihydropyridine
fr_epoxide	fr_ester	fr_ether
fr_furan	fr_guanido	fr_halogen
fr_hdrzine	fr_hdrzone	fr_imidazole
fr_imide	fr_isocyan	fr_isothiocyan
fr_ketone	fr_ketone_Topliss	fr_lactam

fr_lactone	fr_methoxy	fr_morpholine
fr_nitrile	fr_nitro	fr_nitro_arom
fr_nitro_arom_nonortho	fr_nitroso	fr_oxazole
fr_oxime	fr_para_hydroxylation	fr_phenol
fr_phenol_noOrthoHbond	fr_phos_acid	fr_phos_ester
fr_piperidine	fr_piperazine	fr_priamide
fr_prisulfonamid	fr_pyridine	fr_quatN
fr_sulfide	fr_sulfonamid	fr_sulfone
fr_term_acetylene	fr_tetrazole	fr_thiazole
fr_thiocyan	fr_thiophene	fr_unbrch_alkane
fr_urea	qed	

References

(S1) Mayr, A.; Klambauer, G.; Unterthiner, T.; Steijaert, M.; Wegner, J. K.; Ceulemans, H.; Clevert, D.-A.; Hochreiter, S. Large-Scale Comparison of Machine Learning Methods for Drug Target Prediction on ChEMBL. *Chemical Science* **2018**, *9*, 5441–5451.

(S2) Wu, Z.; Ramsundar, B.; Feinberg, E.; Gomes, J.; Geniesse, C.; Pappu, A. S.; Leswing, K.; Pande, V. MoleculeNet: A Benchmark for Molecular Machine Learning. *Chemical Science* **2018**, *9*, 513530.

(S3) Hans, C. Bayesian lasso regression. *Biometrika* **2009**, *96*, 835–845.